Research on NiW coatings as a promising replacement for Cr-VI : indentation and X-ray diffraction investigations

Siyang Lu

THÈSE POUR L'OBTENTION DU TITRE DE

DOCTORAT DE L'UNIVERSITE DE LILLE

En

Mécanique, génie mécanique, génie civil

Présentée par

Siyang LU

Research on NiW coatings as a promising replacement for Cr-VI: indentation and X-ray diffraction investigations

Revêtements NiW comme alternative au chromage dur : caractérisation par indentation et diffraction de rayons X

Soutenue le 5 Décembre 2022 devant le jury composé de :

Rapporteur（Président) :	Pr. Caroline RICHARD, Université de Tours
Rapporteur :	Pr. Eric LE BOURHIS, Université de Poitiers
Examinateur :	Dr. Anne MOUFTIEZ, Icam Lille
Examinateur :	MCF. Amélie FILLON, Université de Rennes 1
Invité :	Pr. Didier CHICOT, Université de Lille
Invité :	Dr. Alberto MEJIAS, JUNIA
Directeur de thèse :	Pr. Francine ROUDET, Université de Lille
Co-directeur de thèse :	MCF HDR Alex MONTAGNE, ENSAM de Lille

Ecole doctorale: Sciences de l'ingenierie et des systemes – EDENGSYS 632
Laboratoire: Laboratoire de Génie Civil et géo-Environnement – LGCgE ULR4515

Acknowledgement

I would like to express my sincerest gratitude to my thesis supervisors, Francine ROUDET and Alex MONTAGNE, for their invaluable guidance and support throughout this entire process. Besides, I would like to acknowledge professor Didier CHICOT who also gives me solid support and guidance. Their expertise and guidance have been instrumental in shaping the direction of my research and helping me to achieve my goals.

Sincerely thanks to Pr. Caroline RICHARD and Pr. Eric LE BOURHIS, whose suggestions and questions promote this work much better. And also, many thanks to Anne MOUFTIEZ, Amélie FILLON, and Alberto MEJIAS, especially their keen insight and encouragements for me.

I am grateful to my colleagues and friends who provided valuable support and encouragement during the writing process. Your words of encouragement and motivation kept me going even during the most difficult times. I also want to thank my family for their love and support throughout my studies. Their constant encouragement and understanding have allowed me to focus on my work and achieve this milestone.

I would like to acknowledge the support and resources provided by Interreg.

Lastly, I would like to extend my appreciation to the participants of my research, without whom this work would not have been possible. Their valuable insights and contributions have greatly enhanced my understanding of the topic.

Thank you all for your invaluable support and contribution to my thesis. I could not have done it without you.

Index

List of Figures

List of Tables

General Introduction

This work falls within the framework of the European Interreg project "Alt Ctrl Trans" (ALTernative au Chrome TRi et hexavaLent pour le secteur du TRANSport et de la TRANSformation), co-financed by the ERDF, initiated in January 2019 (http://www.altctrltrans.eu/fr/accueil/#project). Interreg France-Wallonie-Vlaanderen is one of Interreg programs that aims to promote new projects between France and Belgium. It aims to co-operate researchers and business people from Hauts-de-France and Grand Est in France, Wallonia, West, and East Flanders in Belgium. One hundred and seventy million euros are provided for the projects in different themes such as research and innovation, the competition of small and medium-sized companies, heritage, natural resources and risk management, and social cohesion, health, training, and employment. The Alt Ctrl Trans Interreg project lies in the research and innovation theme.

The objective is to develop and promote viable and effective alternatives to hard chromium coatings, also called hexavalent chromium (Cr-VI), for the transport and processing industries. Protection of tools and components (to be used in automobile and aerospace industry, for example) by coatings is used to enhance their performance and service life [1]. Coatings made from chromium VI are used because of their easy-to-depose process and their excellent mechanical properties, especially in tribology [2]. However, chromium VI is classified as CMR (Carcinogenic Mutagenic Reprotoxic) because of its very high toxicity during its manufacturing due to the use of Cr^{6+} solutions. It leads to liver damage, pulmonary congestion and causes skin irritation resulting in ulcer formation [3]. The newest research shows that Cr-VI is also neurotoxic [4].This is why, European directives imposed by REACH (Registration, Evaluation, Authorisation and Restriction of Chemicals) drastically reduced the use of hexavalent chromium and aim to totally eliminate its use by 2024.

To date, Cr-VI is sometimes replaced by chromium trioxide (Cr-III) because of Cr^{3+} ions are non-toxic under certain concentration. Some researches believed that Cr-III has similar or even better mechanical properties in some certain perspectives than Cr-VI, for example the anti-wear and corrosion performance [5][6]. Unfortunately, it is difficult to obtain a thick and uniform chromium

film from Cr-III plating bath. At the same time, this type of deposit has a "brittle" character with through cracks and the presence of carbon and oxygen atoms which make it more sensitive to corrosion than Cr-VI [7].Thus, this type of coating cannot be used in corrosive environments.

NiW may be a good replacement for Cr-VI, and that is why this work focuses on comparing the properties between these two materials. NiW electro-deposition can provide us materials with good corrosion and wear resistance, and it is environmental friendly as well [8][9]. Electro-deposition is an economic and simple way at the same time.

In order to compare the mechanical behavior of coatings, indentation tests have been performed. Indentation is a fast and reliable test. It allows a local solicitation, at small loads and forces, particularly well adapted for coated systems. When indenting a material, there will be a permanent shape change when a force is applied, and the hardness can be defined as the plastic resistance during this process. Since hardness is related to some other mechanical properties like strength, ductility and fatigue resistance, hardness measurement can be used in industry as a fast and relatively cheap material quality control method. Nowadays it is known that material hardness is a multifunctional physical property depending on a large number of internal and external factors.

X-ray diffraction test is a powerful technique which is non-destructive, and works most effectively with materials that are wholly, or partly, crystalline. This method bases on the Bragg's law to get the information of the materials' structures. By collecting the diffracted X-rays, sample's structure can be analyzed. It is convenient to determine the orientation of the crystals.

In chapter I, the main theories and method used in this work will be presented. The main idea is focused on the mechanical properties, for example hardness and elastic modulus, and explore the methods for structures and crack analysis. For the mechanical properties, the indentation test is displayed and the differences between macro, micro and nano indentation are discussed. Besides, different models are applied to take into account the indentation size effect, tip defect and substrate effect. While the samples' structures are mainly observed by the X-rays diffraction test. Many cracks are generated on the coatings surface by different experimental approaches: indentation, tensile test,

scratch test, and several analysis ways are presented as well.

In chapter II, the indentation tests which focus on the mechanical properties are discussed. The work aims to investigate electroplated NiW coatings obtained under different process conditions and compare to the Cr-VI as a reference. Regarding the roughness of the surface, we proposed to apply classical indentation test in micro scale to characterize the mechanical properties of the samples. Tests are applied on both top surfaces and cross-sections and results are discussed. In the analysis, both tip defect and indentation size effect are taken into account. Furthermore, the micro instrumented indentation tests are carried out for the comparison of hardness and the investigation of elastic modulus.

In chapter III, the main idea is to explore the information of the structures by the X-rays diffraction tests. Firstly, the comparison is made between our samples with the standard peaks of Cr-VI and NiW to know the preferred orientation. It is also interesting to know if the temperature has an influence on the preferred orientation and stress inside the coatings by both *ex-situ* and *in-situ* experiments. Additionally, the cracks on the surface generated by indentation, scratch and tensile tests are presented and discussed. This information can help to compare the toughness and adhesion of the coatings.

In chapter IV, it is a general conclusion and perspective for further work.

During the thesis, this work was presented every six months on the Comac of the Interreg.

Besides, we attended and made a presentation on the conference:

S.Lu et al., Characterization of the Ni-W coating as a replacement for chrome VI. In Lorient; 2021.

There is a publication as well:

S. Lu et al., “Vickers hardness of NiW coating as a potential replacement for Cr-VI: A methodology to consider size effect and tip defect in classical microindentation,” Surf. Coatings Technol., vol. 447, no. August, p. 128812, 2022, doi: 10.1016/j.surfcoat.2022.128812.

Chapter I. Background

This thesis will compare NiW and Cr-VI coatings in several different perspectives, mainly in mechanical properties. There are many kinds of ways to compare the mechanical properties among several materials, including indentation test, X-ray diffraction test, scratch test and tensile test etc. In this chapter, we will mainly discuss the theoretical background.

1.1 Indentation test

Indentation test could be simply described: a tip, or indenter, of known shape and mechanical properties is pressed against a material to be analyzed. This load, or force, is also known. When the load is applied by a dead weight, we talk about classical indentation or hardness test. After the removal of the load and the withdrawal of the tip, the residual imprint is measured and, according to different definitions, a hardness can be calculated. On the other hand, when the load is progressively applied and removed with an electro-mechanical system for example, force and penetration depth of the tip are continuously recorded, we talk about instrumented indentation (IIT). The collected data give the so-called load-displacement curve. This curve is then processed following models, and mechanical properties, such as hardness, **H**, and Young's modulus, **E**, could be extracted from the shape of the curve. As a general definition, hardness is calculated as the ratio of the applied load over the area of the imprint. The latter one has various definitions depending on the scale considered.

There are three scales classically defined in indentation: macro, micro and nano scales, coming from ISO 14577-1:2015 (Table I-1) [10]. The indenter could be with a shape of a ball, pyramid, or cone. Each shape of the indenter has its specifical name as respectively: Brinell or Meyer; Vickers, Knoop or Berkovich; and Rockwell. The hardness is correlated with the plastic deformation of the surface or the penetration depth of the indenter (h), under a given load (F), and within a specific period of time [11].

The hardness of a solid material can be defined as a measure of its resistance to a permanent shape change when a force is applied. Besides indentation test, the deformation can be produced by different

methods, like scratching, cutting, mechanical wear, or bending. In metals, ceramics, and most of polymers, the hardness is related to the plastic deformation of the surface.

Table I-1. *Scales of indentation (ISO 14577-1:2015).*

	Macro	**Micro**	**Nano**
F (load)	$2N \leq F \leq 30kN$	$F < 2N$	\
h (depth)	\	$h > 0.2\ \mu m$	$h \leq 0.2\ \mu m$

1.1.1 Macro- and micro-indentation test

There are many different kinds of indentation test such as Meyer test, Brinell test, Vickers test. Their differences mainly lie in the shape of the tip and the definition of the imprint area.

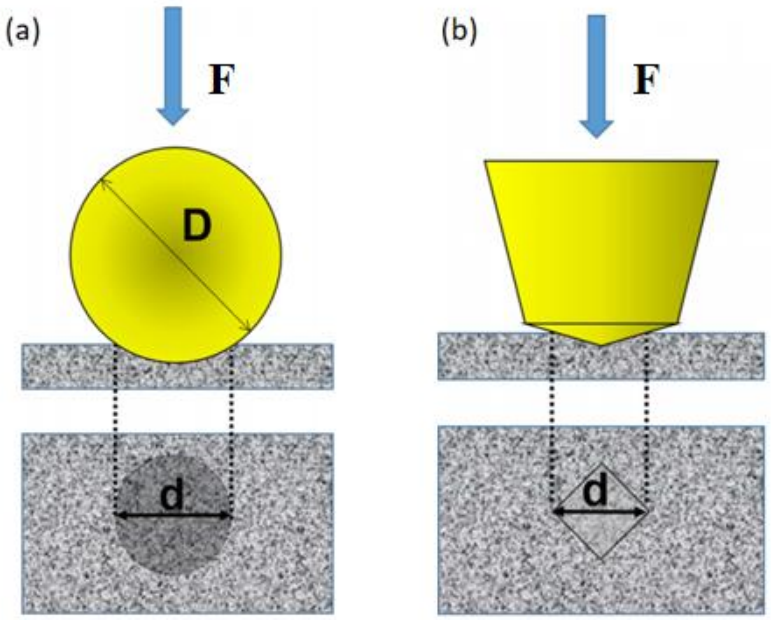

Figure I-1. *(a)Brinell macro-indentation test and (b) Vickers macro-indentation tes*t [11], *with their actual surface areas* A_c *respectively.*

Brinell test is commonly considered as the first modern indentation test: a sphere, of known diameter,

is pressed against the material to be tested and after the full withdrawal of the sphere, the diameter of the residual imprint is measured (Figure I-1(a)). Then, the hardness is defined as the ratio between the applied load and the real imprint area. Later, in 1908, Meyer test is proposed by Prof. Eugene Meyer in Germany. This test is experimentally the same as Brinell but the hardness is defined here as the ratio of the applied load over the projected area. Comparing to the Brinell test, Meyer test is less sensitive to the applied load. An empirical equation was also deduced between the Load ***F*** and the diameter of the imprint ***d***, which is known as Meyer's law:

$$F = kd^n \tag{I-1}$$

Where ***k*** is a constant of proportionality. The exponent ***n***, which is also named Meyer index, depends on the state of work hardening of the material, but it is independent with the diameter D of the ball indenter. The constant ***n*** commonly is 2 for fully strain hardened materials while it is 2.5 for fully annealed materials [12]. The Meyer hardness number (MHN) is expressed by the relationship between the indentation load ***F*** and the projected area A_p of the indentation:

$$MHN = \frac{F}{A_P} = \frac{4F}{\pi d^2} \tag{I-2}$$

The sensitivity to applied load of Brinell test leads to the development of Vickers indenter, which is a four-sided pyramid with an angle of 136° at its summit (Figure I-2). Thus, following the same experimental protocol as Brinell test and the same hardness definition, hardness is constant whatever the load applied. And both of them can be carried out in macro scale as well as micro scale.

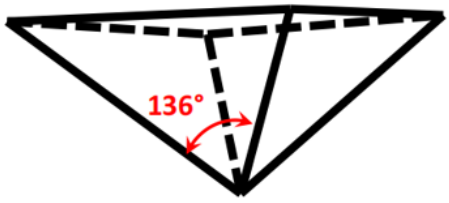

Figure I-2. *Schematic of Vickers indenter.*

In indentation test, the use of different area will give out different result of mechanical properties.

The most common known are actual area (*Ac*) and projected area (*Ap*). Projected area is the two dimensional area measurement of a three-dimensional object by projecting its shape on the surface of specimen plane. The difference between them are shown as Figure I-3 for a Brinell test.

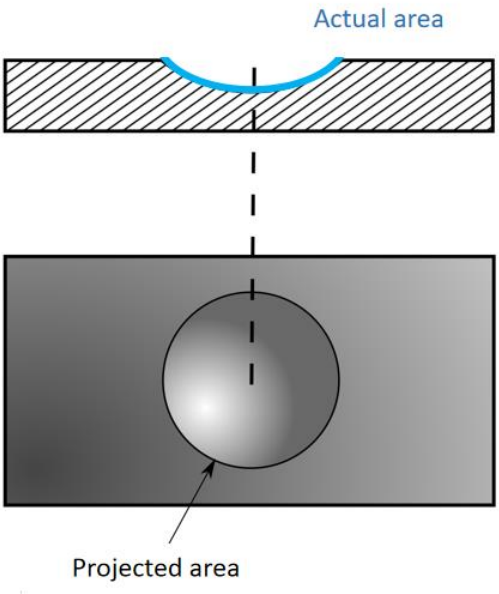

Figure I-3. *Schematic of actual area and projected area.*

Schematic and imprint of Brinell test is shown in Figure I-1(a) , where the actual area is represented after unloading. In this test, a ball of diameter *D (mm)* is used to indent the material through the application of a load *F (kN)*. The diameter *d (mm)* of the residual imprint on the surface is measured with an optical microscope, and the Brinell hardness number (BHN) is then calculated as the load divided by the actual area A_c of the curved surface of the impression:

$$BHN = \frac{F}{A_c} = \frac{2F}{\pi D(D-\sqrt{D^2-d^2})} \quad \text{(I-3)}$$

Schematic and resulting imprint of Vickers hardness test is shown in Figure I-1(b). The Vickers hardness value, *HV*, can be calculated using the load ***L*** and the actual surface area of the impression ***Ac*** [13]:

$$HV = \frac{F}{A_c} = \frac{2F}{d^2} sin\frac{136^\circ}{2} \quad \text{(I-4)}$$

where ***F*** is measured in *kgf* and ***d*** *(mm)* is equal to the average length of the diagonals measured from corner to opposite corner on the residual impression in the specimen surface.

The use of indentation forces below 1 kgf (~ 10 N) with the Vickers test was first evaluated in 1932 at the National Physical Laboratory in the UK [14]. Vickers tests are one of the most common indentation tests and they can be carried out at different scales of measurement [15]. In classical indentation test, the residual imprint is observed after the withdrawal of the indenter. For Vickers indenter, a square is observed at the indented surface and the two indent diagonals are measured in order to calculate the average indent diagonal value, ***d***, as previously mentioned. The Vickers hardness is defined as the ratio between the maximum indentation force, ***F***, and the actual area, *i.e.* the surface of the four sides of the truncated pyramid. The Eq. I-4 can be express here as:

$$\mathrm{HV} = 1.8544\ \frac{\mathrm{F}}{\mathrm{d}^2} \tag{I-5}$$

Where HV is the Vickers Hardness Number expressed in kgf/mm^2 when the indentation force, ***F***, is in kgf and the indent diagonal, ***d***, in mm. In the following, the Vickers Hardness will be expressed in GPa by multiplying the value by 10.

Besides most common Brinell and Vickers tests, there are also some other kinds of indenters that can be used for these tests, for instance, the three-sided Berkovich (Figure I-4) or the four-sided diamond-based Knoop indenters (Figure I-5).

The area of the residual imprint left by a Berkovich of Vickers indenter is calculated from a geometrical point of view. The Vickers indenter, which has four faces, has usually a defect at its apex. During the manufacturing of such a shape, it is very difficult to make converging the four sides in only one point. That is why the summit of the pyramid is often a line, instead of a unique point. This defect leads to a bad evaluation of the area when considering an ideal geometry for calculation. Berkovich indenter has only three faces and they converge to one point. Due to this reason, Berkovich indenter has lower tip defect than Vickers and is commonly used for small penetration depth test [16].

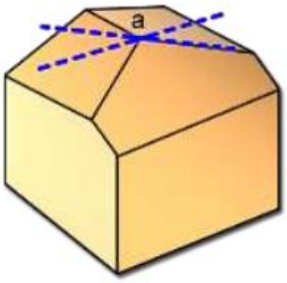

Figure I-4. *Schematic of Berkovich indenter.*

The geometry of a Knoop indenter is an extended pyramid with the length to width ratio being 7:1 and respective face angles are 172 degrees for the long edge and 130 degrees for the short edge [17]. The Knoop indenter is used particularly for very brittle materials or thin sheets, where only a small indentation may be made for testing purposes. Meanwhile it applies a low load (often 100g). This indenter is also commonly used in the adhesion test applied on the interface between a substrate and its coating.

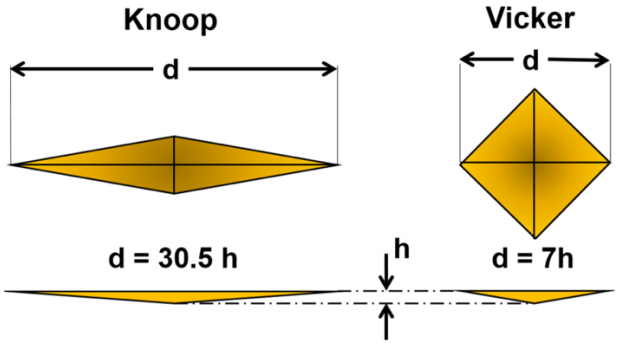

Figure I-5. *Comparison of Knoop and Vickers micro-indenter* [11].

The Knoop hardness (KHN) is defined as the ratio of the applied load F (*kgf*) divided by the projected area $\boldsymbol{A_p}$ of the indent [17]:

$$KHN = \frac{F}{A_p} = \frac{2F}{d^2[cot\frac{172.5^\circ}{2}tan\frac{130^\circ}{2}]} = 14.24\frac{F}{d^2} \quad \text{(I-6)}$$

where d is the length of the longest diagonal (*mm*).

In macro and micro scales, we can also commonly find the Rockwell test.

Rockwell test [18] determines the hardness by comparing the difference between the depth of penetration of an indenter under a large load and the penetration made by a smaller preload. The determination of the Rockwell hardness (HR) of a material involves the application of a minor load $\boldsymbol{F_0}$ of 10 kgf (~98.1N) followed by a major one $\boldsymbol{F_1}$ (Figure I-6). According to the load used in Rockwell test, it is usually applied in only macro scale test than previous mentioned methods. Firstly, use the minor load to determine the zero position. Then, apply the major load and remove while maintain the minor load. Rockwell hardness expresses as:

$$HR = N - 500h \tag{I-7}$$

where $\boldsymbol{h}$ (in mm) is the difference of the two penetration depths. The value of N depends on the indenter: 100 for spheroconical indenters and 130 for ball.

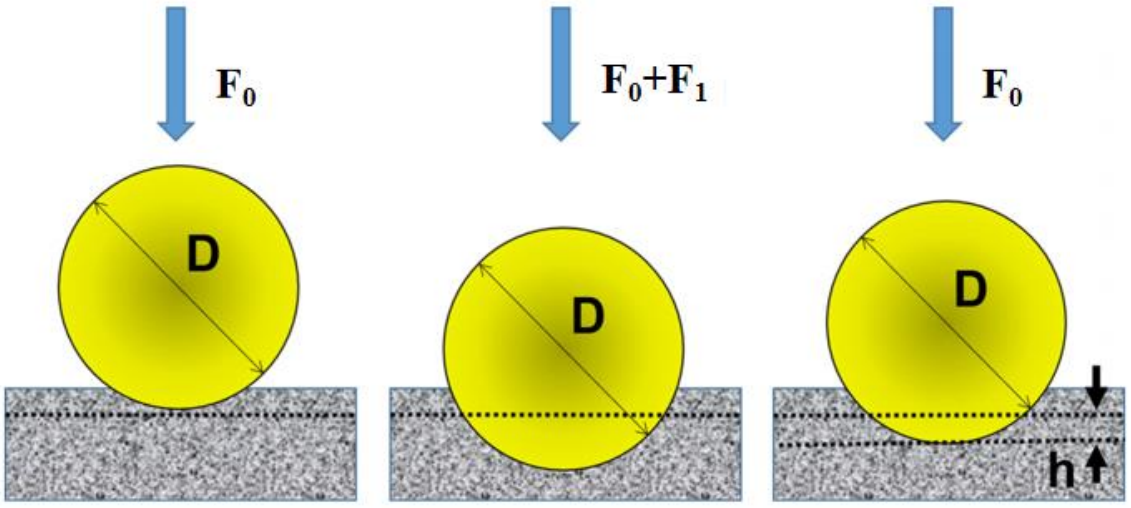

Figure I-6. *Principle of the macroindentation Rockwell test* [11].

Eq. I-7 establishes that the penetration depth and hardness are inversely proportional. In this test, there is no need for residual imprint observation and measurement. There are several $\boldsymbol{F_1}$ loads: 60, 100, and 150 kgf (1 kgf ~ 9.8 N), and several ball diameters: 1/2, 1/4, 1/8, and 1/16 inch (1 inch ~ 2.52 cm) that can be used, so the operator should use letters to specify the value of loading and indenter size (scales A, B, C, D, E, F, G, H, K, L, M, P, R, S, and V), and the most used are explained in Table I-2. Therefore, the correct notation for a Rockwell hardness value is HR followed by the scale (e.g., 62 HRC) where

C is the letter for the scale used. The spheroconical indenter used in some of the scales (also known as Brale indenter) is made with a diamond of 120° ± 0.35° included angle. The tip of the diamond is spherical with a mean radius of 0.200 ± 0.010 mm. The main international standards for Rockwell tests are ISO 6508-1 [19] and ASTM E18 [20] for metallic materials, and ISO 2039-2 [21] for plastics.

Table I-2. *Main Rockwell scales* [11].

Scale	Name	Indenter	Load (kgf)
A	HRA	120°diamond spheroconical	60
B	HRB	1/16-inch diameter (1.58mm) steel sphere	100
C	HRC	120°diamond spheroconical	150
D	HRD	120°diamond spheroconical	100
E	HRE	1/8-inch diameter (3.17mm) steel sphere	100
F	HRF	1/16-inch diameter (1.58mm) steel sphere	60
G	HRG	1/16-inch diameter (1.58mm) steel sphere	150

1.1.2 Instrumented indentation

In nano-indentation test, the indenter is pushed into the surface of the specimen producing both elastic and plastic deformation of the material as it is the case for all indentation tests. As we discuss before, the indentation in nano scale is with lower load and indent depth.

Different from the classical indentation, during an instrumented indentation test the depth is monitored throughout the experiment by means of a displacement sensor. For classical test, the key point is the diagonal of the residual imprint. While for instrumented test, the load-displacement curve should be analyzed.

During the nano-indentation process (Figure I-7), the indenter will penetrate the sample until a

predetermined maximum load L_{max} is reached (for load-controlled system), where the corresponding maximal penetration depth is h_{max}. When the indenter is withdrawn from the sample, the displacement is also continuously monitored until the zero load is reached, while a final penetration depth h_f can be measured. The slope at the beginning of unloading, denoted as $S = dF/dh$, is called the elastic contact stiffness. This process is called instrumented indentation test.

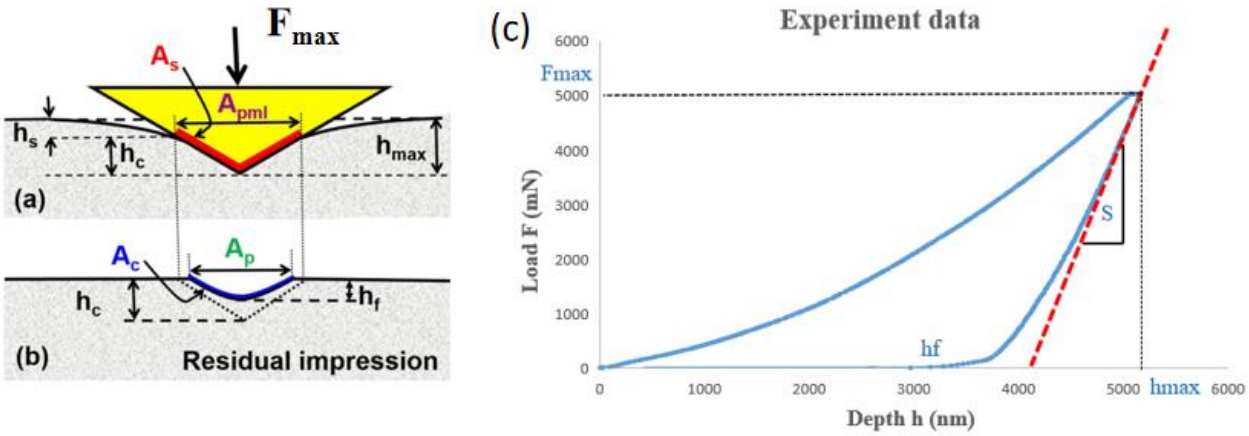

Figure I-7. *(a)The instrumented indentation test at maximum load F_{max}; (b) The residual impression after the indentation test* [11]*;(c) the load-unload curve during instrumented indentation test.*

The hardness ***H*** of the material is calculated by:

$$H = \frac{F_{max}}{A_{pml}} \tag{I-8}$$

where A_{pml} is the projected area of contact at the maximum load (as Figure I-7(a)). In Figure I-7(b) and (c), the impression and curve after the test are shown. Because of the very small scale of the nano-indentation test, the area cannot be simply observed by an optical microscope. It exists others solutions for observation at such small scale: Atomic Force Microscope (AFM), Scanning Electron Microscope (SEM)… But these technics need to make a lot of manipulation with the sample, which is time consuming and not adapted for systematical analysis. Considering this issue, some models have been proposed to analyze the load-displacement curve and extract mechanical properties (hardness, ***H*,** and Young's modulus, ***E***, for instance).

Oliver and Pharr developed a method to calculate ***H*** and ***E*** from the indentation load–displacement data, without measurement of the deformed area with a microscope [22]. For method, the contact stiffness should be determined. But for beginning of unloading part, the experimental data will be influenced by the creep of the materials and the thermal drift. The penetration depth will be over measured leading to an inaccurate slope. So, Oliver and Pharr propose to fit the unloading curve from 40% to 98% with the power-law relation:

$$F = \beta(h - h_f)^m \tag{I-9}$$

where β and m are empirically determined fitting parameters and $\boldsymbol{h_f}$ is the residual penetration depth we mentioned before, which is also determined from the curve fit.

They find out the contact stiffness S by differentiating the unloading curve fit, and evaluating the result at $\boldsymbol{h} = \boldsymbol{h_{max}}$. It gives:

$$S = \left(\frac{dF}{dh}\right)_{h=hmax} = \beta m(h_{max} - h_f)^{m-1} \tag{I-10}$$

The model of Oliver and Pharr assume an elastic sink-in of the surface surrounding the contact of the indenter (as shown in Fig. 8(a)). Thus, the amount of sink-in $\boldsymbol{h_s}$ can be given as follow:

$$h_s = \varepsilon F_{max}/S \tag{I-11}$$

where $\boldsymbol{\varepsilon}$ is the geometry factor which depends on the geometry of the indenter. For Berkovich indenters as an example, $\boldsymbol{\varepsilon}$ is 0.75. The contact depth $\boldsymbol{h_c}$ is estimated according to:

$$h_c = h_{max} - h_s = h_{max} - \varepsilon F_{max}/S \tag{I-12}$$

If we have an ideal Berkovich indenter, the contact area ($\boldsymbol{A_c}$) is simply the cross-section of a pyramid and by geometrical consideration is expressed as [23]:

$$A_c = 3\sqrt{3}\,tan^2\left(\frac{\alpha}{2}\right)h_c^2 = 24.56h_c^2 \tag{I-13}$$

where α is the angle of the Berkovich indenter, and the value is 142.3°. Then we can calculate the contact area by Eq. I-13.

As proposed by equation I-8, the calculation of hardness depends on the projected contact area determination. Since the geometry of the tip is known, by simple relation it is easy to determine the projected contact area knowing the penetration depth. Unfortunately, a real tip can slightly differ from an ideal one. This could be due to the manufacturing process and mainly to the blunting during its use. For the last one, this is changing with time, meaning the real shape of the tip evolves. The difference between the ideal tip and the real one is called tip defect and should be regularly calibrated. If the indenter displacement is larger than 200 nm during the indentation test, Troyon and Huang [24] proposed to take into account the tip defect in the expression of the contact area as follow:

$$A_c = 24.56(h_c + h_b)^2 \quad \text{(I-14)}$$

Where h_b is the truncation length of the tip defect, 24.56 is the coefficient for a perfect Berkovich pyramid.

There is still another problem: the contact depth h_c. The deformation of the surrounding surface, sinking-in or piling-up, which will cause different contact depth with the same maximum depth as shown in Figure I-8.

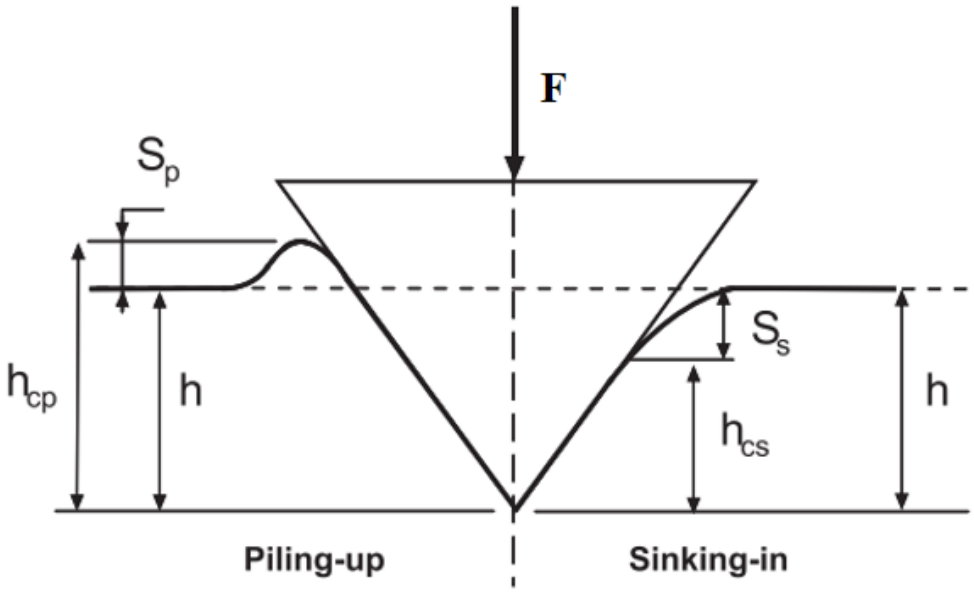

Figure I-8. *Representation of piling-up and sinking-in during an instrumented indentation test* [25].

Several methods are proposed by various authors. For sinking-in situation, Oliver and Pharr [22] calculate the contact depth h_{Cs} by the function of the maximum indentation depth ($\boldsymbol{h_{max}}$), the corresponding maximum load (F_{max}) and the elastic unloading stiffness (S) as the Eq. (I-10). And the ε is a geometry constant from the indenter. For conical punch ε = 0.72, while for sphere indenter and flat punch indenter, ε = 0.75 and 1.00 respectively.

For piling-up situation, Loubet *et al.* [26] suggest to write the contact depth, h_{Cp}, by following:

$$h_{Cp} = \alpha(h_{max} - F_{max}/S) \tag{I-15}$$

Where α is a constant equal to 1.2.

Combining the Eq. I-14, two new equations can be deduced for the sinking-in and piling-up contact area respectively (A_{Cs} and A_{Cp}):

$$A_{Cs} = 24.56(h_{max} - \frac{\varepsilon F_{max}}{S} + h_b)^2 \tag{I-16}$$

$$A_{Cp} = 24.56\alpha^2(h_{max} - \frac{F_{max}}{S} + h_b)^2 \tag{I-17}$$

1.1.3 Corrections for indentation test

For mechanical applications, the mechanical properties of the coating/substrate couple must be well determined. Within this objective, classical and/or instrumented indentation tests are reliable and fast techniques to get information about mechanical properties of the materials, especially for hardness [11]. However, it is well-known that the most efficient method developed these last decades is instrumented indentation at a nanoscale which allows a local determination of the mechanical properties. This is particularly appreciated in the case of thin coating analysis in which the hardness of the coating is directly accessible by the test under some depth restriction. However, nanoindentation is very sensitive to the roughness of the material surface. Indeed, the determination of the contact depth is a key parameter for mechanical properties evaluation. If the surface is very rough, small heights variation on the surface will affect the measure of penetration depth, resulting in a poor estimation of contact depth h_c. This is more critical for nanoindentation where roughness is not negligible in front

of shallow depths. For the studied coatings, nanoindentation is revealed as a non-efficient technique to characterize the two coatings without previous surface polishing. On the other hand, it is clear that a surface preparation can affect in a relatively great extent the mechanical properties, for example, by relaxing the residual stresses eventually present into the coating or work harden the close surface.

The major factors which influence the result of indentation are different from microscale to nanoscale [27]. In classical indentation the Indentation Size Effect (ISE) is a common phenomenon resulting in a hardness-indentation force dependence. Usually, hardness tends to increase as the indent size decreases, this phenomenon being amplified at very small scales. The second one to pay attention to is the influence of the tip defect. It is well-known in instrumented indentation and taken into account by introducing it into the computation of the contact area function. Unfortunately, this is not the case in classical microindentation where the tip defect is always neglected. Indeed, Benarioua *et al*. [28] have shown a great influence of the indenter tip defect on the hardness of DLC thin films determined by classical tests. The main problem in practice is that both indentation size effect and tip defect interact together in the hardness computation and it is often impossible to separate these two contributions. A focus on this aspect is proposed in this work by considering several relationships developed for the ISE analysis. Among them to be cited, Meyer [12] (in 1908) firstly mentioned this phenomenon, but the proposed model is not useful because it does not allow to give a hardness number representative of the hardness of the material, namely macrohardness. That is why it is often preferred the models of Li and Bradt [29], Bull and Page [23], and Nix and Gao [30] who propose to represent the indentation force or the hardness as a function of the indent diagonal. We will demonstrate here that these three models are incompatible from a mathematical point of view. However, and independently of this contradiction, the different models were applied and discussed in order to select the most appropriate model able to represent the experimental data for the tested coated samples.

As mentioned before, there are several models to correct the ISE. These three models are divided into two groups. Firstly, Li and Bradt [29] and Bull and Page [23] propose to describe the indentation force as a function of the indent diagonal. Li and Bradt propose the following relationship:

$$F = A_1.d + A_2.d^2 \quad \text{(I-18)}$$

Where A_1 and A_2 are coefficients related to the indentation size effect and to the material hardness, respectively. A_1 is expressed in N/µm and A_2 in N/µm^2.

According to Li and Bradt [29] and after introducing Eq. I-18 into Eq. I-5, the Vickers hardness can be expressed as a function of the indent diagonal by introducing a macrohardness term, HV_0, and a parameter connected to the indentation size effect, d_{LB}, as follows:

$$\frac{HV}{HV_0} = 1 + \frac{d_{LB}}{d} \quad \text{(I-19)}$$

Where HV_0 is the Vickers macrohardness (= 1,8544.A_2). d_{LB} corresponds to a characteristic scale distance connected to the ISE (=A_1/A_2). Unfortunately, this last value is not yet well-identified and not clearly associated to a physical significance.

For Bull and Page [23], the relationship is a specific polynomial law expressed as follows:

$$F = A_3.(d + d_{BP})^2 \quad \text{(I-20)}$$

Where A_3 is a constant that depends on the material, and d_{BP} a distance that, for the authors, represents the size effect or a shift due to the zero contact point between the indenter and the surface of the material.

In the same way than that applied for Li and Bradt's model, by introducing Eq. I-20 into the general Eq. I-5, the following Vickers hardness relationship is obtained:

$$\frac{HV}{HV_0} = \left(1 + \frac{d_{BP}}{d}\right)^2 \quad \text{(I-21)}$$

Where the macrohardness HV_0 equals A3 multiplied by 1.8544.

The second group of ISE models is based on the Strain Gradient Plasticity theory (SGP theory) proposed by Nix and Gao [30]. It is based on a concept of geometrically necessary dislocations, assuming that indentation deformation is accommodated by dislocations, interfering with permanent changes in the contact area. The model of Nix and Gao expresses the hardness as a function of the

indent diagonal and a macro hardness term as follows:

$$\left(\frac{HV}{HV_0}\right)^2 = 1 + \frac{d_{NG}}{d}$$

It can be also written as:

$$\frac{HV}{HV_0} = \sqrt{1 + \frac{d_{NG}}{d}} \quad \text{(I-22)}$$

d_{NG} is related to the dislocation density as defined by the Nix and Gao in the strain gradient plasticity theory.

As it can be seen clearly here, it is obvious when comparing Eq. I-19 related to the model of Li and Bradt [29], Eq. I-21 related to the model of Bull and Page [23] to Eq. I-22 related to the model of Nix and Gao [30], that there is a mathematical incompatibility. Indeed, the different equations show a linear variation of the hardness as a function of the reciprocal indentation diagonal for Li and Bradt's model [29] whereas it is the square root of the hardness for Bull and Page's model [23] and the square of the hardness for the Nix and Gao's model [30].

In addition to ISE and tip defect aspects, when indentation is performed on a coated sample, the substrate could contribute to the measured hardness (commonly called composite hardness), depending on the coating thickness and the mechanical properties of both the coating and the substrate. It is usually admitted that for a hard material deposited on a soft substrate, as soon as the indentation depth is higher than approximately 10% of the coating thickness, the substrate interferes into the hardness measurement [31]. In this case, some models are required to separate the contribution of the substrate from the apparent hardness measurement. Note that the rule of 10% could be also transposed in classical test knowing that the indent diagonal is about seven times the indentation depth for a Vickers indenter. Among many models, Jönsson and Hogmark [32] is the earliest one and is a reference for many other researchers. Chicot *et al.* [33] and Puchi-Cabrera [34] tried to solve the problem by the geometry analysis. While Korsunsky *et al*. [35] proposed an approach considering the energy aspect.

Following the methodology validated on the pseudo massive materials, Jönsson and Hogmark [32]

proposed their model. This model is applied on the corrected indentation data taking into account the influence of the tip defect. The general expression is given for the Vickers hardness by [32]:

$$\mathrm{HV_C} = \mathrm{HV_S} + \left(\frac{2\mathrm{Ct}}{\mathrm{d}} - \left(\frac{\mathrm{Ct}}{\mathrm{d}}\right)^2\right).(\mathrm{HV_F} - \mathrm{HV_S}) \quad \text{(I-23)}$$

From Eq. I-23, it is possible to extract the coating hardness as follows:

$$\mathrm{HV_F} = \mathrm{HV_S} + \frac{(\mathrm{HV_C} - \mathrm{HV_S})}{\left(\frac{2\mathrm{Ct}}{\mathrm{d}} - \left(\frac{\mathrm{Ct}}{\mathrm{d}}\right)^2\right)} \quad \text{(I-24)}$$

This model expresses the composite hardness, $\boldsymbol{HV_C}$, corresponding to the measured hardness, as a function of the substrate hardness, $\boldsymbol{HV_S}$, and the coating hardness, $\boldsymbol{HV_F}$, through a coefficient representing the part of the film involved into the composite hardness measurement. This coefficient is related to the indent diagonal, $\boldsymbol{d}$, and the coating thickness, $\boldsymbol{t}$, as well as a coefficient, $\boldsymbol{C}$, which can take two values, 0.5 or 1, depending on the mechanical behavior of the coating, brittle or ductile, respectively.

The model from Chicot and Lesage [33] based on the theory from Burnett and Rickerby [36] in which they consider the volumes of the plastic deformation zones, $\boldsymbol{V_F}$ and $\boldsymbol{V_S}$ respectively in the film and in the substrate:

$$H_C = \frac{V_F}{V} H_F + \frac{V_S}{V} H_S \quad \text{(I-25)}$$

Where $V = V_F + V_S$ and H_C is the composite hardness from experiments, while H_F and H_S are the hardness of the thin film and the substrate respectively.

Generally, it is assumed that the plastic zone has a hemispherical shape and that the size of the hemispherical plastic zone is related to the size of the Vickers imprint diagonal. According to Lawn [37], this leads to:

$$b_i = \frac{d}{2}\left(\frac{E_i}{H_i}\right)^{1/2} cot^{1/3}\xi \quad \text{(I-26)}$$

Where $\boldsymbol{b_i}$ is the plastic zone radius, $\boldsymbol{d}$ is the indentation diagonal, $\boldsymbol{\xi}$ is the indenter semi-angle and equal to 74° (in the case of a Vickers indenter), $\boldsymbol{E_i}$ is the Young's modulus and $\boldsymbol{H_i}$ the hardness of the

tested material. This equation bases on the hypothesis of continuity between the coating and the substrate. Under some assumption of the geometry [33], the composite hardness may be written:

$$H_C = \frac{3}{2}tan^{\frac{1}{3}}\xi \frac{tH_F^{\frac{3}{2}}}{dE_F^{\frac{1}{2}}} + \left(1 - \frac{3}{2}tan^{\frac{1}{3}}\xi \frac{tH_S^{\frac{3}{2}}}{dE_S^{\frac{1}{2}}}\right)H_S + \frac{3}{2}tan^{1/3}\xi \frac{t}{d}\left[\left(\frac{H_S}{E_S}\right)^{\frac{1}{2}}H_F - \left(\frac{H_F}{E_F}\right)^{\frac{1}{2}}H_S\right] \quad \text{(I-27)}$$

With t the thickness of the coating. This method is usually preferred when the Young's modulus E is convenient to get.

Korsunsky *et al.* [35] proposed a new idea to calculate the film hardness (H_F) by the work of the indentation. The total energy (W_{tot}) required to produce an indentation of depth h is given by:

$$W_{tot} = \int_0^h F_{max}\, dx = \frac{Hh^3}{3\kappa} = W_S + W_F \quad \text{(I-28)}$$

Where F_{max} is the maximum load, H is the measured hardness and κ is a parameter describing the indenter geometry, S and F subscripts stand for substrate and film respectively.

In case of fracture-dominated coating and case of plastic-dominated coating, and simplify the model and for the ease of fitting at the same time, we have the equation to present the composite hardness (H_C) by the substrate hardness (H_S) and coatings' hardness (H_F) [38]:

$$H_C = H_S + \frac{H_F - H_S}{1 + k\beta^2} \quad \text{(I-29)}$$

Where the fitting parameters H_S, H_F and k are determined by fitting to the experimental variation of H_c with β, where $\beta = \delta/t$ denotes the indentation depth normalized with respect to the coating thickness and has been termed the relative indentation depth. In the case of the cracked coating, the constant k should be proportional to thickness, whereas in the case of the plastically-deformation coating, k should be almost independent of the thickness. Korsunsky's model gives out good result when there are enough experiments point to make the fitting.

1.2 Measurement of residual stress

1.2.1 X-ray diffraction test

Residual stress, which is the stress in the materials after the manufacturing process, will cause deformation inside samples or can affect the response of the material to external mechanical solicitations during service of the coated material. X-ray diffraction (XRD) is a non-destructive technique than can be used to determine thickness, lattice parameters, residual stresses, micro strain, composition and defects in the microstructure of a material [39]. When the microstructures deformed, which means they contain residual stress, are characterized, the X-ray microbeam diffraction technique will be applied. This technique was first developed by Hirsch [40] and was applied to the study of the deformed microstructure of various metals.

In general, the XRD technique is mainly expected to observe the variations of residual stress in the coatings, especially before and after heat treatments. XRD test can help us to have some information about the change of microstructure and preferred orientation in the materials during the heat treatment [41] [42] [43].

X-ray diffraction involves probing a crystal with X-ray radiation having a wavelength (λ) close to the interradicular spacing (d), as shown in Figure I-9. The lightening angle between incoming rays and crystallographic planes is denoted $\boldsymbol{\theta}$. Usually, X-rays are generated by accelerating electrons towards a metal target in a vacuum tube. This produces a radiation spectrum from which the bright, specific wavelength can be selected. The wavelength $\boldsymbol{\lambda}$ depends on the material of X-rays generating tube. Cu, which is among the most common targets, produces a wavelength $\lambda = 1.5406\ \mathring{A}$.

These X-rays are scattered by the electron cloud surrounding every atom in the crystal. According to the Bragg's law, when two rays are diffracted on two parallel planes, the path difference is equal to ($2\boldsymbol{d\ sin\theta}$) and constructive interference will occur when this path is equal to $\boldsymbol{n\lambda}$ (where $\boldsymbol{n}$ is an integer). Bragg's law can be expressed as:

$$n\lambda = 2d\ sin\theta \tag{I-30}$$

The crystal acts as a 3D diffraction grid, so that as the sample and/or the detector are moved relative to the incident beam, a 3D array of diffraction maxima can be investigated. Each set of crystal planes will produce a diffraction spot, with the positions and shapes of the diffraction spots being inversely related to the spacings of the crystal planes and size of the crystallites. The diffraction angle $2\boldsymbol{\theta}$ is measured during the diffraction experiment.

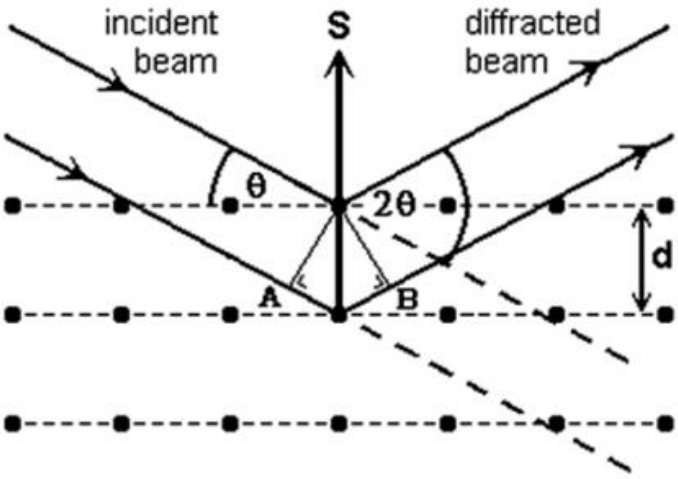

Figure I-9. *Schematic of x-ray diffraction: the conditions required for Bragg's law* [44].

Practically, several mechanical and geometrical configurations can be used. For polycrystalline materials or powders, set-ups using two circle goniometers are widely used. In the θ-2θ set-up, the source is fixed, and the sample and detector simultaneously rotate by an angle θ (resp 2θ) relative to the incident beam. In this case, the light collected by the detector is diffracted by the planes lying parallel to the surface of the specimen. This makes the technique sensitive to the orientation of the crystallites, whether it is random or not will affect the peak intensities in the diffraction diagram.

Usually, the laboratory equipment will contain a goniometer. With the goniometer, it is possible to move the X-ray source or the sample and the detector relative to each other in a very precise way. In common, the distance between the specimens and the detector will be control as a constant for all the $\boldsymbol{\theta}$ angle, which is known as Bragg-Brentano geometry. Two major basic types of goniometers are widely used: $\boldsymbol{\theta/\theta}$ goniometers, where the specimen will be fixed as Figure I-10 (a) when the X-ray

source and the detector moves; another one ***θ/2θ*** goniometer is on the contrary, for which the X-ray source is fixed while the specimen and detector are moving as Figure I-10 (b).

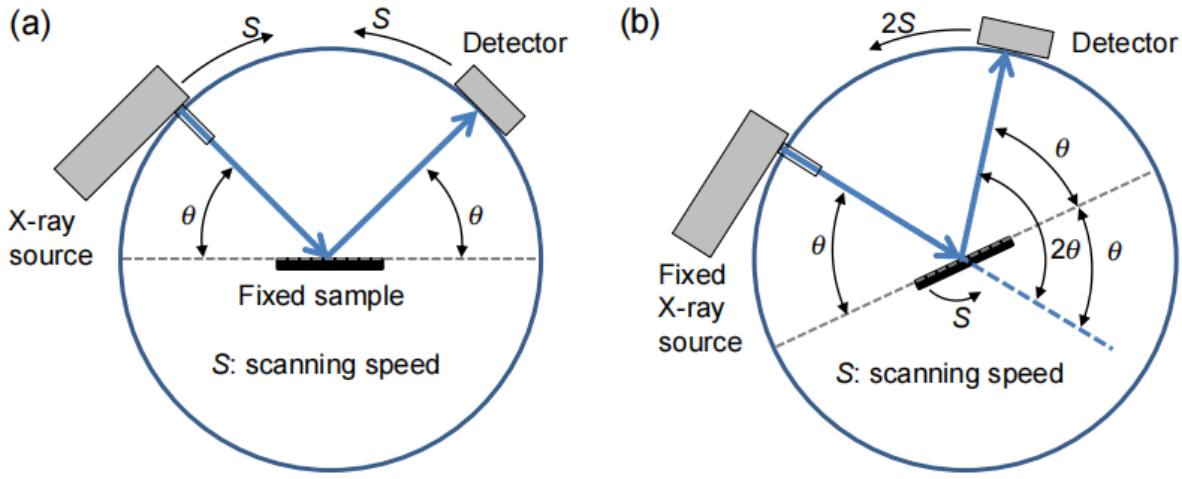

Figure I-10. *Principle of (a) **θ/θ** goniometers and (b) of **θ/2θ** goniometers* [45].

The lattice deformation in a crystalline material can produce different effects on the XRD peaks. The deformation can be uniform, resulting in first order residual stresses, or nonuniform, resulting in second and third order residual stresses (micro-deformations) [46]. Uniform deformation is homogeneous over many grains, resulting in the angular position of the XRD peak being slightly shifted according to the Bragg's law, as can be seen in Figure I-11(b). Figure I-11(a) is the specimen with non-deformed crystallographic structure, while (b) and (c) are the uniform deformation and non-uniform deformation respectively. At this scale, we speak about macro residual stresses. Non-uniform deformation is homogeneous over small domains, such as a part of a grain, and broadening of the XRD peak is observed due to increasing density in the dislocation network.

If the standard value of ***θ*** for experimental samples is known, a comparison between the standard and the experimental values can be made. Then the macro residual stress in the sample, which will cause a change in the lattice spacing (stress), can be determined as Figure I-11 (b). In another case (Figure I-11(c)) FWHM (Full Width at Half Maximum) method can be applied to monitor the micro stress, which will be introduced later.

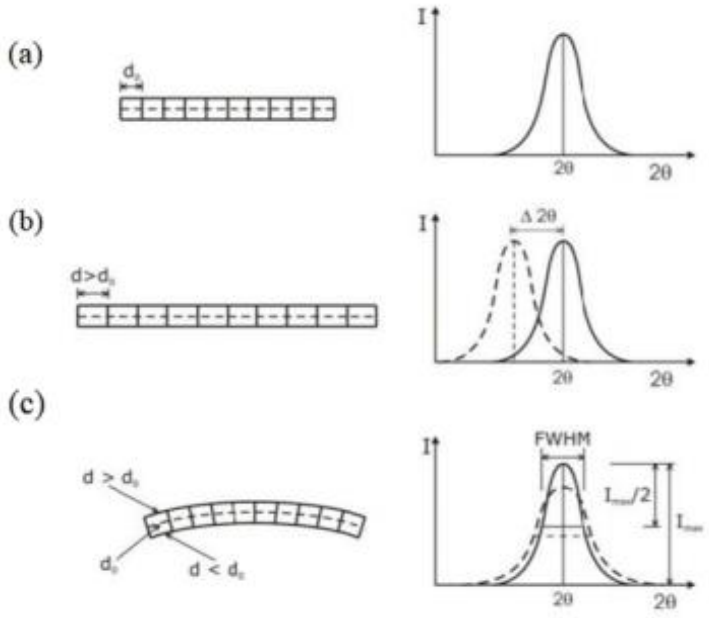

Figure I-11. *Effects of lattice deformation on XRD peaks for (a) non-deformed crystallographic structure, (b) uniform deformation (macrostresses), and (c) non-uniform deformation (microdeformations)*[46].

XRD peaks can help us to get information to calculate independently macroscopic stresses, by evaluation the shift of the peaks, and micro deformations, by analysis of peak broadening. The shift of the XRD peak allows the measurement of the elastic deformation of the crystal lattice space, while the peak broadening results from the decreasing of the crystallized size. Since the peak analysis can give us information on the structure and properties of the materials, several methods for line profile analyses are presented as follow.

Warren- Averbach method

Warren and Averbach [47][48] proposed the first theory for the broadening of the diffraction peaks, in which it was assumed that the broadening is caused by size effect and strain effect. If the measured planes are from the same family, for example {100}, {200}, the size and strain effects can be separated, as the size contribution not dependent of L and the strain coefficient is dependent of the order.

After obtaining the peaks by convolution, the discrete Fourier transform is performed to obtain the

natural logarithm of the normalized intensity expressed as:

$$lnA(g_{hkl}, L) \cong lnA^S(L) - 2\pi^2 g_{hkl}^2 L^2 < \varepsilon^2 > \quad \text{(I-31)}$$

Where A is the Fourier coefficients of total intensity, g_{hkl} is the reflection vector of each plane, $L=na_3$ is the Fourier varible and $< \varepsilon^2 >$ is the mean square strain dependent on diffraction vector.

The WA plot can be constructed by plotting function $A^S(L)$. The tangent at L=0 results in the area-weighted mean column length according to:

$$< t >_{area} = \frac{V_C}{\int_0^\infty da_t} \quad \text{(I-32)}$$

Where V_C is the volume of columns perpendicular to *{hkl}* planes, and da_t is the cross-section of columns of length t.

The size and strain components can be determined to be isotropic when $< \varepsilon >$ and $< t >$ are equal for a pair of harmonic reflections; nevertheless, if the values are different, the material is anisotropic. The line shape is directly established by the column length distribution in the domains perpendicular to the planes according to Bertaut's theory, which depends on the mean size, size distribution and shape of the coherent diffraction domains [49].

Scherrer's equation and W-H plot method (FWHM)

Besides the methods mentioned previously, there is another one named full width at half maximum (FWHM), which is a very common and convenient method. It is a qualitative or semiquantitative method of analysis of peak broadening [50]. This method is based on the Scherrer's equation [51]:

$$D = \frac{k_1 \lambda}{\beta cos\theta} \quad \text{(I-33)}$$

Where λ is the wavelength of the X-ray source, θ is the diffraction angle and the β is FWHM which is expressed in radians. k_1 is the Scherrer's constant, which depends on the crystal structure and varies from 0.62 to 2.08, and mostly it is used as 0.94 [52][53].

Scherrer's equation is a rough estimation of the average size D (crystallite size). But it does not

consider the micro strain effect. Williamson and Hall [54] also proposed a method to get the anisotropy information in broadening. They made the assumption that both size and strain broadened profiles are Lorentzian. In XRD data, the total broadening β_T of the peaks is due to the combine effect of crystallites size β_D and micro strain β_ε:

$$\beta_T = \beta_D + \beta_\varepsilon \tag{I-34}$$

From Scherrer's equation (Eq. I-33), the β_D can be expressed as:

$$\beta_D = \frac{k_1\lambda}{Dcos\theta} \tag{I-35}$$

And the broadening due to strain can be expressed as:

$$\beta_\varepsilon = 4\varepsilon tan\theta \tag{I-36}$$

The deduced formula would be:

$$\beta_T = \frac{k_1\lambda}{Dcos\theta} + 4\varepsilon tan\theta \tag{I-37}$$

After some simply deduction, Eq. I-37 can be written as:

$$\beta_T cos\theta = \frac{k_1\lambda}{D} + \varepsilon(4sin\theta) \tag{I-38}$$

The crystallites size $\boldsymbol{D}$ can be given by plotting the curve with $\boldsymbol{\beta_T cos\theta}$ versus $\boldsymbol{4sin\theta}$, where the slope is the strain $\boldsymbol{\varepsilon}$ and intercept is $\boldsymbol{\frac{k_1\lambda}{D}}$. This method can be applied when every peak of the material is known.

1.2.2 Laser Ultrasonic

Laser ultrasonic, using laser for the generation and detection of ultrasound, is a newly developed non-destructive technique for the measurement of the stress according to the acoustoelastic effect (the influence of structure or stress on the ultrasonic wave) [55][56][57]. Among nondestructive methods, ultrasonic method are the most often applied for stress evaluation because the acoustoelastic effect in materials is well studied theoretically and experimentally, equations of the

acoustoelastic effect are derived analytically as well [58].

Stress fields can be analyzed using ultrasonic waves because the stresses within a material change the characteristics of the wave (velocity, attenuation) [59]. Ultrasonic evaluation of the residual stress is based on the acoustoelastic theory. The main effect of stress on the propagation of ultrasonic wave is the variation in propagation velocity. Generally speaking, the relative change in the velocity caused by stress is proportional to the latter. The proportionality coefficient is called the acoustoelastic coefficient, which depends on the second and third order elastic constants, and also on the acoustic wave propagation and stress directions [60]. Here the final relationship between velocity and stress is given directly and there are only two directions (***x*** and ***z***) of stresses taken into account [61], because the isotropic symmetric assumption. When the displacement due to the propagation of surface wave is infinitesimal, then the relative variation of the propagation velocity can be expressed in terms of static stresses as explain in Eq. I-39 and I-40:

$$\frac{\Delta v_x}{v_0} = \frac{v_x - v_0}{v_0} = K_1\sigma_x + K_2\sigma_z \tag{I-39}$$

$$\frac{\Delta v_z}{v_0} = \frac{v_z - v_0}{v_0} = K_1\sigma_z + K_2\sigma_x \tag{I-40}$$

Where v_x and v_z (m/s) are the surface wave velocities in the presence of (σ_x, σ_z) residual stresses along the ***x*** and ***z*** directions, respectively; v_0 is the surface wave velocity in the material without stress; σ_x and σ_z are the principal stress (MPa); K_1 and K_2 are the acoustoelastic coefficients of the surface wave (MPa^{-1}). The material is assumed to be an isotropic symmetry, thus, the acoustoelastic coefficients only depend on the surface wave propagation and stress directions. The value of these acoustoelastic coefficients is obtained experimentally.

In order to solve principal stress by Eq. I-39 and I-40, the coefficients K_1 and K_2 must be determined in advance. The constants K_1 and K_2 can be determined by a calibration process: a uniaxial known stress field is applied and the corresponding surface wave velocity is measured. When the specimens are in the state of uniaxial stress, Eq. I-39 and I-40 can be simplified as [60]:

$$\frac{\Delta v_x}{v_0} = \frac{v_x - v_0}{v_0} = K_1 \sigma_x \quad \text{(I-41)}$$

$$\frac{\Delta v_z}{v_0} = \frac{v_z - v_0}{v_0} = K_2 \sigma_x \quad \text{(I-42)}$$

Obviously from Eq. I-41 and I-42, for a definite pre-stress, if the velocity of surface waves is measured parallel and vertically to the stress direction, we can get the acoustoelastic coefficients $\boldsymbol{K_1}$ and $\boldsymbol{K_2}$, respectively.

1.3 Cracks formation as indicator of toughness and adhesion

Besides the main idea that use indentation test and XRD to identify the mechanical properties of the coated samples, there are some other aspect interesting to be explored, the toughness and interfacial adhesion for instance.

Tensile test is a widely used and very convenient way to collect information about mechanical properties of bulk materials, for example the ultimate tensile strength, breaking strength and maximum elongation. In this work, this method will also be applied to the coated samples. Scratch test and indentation test can make some cracks on the specimens whose density can help to compare the toughness and adhesion among different coatings. Besides, the Rockwell adhesion test can directly tell us the interfacial tenacity is good enough or not, especially for thin coated samples.

In this part, this work is going to explore the mechanical properties from approaches which can give out different length, shape and density of cracks.

1.3.1 Tensile test

Tensile test is one of the common methods to measure the mechanical properties of bulk material. Recently, the tensile testing is also becoming increasingly common in determining the mechanical properties of materials used in aircraft structural components, bridge support sections, machine components, etc. [62]. But in this work, the adhesion of the coating to the substrate material can be

determined using simple tensile testing of coated flat metal. The method is simple but powerful and there is direct relevance to film fracture resistance and decohesion, giving important clues about the adhesion behaviors [63][64].

In tensile test, the engineering stress can be calculated by assuming the section of the sample remains constant throughout the whole experiment:

$$\sigma = \frac{F}{S_0} \tag{I-43}$$

And engineering strain is given by:

$$\varepsilon = \frac{L - L_0}{L_0} \tag{I-44}$$

Where $\mathbf{L_0}$ is the initial length and $\boldsymbol{L}$ is the length under load, $\mathbf{S_0}$ presents the initial sectional area, **F** is the force.

As section is not a constant during the test in the elasto-plastic zone when the yield stress is exceeded, true stress σ_t and true strain ε_t are defined following the real evolution of the shape of the specimen:

$$\sigma_t = \sigma(1 + \varepsilon) \tag{I-45}$$

$$\varepsilon_t = \ln(1 + \varepsilon) \tag{I-46}$$

According to the Hollomon law [65]:

$$\sigma_t = K\varepsilon_t^m \tag{I-47}$$

Where $\boldsymbol{K}$ and $\boldsymbol{m}$ are constants determined by the materials. $\boldsymbol{K}$ is the strength coefficient and **m** is the strain-hardening exponent. According to this model, the mechanical behavior of substrate could be described [65].

When the coated samples are considered, the information of the substrate is important. Because the coating shares the same strain with the substrate under it. If everything is clear for the substrate, it will be much easier to analysis the coatings' mechanical behaviors.

For the coated specimens, the stress-strain curve is shown in Figure I-12. In Figure I-12, there should be onset of cracking area and debonding area which could be observed on the corresponding specimens.

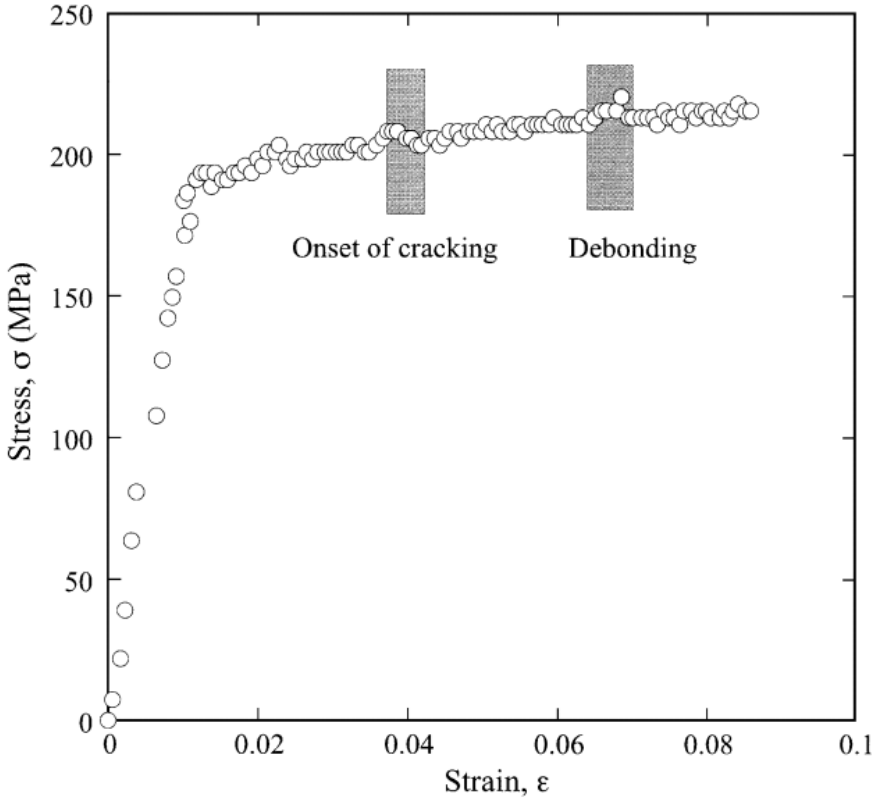

Figure I-12. *Typical stress-strain curve of tensile test. The shaded boxes indicate the general area corresponding to the onset of film cracking and debonding* [66].

One limit of classical tensile test is the fact that if you want to have access to the evolutions of the decohesion between the substrate and the coating, you must machine different width of sample. To avoid this, Millet and Iost [67] proposed a trapezoidal shape as shown in Figure I-13. Due to this special shape, the stress is relative to the width of the specimen which also represent different location on the surface during the tensile test with homogenous loading. In this way, only one sample can give out the behaviors of the material under different stresses and easily get the fracture stress. Using the Hollomon law (Eq. I-47) with a rectangular specimen of the substrate, it is therefore possible to determine the strain at each point of the specimen if the section and the load are defined.

With this test, it is possible to obtain the tenacity of the coating and the interfacial tenacity, using

the energy of crack of the coating and the total energy of interfacial rupture. With this shape of specimens, the apparition of the cracks can be defined, and it is then possible to have access of the number of cracks to define the density of cracks, the distance between each of them. Then with the localization of the first cracks, it is therefore possible to have access to real stress and know at which stress value cracks appear and see if there is a good or bad adhesion between the substrate and the coating.

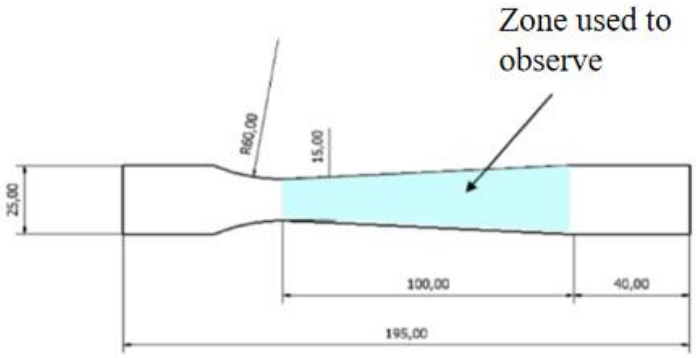

Figure I-13. *Shape and dimensions of coated tensile test specimen* [67].

During the tensile test on this trapezoidal specimen, the cracks supposed to appear firstly at the thinnest part of the shape. The highest crack density should be at this point as well, due to there is higher stress than other positions on this specimen. And with the increasing of the width and section, the crack density will decrease or even the crack will not appear close to the broad end of the sample. The qualitative analysis among different samples can be done by this method.

Y. Leterrier [68] observed that the crack density varied from the small strain to high strain as the curve shown in Figure I-14. Figure I-14 presents the three stages of the coating cracks under uniaxial loading. Stage I: at a critical strain (ε_{crit}) the sample starts cracking perpendicular to the solicitation; stage II: at a higher strain, mid-point cracking begins and transverse fragment buckling initiates; stage III: above a certain strain, the crack density becomes a constant, there are no more new cracks formed and the crack density reaches saturation.

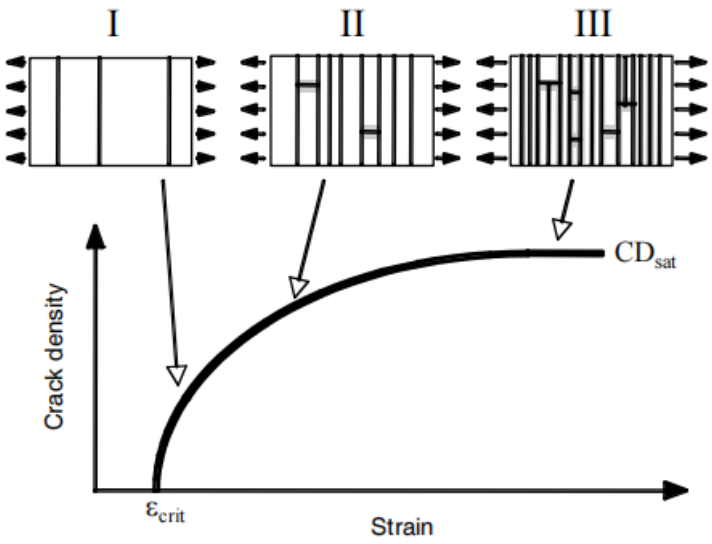

Figure I-14. *Schematic of crack density varying with increasing strain* [68].

This theory make it possible to calculate the interfacial shear strength (IFSS), which characterizes the practical adhesion of the coating layer in the mechanical sense, through the measured critical strain ($\boldsymbol{\varepsilon_{crit}}$) and crack density at saturation ($\boldsymbol{CD_{sat}}$) [68]:

$$IFSS = 1.337 t_c E_c \varepsilon_{crit} CD_{sat} \quad \text{(I-48)}$$

Where $\boldsymbol{t_c}$ and $\boldsymbol{E_c}$ are the thickness and elastic modulus of the coating.

1.3.2 Scratch test

Adhesion is a very important property of a coating. And scratch test provide a simple and reliable method to assess the adhesion of thin hard coatings [69][70]. A classical configuration of the test is a diamond stylus scratching the coated surface under an increasing load until some well-defined failure occurs at a load which is often termed the critical load, $\boldsymbol{L_c}$. Many different types of failures can be observed, including coating detachment, through-thickness cracking and plastic deformation or cracking in the coating or substrate. Due to the several different failure modes occur at the same time, the results of the test is difficult to interpret [71]. The failure modes observed in the scratch test depend on many factors and are most easily characterized in terms of the hardness of both substrate and coating (Figure I-15). For example, a very hard substrate with a very hard coating, there suppose be bulk

fracture during the scratch test. And in most common situation, it is a hard coating with a soft substrate, and it supposed to have interfacial failure of through-thickness fracture when scratching.

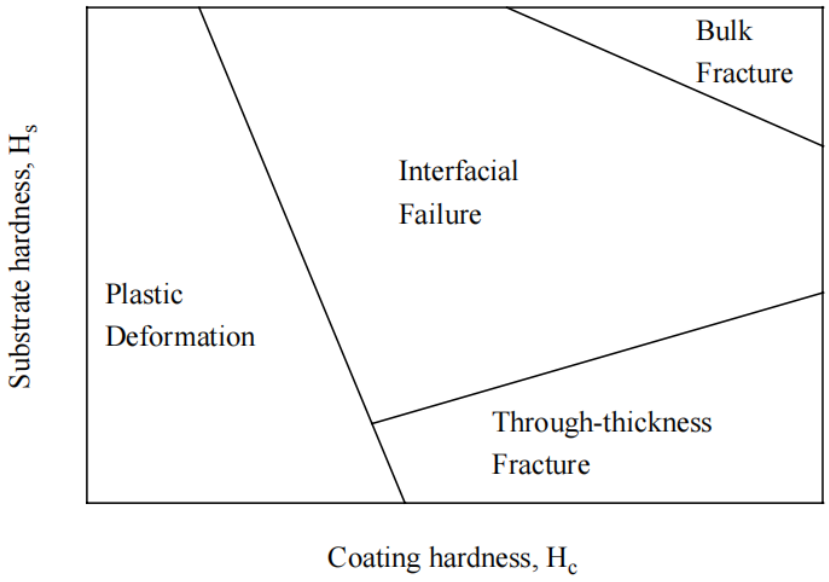

Figure I-15. *The various scratch test failure modes which dominate as a function of coating and substrate hardness (H_c and H_s, respectively)* [71].

There are some intrinsic and extrinsic parameters which will affect the measurement of critical load during the scratch test (Table I-3). Many of these intrinsic factors are instrument-specific and require a careful calibration approach if results are to be compared between instruments. While the extrinsic parameters need to be estimated before the analysis of the scratch test such as coating thickness and substrate hardness. These parameters, together with the residual stress in the coating and the Young's modulus, are an important requirement for the models of the failure mode used to generate interfacial fracture toughness. There are thus four requirements for a quantitative scratch adhesion test [71]:

1) An adhesion-related failure mode;

2) A well-defined failure mechanism;

3) A method to identify that adhesion failure has occurred, where it is located and the size of the failure;

4) A method of determining the stresses which cause failure.

Table I-3. *Intrinsic and extrinsic factors in the scratch test.*

Intrinsic	Extrinsic
Loading rate [69],[72]	Substrate properties (hardness, elastic modulus) [72]
Scratching speed [69],[72]	Coating properties (thickness, hardness, modulus, residual stress) [72]
Indenter tip radius [69]	Friction coefficient [73]
Indenter wear	Surface roughness [72]
Machine stiffness/design	

1.3.3 Indentation crack length method

Indentation aims to investigate the mechanical properties of materials. Oliver and Pharr [22] have found that for a certain type of indenter, there was a simple relationship between contact area, contact stiffness and Young's modulus. Residual stress affects the material's hardness that can be investigated by indentation tests. Thus, deducing the residual stress from indentation test is a feasible way.

Residual stresses can be determined by means of indentation tests if the stress-free state of the material is known. R. Moharrami *et al.* [74] calculate the residual stress from yield stress, and H. Liu *et al.* [75] get it by hardness and contact area. Both of them refer to the same model from S. Suresh e*t al.* [76] who have verified this method by comparing the results with finite element predictions as well as nano-indentation experimental results.

Some brittle materials are prone to exhibit cracks formation and propagation around the contact between the indenter and the surface. It will be a convenient method to get residual stress because it is easy to get the crack length from direct observation, as Figure I-16(a) shows. In the case of specimens (8 wt% yttria partially stabilized zirconia coating) tested at high temperatures (over 400℃), Z. Qu *et*

al. [77] propose to measure residual stresses using the indentation test with the stress intensity factor calculated from the cracks generated by the indenter.

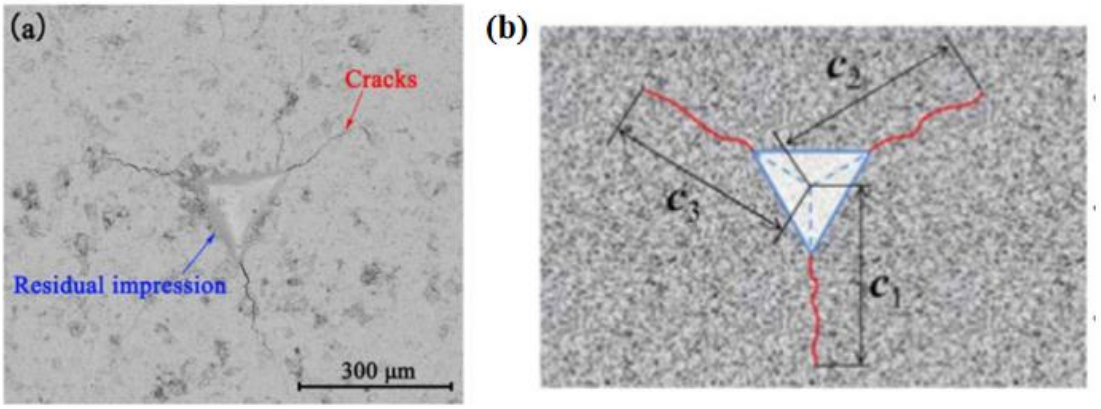

Figure I-16. *(a) Specimen surface after indentation and (b) Label the three crack length* [77].

Considering the residual stresses in the coating [78][79], based on the principle of superposition, the total stress intensity factor $\boldsymbol{K_I}$ can be given by Eq. I-49.

$$K_I = \chi P/c^{3/2} + 4\sigma_r\sqrt{t}/\sqrt{\pi} - (2\sigma_r t)/(\sqrt{\pi c}) \quad \text{(I-49)}$$

For equilibrium fracture conditions, the cracks extend when $\boldsymbol{K_I}$ reaches a critical value, $\boldsymbol{K_{IC}}$ (fracture toughness). Eq. I-49 can then be rewritten as:

$$P/c^{3/2} = (K_{IC} - 4\sigma_r\sqrt{t}/\sqrt{\pi})/\chi + ((2\sigma_r t)/(\chi\sqrt{\pi}))c^{-1/2} \quad \text{(I-50)}$$

All the parameters are listed below:

K_I is the total stress intensity factor/ $\boldsymbol{K_{IC}}$ is under the equilibrium fracture conditions (N/m$^{3/2}$);

$\boldsymbol{\chi=\delta(E/H)^{1/2}}$, δ is the geometric factor;(δ = 0.036 for a cube corner indenter [77], δ = 0.015 for Vickers indenter from *W.G. Mao et al.* [78]);

$\boldsymbol{E}$ is the Young's modulus (Pa);

$\boldsymbol{H}$ is the hardness (Pa);

$\boldsymbol{P}$ is peak indentation load (N);

$\boldsymbol{c}$ is the average crack length (m) from the three labeled cracks in Figure I-16(b);

$\boldsymbol{\sigma_r}$ is the average stress in the coating (Pa);

$\boldsymbol{t}$ is the thickness of the coating (m).

A linear relationship is found between the ratio $\boldsymbol{P/c^{3/2}}$ and $\boldsymbol{c^{-1/2}}$. Here, $(\boldsymbol{2\sigma_r t})/(\boldsymbol{\chi\sqrt{\pi}})$ and $(\boldsymbol{K_{IC}} - \boldsymbol{4\sigma_r\sqrt{t}/\sqrt{\pi}})/\boldsymbol{\chi}$ denote the slope and intercept of Eq. I-50, respectively. Then, residual stress and fracture toughness can be determined by the values of slope and intercept, respectively. Residual stress can be calculated from the result of the experiments.

1.3.4 Rockwell adhesion test

The well-known Rockwell C indentation test is prescribed by the VDI 3198 norm, as a destructive quality test for coated compounds. This method is also known as Daimler-Benz test or VDI adhesion test. It uses a Rockwell "C"-type diamond cone indenter with an applied load of 150 kg. The Rockwell adhesion test is influenced by the substrate hardness and the coating thickness. Therefore the minimum substrate hardness should be 54 HRC and the maximum coating thickness that can be accurately tested is 5 μm. This method is a qualitative test but not a quantitative one, so it is usually used for comparing different materials.

The principle of this method is presented in the upper right part of Figure I-17. A conical diamond indenter penetrates into the surface of a coated compound, thus inducing massive plastic deformation to the substrate and fracture of the coating. The 1/10th rule must be accomplished, and therefore the overall specimen thickness must be at least 10 times greater than the indentation depth. The type and the volume of the coating failure zone, exhibit in a first sight the film adhesion and secondly its brittleness. The coated specimen may be adequately evaluated, by means of conventional optical microscopy. However, the specific quality control method becomes significantly more effective, when scanning electron microscopy and spectroscopy are utilized [80].

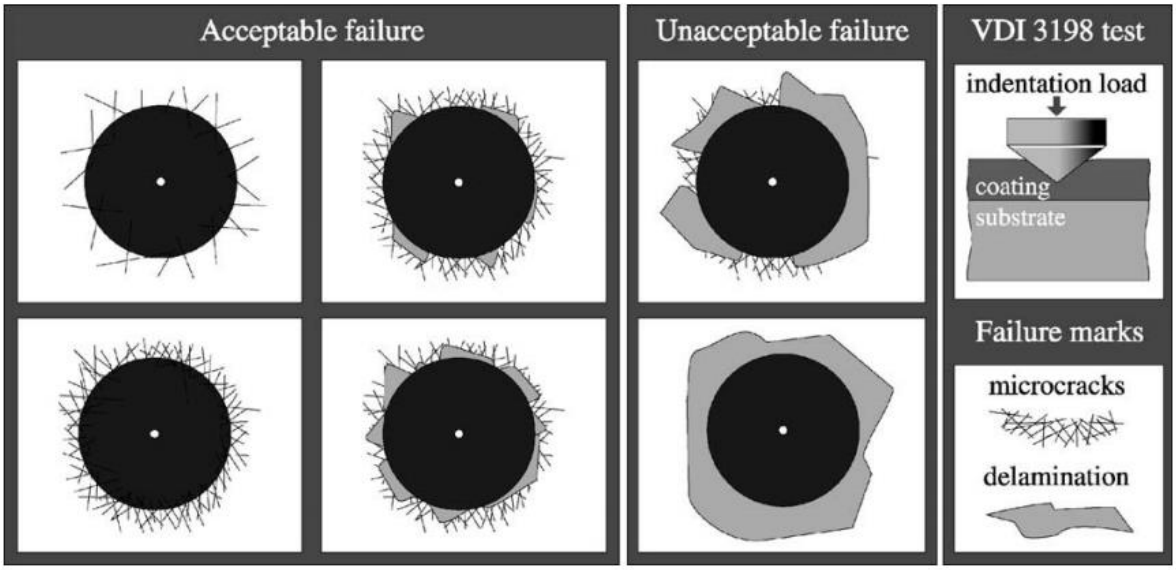

Figure I-17. *The principle of the VDI 3198 indentation test* [80].

Chapter II. Indentation test

2.1 Preparation of the samples

For deposition process, the selected substrate is a very common steel in industry, ST37, whatever the coating. Its composition is listed below in Table II-1. ST37 is also known as S235JRG2C: “S” is for Structural Steel; “235” refers to the minimum yield strength value (MPa) for a thickness ≤ 16mm; “JR” means the impact energy value is 27 J at room temperature; “G2” is a subdivided quality grade; “C” means the steel is suitable for cold drawing. In the present work, the substrate will be written ST37.

Table II-1. *Chemical composition in weight percent of ST37 steel* [81].

Elements	C	Si	Mn	P	S	Cr	Ni
w.%	0.11	0.03	0.56	0.007	0.005	0.07	0.03

The NiW and Cr-VI coatings are obtained by electroplating. For NiW, the bath is composed by 0.06 mol/L nickel sulfamate ($Ni(SO_3NH_2)_2$), 0.5 mol/L tri-sodium citrate dehydrated ($Na_3C_6H_5O_7 \cdot 2H_2O$), 0.14mol/L disodium tungstate dehydrated ($Na_2WO_4 \cdot 2H_2O$), 0.5 mol/L ammonium chloride (NH_4Cl) and 1g/L dodecyl sulfate sodium salt (surfactant). Anode is platine-titanium and the deposition rate is 0.61µm/min at a current density of 2 A/dm^2 and 0.28µm/min at 5A/dm^2, respectively named NiW-2A and NiW-5A in the following. The temperature is set at 65 °C while the pH is in the range of 8 to 8.5 by adding NH_4OH. For the Cr-VI bath, there are chromic acid 250 g/L, trivalent chromium 1-3 g/L, and the ratio of sulphate/chromic acid is 1.0-1.4%. Anode is lead-tin alloy and the deposition rate is 0.84 µm/min at a 40A/dm^{2}current density. The temperature is set at 55 °C. The parameters were chosen according to the chemical composition and the morphology of the deposits: for NiW-2A it is found a homogeneous structures in surface while for NiW-5A it is cauliflower structure (Figure II-1).

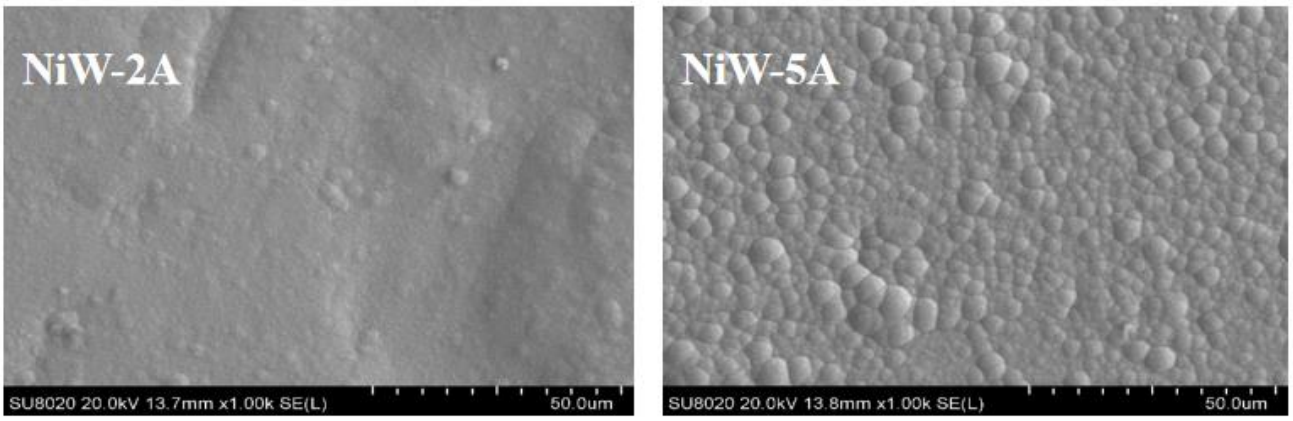

Figure II-1. *The surface structure of NiW-2A and NiW-5A observed by SEM.*

Before electroplating, the steel substrates ST37 were degreased cathodically with alkaline commercial solution ATF Systoclean at 40 °C, 3 A/dm^2 for 3 min. In a second step, they were rinsed in demineralized water, activated in H_2SO_4 solution (10% volume fraction) at room temperature for 1 min and finally rinsed again in demineralized water and immediately immersed in the plating bath. The size of both NiW-2A and NiW-5A specimens are 30 mm x 30 mm square and the coating is about 10 µm of thickness. While for Cr-VI, it is a larger plate which is 11 cm x 11 cm, and the thickness is around 100 µm. Before the indentation experiments, the Cr-VI specimen is cut into smaller pieces in order to get the appropriate size for the different tests. Figure II-2 shows us the size of Cr-VI and NiW coated specimens. Both Cr-VI and NiW coating will be investigated by indentation and X-ray diffraction tests.

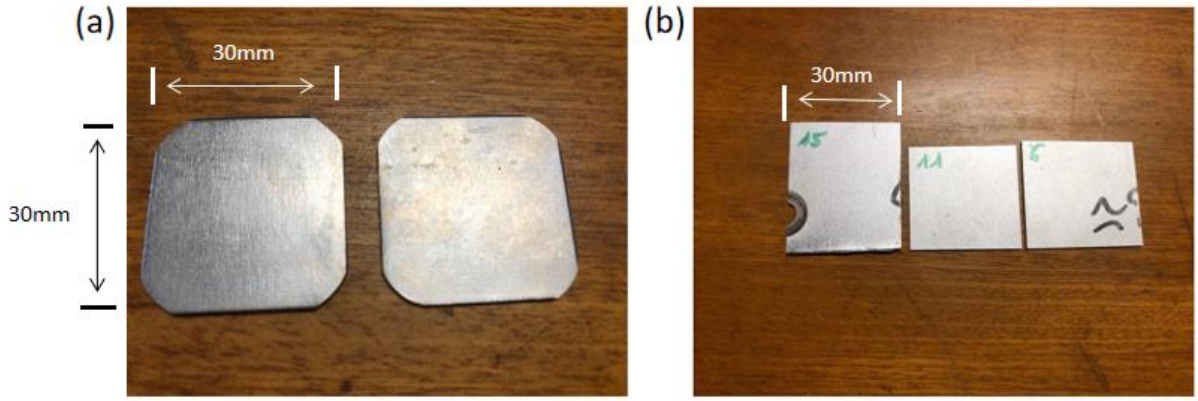

Figure II-2. *(a) NiW coated specimens; (b) Cr-VI coated specimens.*

Indentation test is strongly affected by the surface roughness. As a rule of thumb, to avoid too much influence of roughness, the penetration depth should be at least 20 times the roughness [82]. Knowing the roughness of the surface can help to find out the most suitable indentation scale. So, the surface morphology was investigated by contact profilometer KLA Tencor P16+ to investigate the roughness on the samples. Figure II-3 shows the surface morphology of the coated samples investigated on a 1 mm x 1 mm area. A closer analysis reveals some particles having several tens of micrometers large and peak height around 27.6 µm for Cr-VI, 12.0 µm for NiW-2A and 10.9 µm for NiW-5A. The roughness Sa equals 2.7 µm for Cr-VI, 1.6 µm for NiW-2A while it is 1.3 µm for NiW-5A. It is also observed that Cr-VI surface is much rougher than both NiW coatings.

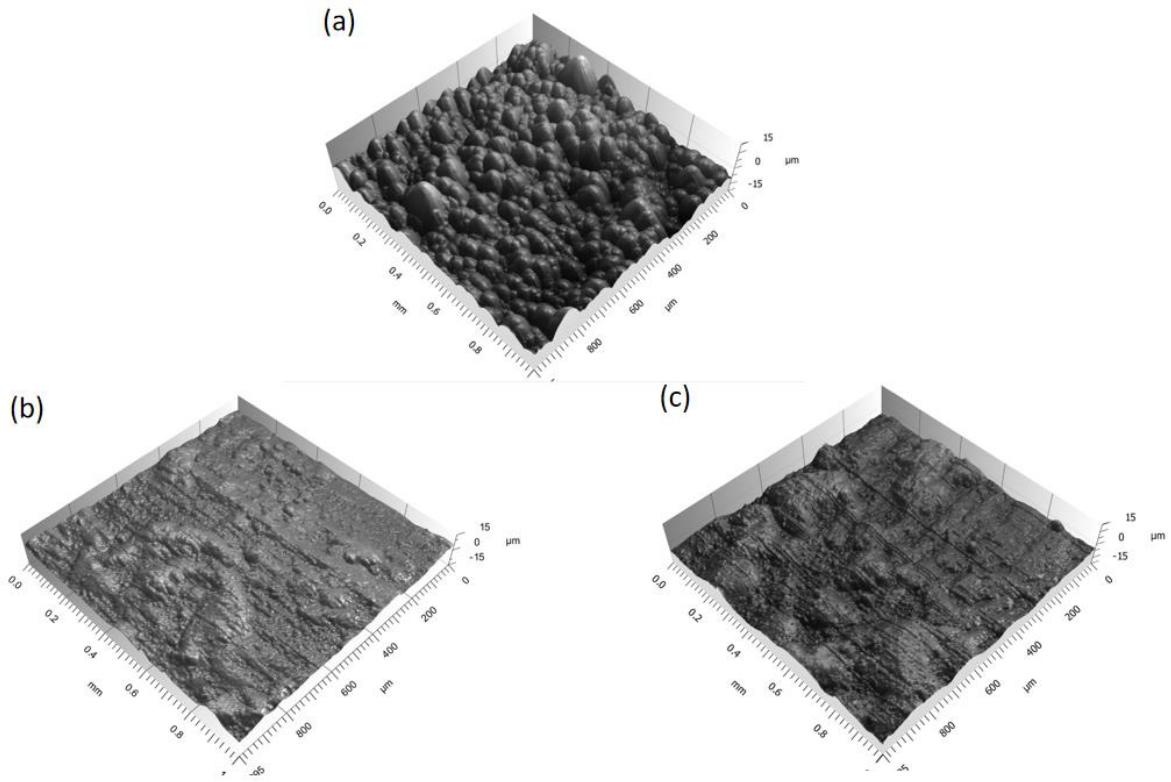

Figure II-3. *Surface topography of (a) Cr-VI, (b) NiW-5A and (c) NiW-2A coatings.*

Following the rule of thumb, that penetration depth should be at least 20 times the roughness, concerning Cr-VI coatings the penetration depth should be larger than 500 µm, more than 5 times the total thickness of the coating. At these depths, the influence of coating is low and, even with the use of multilayer models, the uncertainty of coating hardness determination will be high. That why we chose to carry out indentation tests on a cross-section perpendicularly to the normal surface to observe possible anisotropy. The specimens were embedded by hot mounting into the Multifast resin by the device CitoPress 1 (Struers, Denmark). The cross-section is mechanically polished from 100 up to 4000 grades and the final step is with silica slurry on a polishing cloth (Figure II-4).

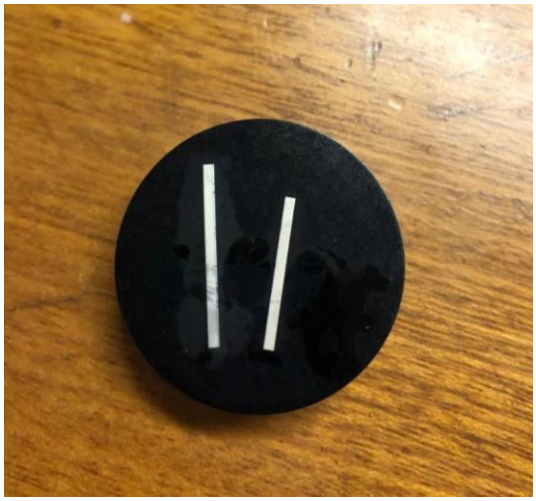

Figure II-4. *Samples prepared for indentation test.*

In this work, both classical and instrumented indentation tests are applied. All the results come from the two devices: Duramin (classical indentation) and CSM 2-107 (instrumented indentation) presented on Figure II-5.

The micro scale classical indentation instrument is Duramin (Denmark). The load range for Duramin is from 0.1 to 20 N containing 9 different loads. For each load, 10 tests will be realized and then take the average diagonals of the residual imprint in order to reduce the error. For the maximum load applied in the tests, the maximum diagonal is less than 200 μm, so the distances between each two imprints will be larger than 1mm (5 times larger than the diagonal) during the tests to neglect the influence of the plastic zone below the indent.

The micro instrumented indentation device is a CSM 2-107 (Switzerland). In this instrument, the load range is from 0.05 to 30 N, and during the test, the maximum load was set from 200nN to 10N. The load resolution of the instrument is equal to 100μN and the maximum displacement allowed by the machine is up to 100μm while the resolution is 0.3 nm.

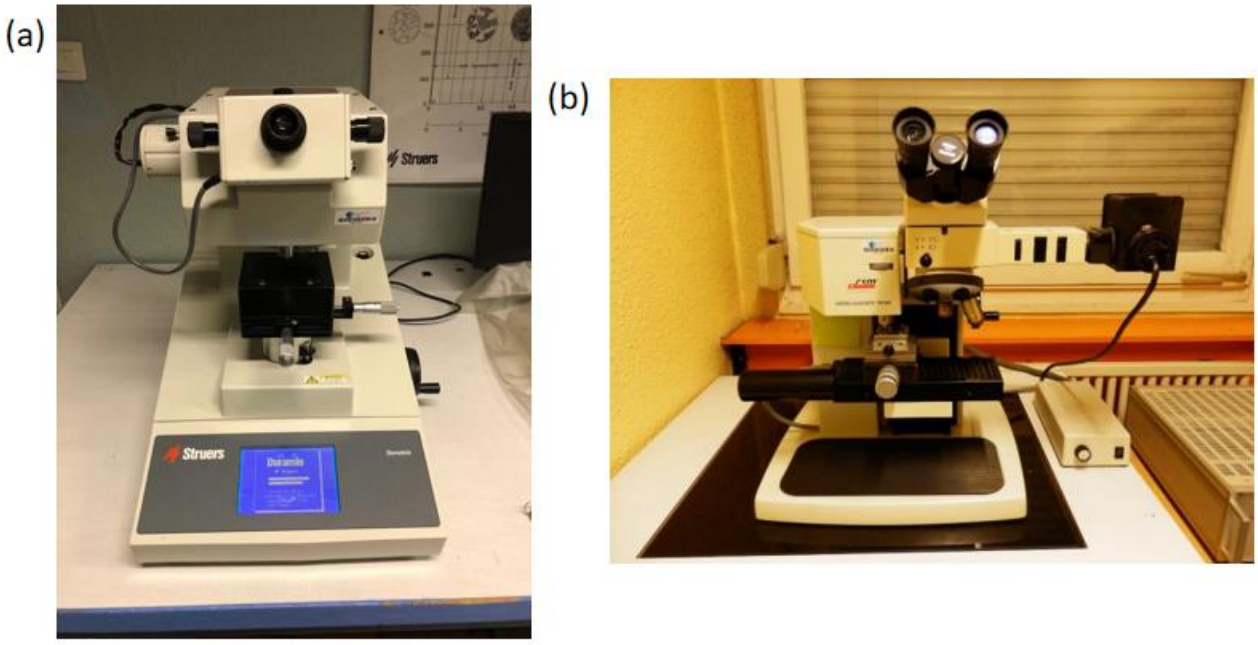

Figure II-5. *The devices used for indentation test (a) Duramin and (b) CSM 2-107.*

2.2 Results and discussion

2.2.1 Classical indentation test

To get rid of the high influence from surface roughness we suggest applying indentation test in the microindentation domain by classical indentation test.

The results of the classical indentation tests performed on the top surface of the ST37 substrate, the Cr-VI and NiW coatings as well as on a cross-section of the Cr-VI coating are collected in Table II-2.

In the first step, we are going to explain results from ST37 and Cr-VI. In second step, we will discuss about the mechanical properties of the Ni-W coatings.

Table II-2. *Indentation data of classical tests obtained on the ST37 substrate, Cr-VI and NiW coatings, i.e. indentation force in N, indent diagonal in µm and its standard deviation for each applied force and each tested materials.*

Indentation force (F in N)	0.2	0.5	1	2	3	5	10	20
ST37, Top surface	17.3 ±1.7	25.6 ±1.4	36.5 ±1.6	53.7 ±1.2	66.0 ±2.1	85.1 ±2.2	121.9 ±1.8	173.2 ±7.7
Cr-VI, cross-section	7.0 ±0.1	10.0 ±0.2	14.2 ±0.2	20.2 ±0.2	24.7 ±0.3	31.9 ±0.2	45.5 ±0.3	---
Cr-VI, Top surface	7.1 ±0.2	10.2 ±0.4	14.6 ±0.7	20.9 ±0.5	25.7 ±1.5	39.3 ±4.2	64.1 ±7.7	106.6 ±3.7
NiW_2A, Top surface	9.4 ±0.3	13.8 ±0.4	21.8 ±1.4	35.4 ±0.5	46.4 ±1.9	67.9 ±1.6	105.1 ±1.5	153.2 ±3.3
NiW_5A, Top surface	8.8 ±0.6	12.9 ±0.5	21.3 ±0.7	33.8 ±1.6	43.1 ±1.0	64.6 ±1.9	102.0 ±3.2	150.3 ±4.3

a) Indentation size effect (ISE)

The results of the classical indentation tests performed on the top surface of the bare ST37 substrate, the Cr-VI and NiW coatings as well as on the cross-section of the Cr-VI coating are collected in *Table II-2*. Different conclusions can be drawn from the lecture of this table. First, we have presented the standard deviation corresponding to 10 indentation tests performed at each indentation force. As a result, the standard deviation is always lower than approximately 5 % of the indenter diagonal.

On the base on the hardness variations observed for the substrate, the cross-section on the Cr-VI coating and on the top surface for the indentation forces lower than 3 N, we can analyze the hardness-force dependence variation through an indentation size effect approach (ISE). Figure II-6 represents the Vickers hardness (HV) variation as a function of the indentation force for ST37, Cr-VI in cross and

top sections.

For the indentation measurement on a cross-section of the Cr-VI coating, the maximum indentation force applied is 10 N and the corresponding indent diagonal is close to the coating thickness, thus indicating that the measurement could be influenced both by the resin and the substrate. Thus, the indentation force of 20 N, leading to even larger diagonals, cannot be logically applied. Furthermore, by comparing the two series of indentation performed on the cross-section and on the top surface of Cr-VI coating, it is clearly visible that for the indentation force less than 3 N, the indent diagonals are more or less similar. For forces above 3 N, the indent diagonal obtained on the top surface is higher than 35 microns. It is noticeable that this last value corresponds to an indentation depth of around 5 microns (h = d/7) indicating that the indenter displacement exceeds 10 % of the coating thickness (equal to 50 microns) [31]. Consequently, for the higher forces, the model of Jönsson and Hogmark should be applied to extract the hardness of the coating, and contrarily for the lowest forces, the measured hardness corresponds to that on the coating only.

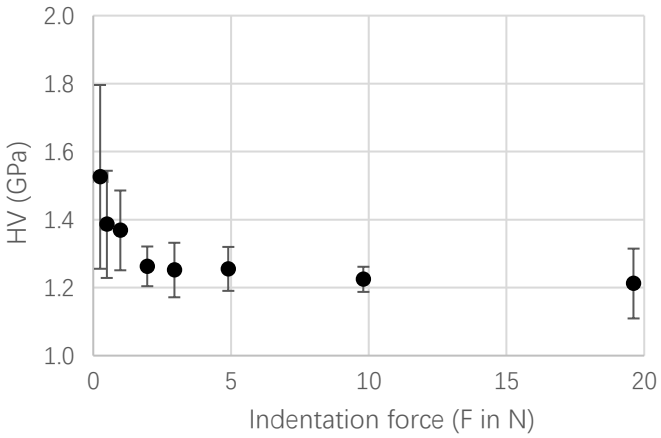

(a) ST37 steel used as substrate

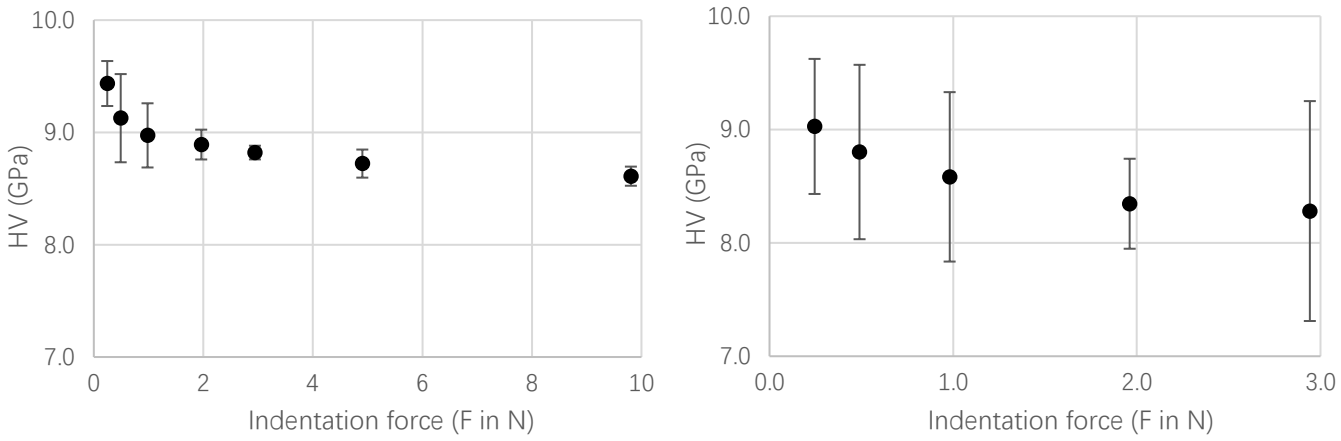

(b) Cr-VI cross-section (c) Cr-VI top surface

Figure II-6. *Vickers hardness variation as a function of the indentation force for a) the ST37 steel used as the substrate, b) on a cross-section of the Cr-VI coating and c) on the top surface of the Cr-VI coating.*

As it can be seen on Figure II-6 and as expected by the indentation size effect (ISE) on the hardness variation, it is found that the hardness increases when the indentation force decreases. It is also noted that the Vickers hardness is rather constant for indentation forces higher than approximately 2 N for all the tested samples. In addition, it is noticeable that the standard deviation is higher for the hardness measurements performed on the top surface of the Cr-VI coating compared to the ones obtained on a cross-section. This difference is due to the fact that the top surface is rougher compared to the polished cross-section, thus showing the influence of the roughness on the hardness measurements.

Now, in order to quantify ISE, we apply equations I-19, I-21 and I-22 related to the models of Li and Bradt [29], Bull and Page [23] and Nix and Gao [30], respectively. Figure II-7 shows that all the models applied to the experimental data can be adequately represented by a straight line.

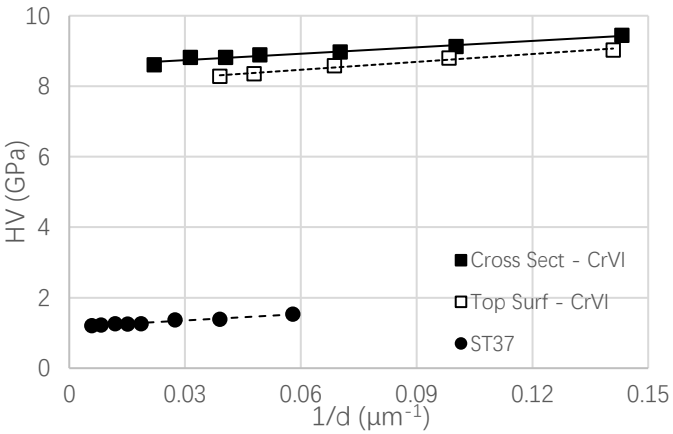

(a) Model of Li and Bradt

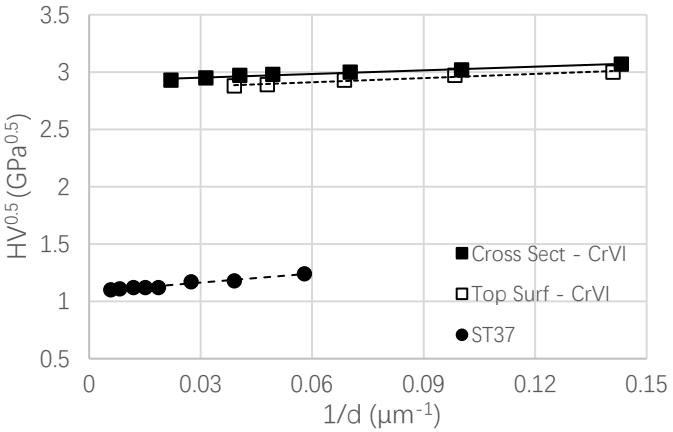

(b) Model of Bull and Page

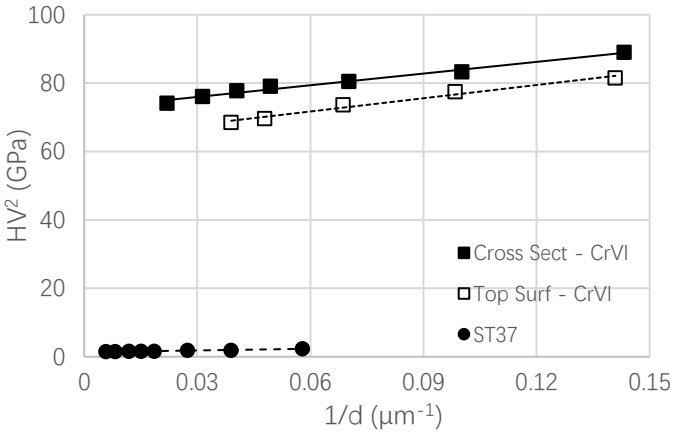

(c)Model of Nix and Gao

Figure II-7.*Application of the models of Li and Bradt (a), Bull and Page (b) and Nix and Gao (c) on the ST37 steel as substrate, the cross-section of the Cr-Vi coating and on the top surface of the Cr-VI coating with indentation force lower than 3 N.*

All the models have been fitted by a linear regression ($y = a + b*x$) and the corresponding parameters *a* and *b* are collected in *Table II-3*. From the fitting coefficients, we extracted the Vickers macrohardness HV_0 and the characteristic scale length, d_i, according to the model concerned. The values obtained are listed in *Table II-3*. The main observation which can be done from this table is that the Vickers macrohardness are found to be independent on the model applied. The macrohardness of the ST37 steel is around 1.17 GPa. For the Cr-VI coating, we obtained 8 GPa and 8.5 GPa on the top surface and on the cross-section, respectively. This apparent difference can have several origins. One possible origin could be the anisotropy between the two directions of hardness measurement due, for

example, to the presence of a residual stress state or to the growth direction of the layer. Another one could result from the polishing process. Indeed, we must note that no specific surface preparation is performed on the top surface whereas a necessary cutting and polishing is required for the preparation of the cross-section. In any case, it is impossible to attribute the slight difference to one origin rather than the other.

Table II-3. *Linear regression parameters (y = a + b*x), Vickers macrohardness HV_0 and the characteristic scale length d_i according to the model of Li and Bradt, Bull and Page and Nix and Gao obtained for the ST37 substrate, the cross-section and the top surface of the Cr-VI coating.*

Models	Parameters	ST37 steel	Cr-VI Cross-section	Cr-VI Top surface
$\mathrm{HV} = a + \frac{b}{\mathrm{d}}$	*a* (GPa)	1.17	8.56	8.02
	b (GPa*µm)	6.11	6.06	7.45
$\left(\frac{\mathrm{HV}}{\mathrm{HV_0}} = 1 + \frac{\mathrm{d_{LB}}}{\mathrm{d}}\right)$	R^2	0.97	0.97	0.98
	$\mathrm{HV_0}$ (GPa)	**1.17**	**8.56**	**8.02**
	$\mathrm{d_{LB}}$ *(µm)*	*5.22*	*0.71*	*0.97*
$\mathrm{HV^{0.5}} = a + \frac{b}{\mathrm{d}}$	*a* ($\mathrm{GPa^{0.5}}$)	1.08	2.92	2.84
	b ($\mathrm{GPa^{0.5}}$*µm)	2.65	1.07	1.21
$\left(\frac{\mathrm{HV}}{\mathrm{HV_0}} = \left(1 + \frac{\mathrm{d_{BP}}}{\mathrm{d}}\right)^2\right)$	R^2	0.97	0.97	0.96
	$\mathrm{HV_0}$ (GPa)	**1.17**	**8.53**	**8.07**
	$\mathrm{d_{BP}}$ *(µm)*	*2.45*	*0.37*	*0.44*
$\mathrm{HV^2} = a + \frac{b}{\mathrm{d}}$	*a* ($\mathrm{GPa^2}$)	1.35	72.55	63.98
	b ($\mathrm{GPa^2}$*µm)	16.27	113.95	128.98
$\left(\left(\frac{\mathrm{HV}}{\mathrm{HV_0}}\right)^2 = 1 + \frac{\mathrm{d_{NG}}}{\mathrm{d}}\right)$	R^2	0.97	0.98	0.98
	$\mathrm{HV_0}$ (GPa)	**1.16**	**8.52**	**8.00**
	$\mathrm{d_{NG}}$ *(µm)*	*12.05*	*2.01*	*2.02*

Concerning the characteristic scale lengths whatever the models, it is difficult at this step of this study to address a specific physical meaning to each parameter. In order to separate a possible influence of the indenter tip defect, an observation by scanning electronic microscope has been done at very high magnifications. Figure II-8 shows a global view of the indenter tip (Figure II-8a) and an enlargement

(Figure II-8b) to highlight the blunt of the indenter tip.

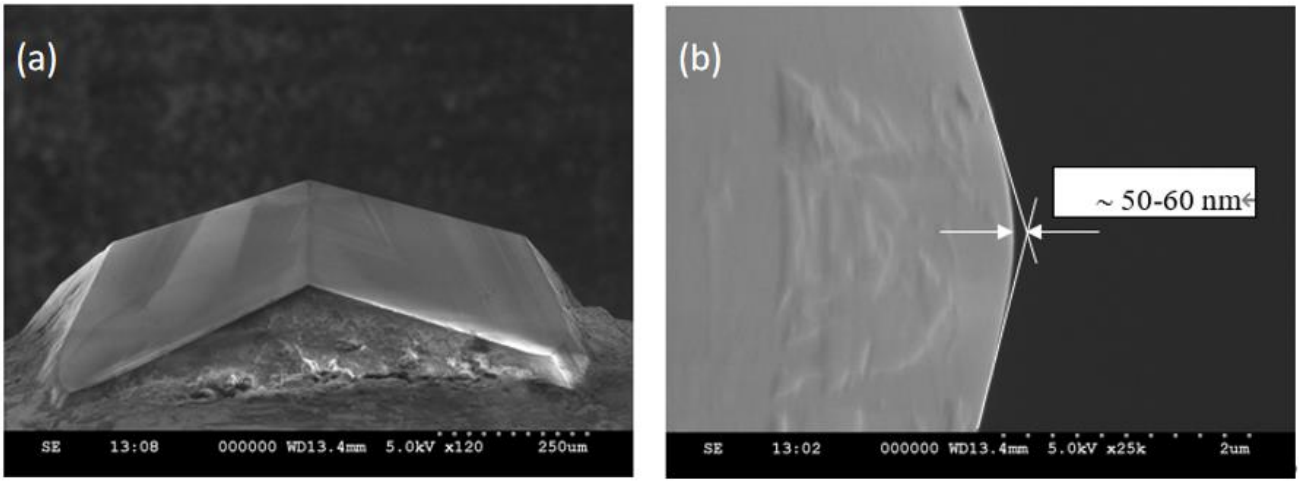

Figure II-8.*SEM observation of the Vickers indenter used in classical indentation test: (a) the main view of whole Vickers indenter and (b) the focus of the tip defect part.*

Usually, the tip defect is associated with the slight deviation from a perfect geometry of the indenter, due to its inevitable bluntness depending on its frequency of use. This tip defect can be defined in two ways, one considers the radius of the rounded tip and the second one the distance between the ideal tip and the actual rounded one as indicated in Figure II-8b. Note that if the pyramidal indenter is assimilated to an equivalent conical indenter having a half-angle at the tip of ψ equals to 70.3°, it exists a relationship between the radius of the rounded indenter tip, $\boldsymbol{R_{blunt}}$, and the indenter tip defect $\boldsymbol{h_b}$ as follows [83]:

$$h_b = R_{blunt} \cdot \left(\frac{1}{\sin\psi} - 1\right) \quad \text{(II-1)}$$

In practice, the two approaches are both rightly applicable. However in this work and within the objective to compare with parameters involved in the ISE models, we prefer the notion of indenter tip defect, $\boldsymbol{h_b}$, which allows comparing its value to a depth whereas the radius is a geometrical parameter of the indenter.

At very high magnifications on SEM observations, we have estimated the tip defect length around 50 and 60 nm. For the following, we will consider a mean value of 55 nm.

Now regarding the values of the characteristic scale lengths, it is difficult to compare these values because the distances in *Table II-3* are given equivalently to an indent diagonal. Consequently, we suggest to transpose the tip defect length as an equivalent diagonal by multiplying its value by 7 according to the geometry and the angles of the Vickers pyramid. Following this statement, we obtain a value close to 0.4 μm which can be compared to the value of d_{BP} resulting from the application of the model of Bull and Page [23]. It is also interesting to note that even if Bull and Page attribute this value of d_{BP} by a shift at the zero-contact, numerous authors such as Saka and Tanaka [84] suggest to calculate the hardness by taking into account the tip defect in instrumented indentation, here it is also applied to classical test as follows:

$$H = \frac{F}{26.43\ (h+h_b)^2} \tag{II-2}$$

Where $\boldsymbol{h_b}$ is the tip defect length.

From this equation, we can express the indentation force as a function of the indenter displacement as follows:

$$F = 26.43\ H\ (h + h_b)^2 \tag{II-3}$$

Which is equivalent to Eq. I-20 proposed by Bull and Page when replacing the indentation depth, $\boldsymbol{h}$, by the indent diagonal, $\boldsymbol{d}$, with the ratio of 7. In this case, Eq. II-3 becomes:

$$F = \frac{H}{1{,}8544}(d + d_b)^2 \tag{II-4}$$

Consequently, we suggest rediscussing the indentation size effect after recalculation of all the indentation data taking into account the indentation size effect with rewriting Eq. II-4 as follows:

$$HV = 1.8544\ \frac{F}{(d+d_b)^2} \tag{II-5}$$

Where $\boldsymbol{d_b}$ equals $7\boldsymbol{h_b}$ so $\boldsymbol{d_b}$ = 0.4 μm.

Figure II-9 presents the models applied to the corrected values of the Vickers hardness (Eq. II-5) which considers the influence of the tip defect.

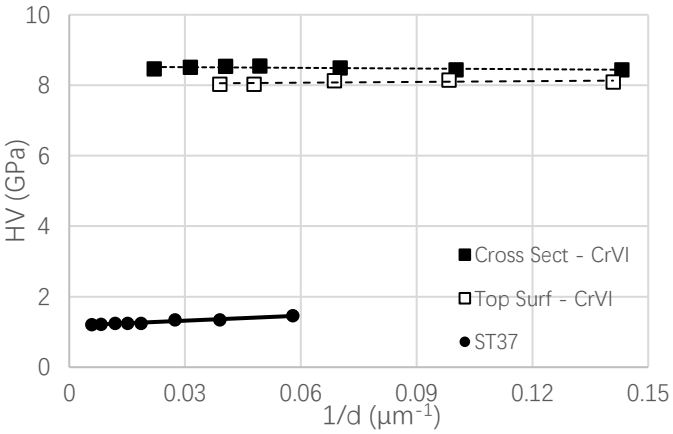

(a) Model of Li and Bradt

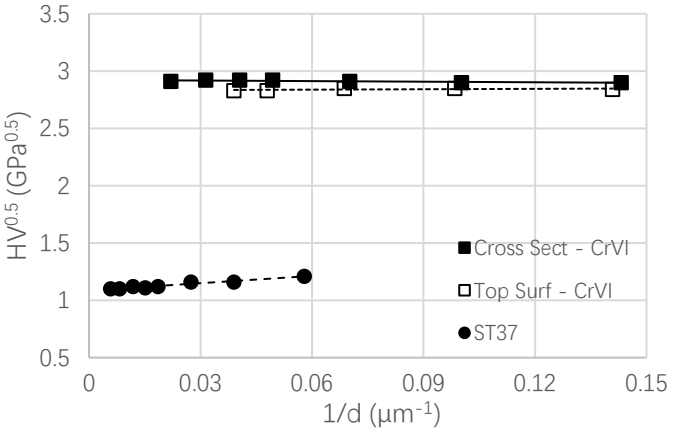

(b) Model of Bull and Page

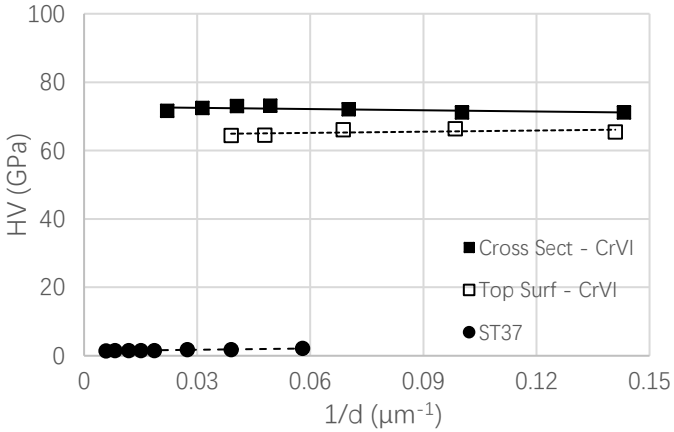

(c) Model of Nix and Gao

Figure II-9. *Application of the models of Li and Bradt (a), Bull and Page (b) and Nix and Gao (c) on the ST37 steel as substrate, on the cross-section and on the top surface of the Cr-VI coating with indentation force lower than 3 N.*

As it can be seen for the Cr-VI coating, both on the top surface and on the cross-section, the hardness is relatively constant thus indicating that the indentation size effect comes only from the influence of the tip defect. Independently of that for validation, we have extracted from a linear fitting the corrected values for the Vickers macrohardness and the characteristic scale lengths which are collected in Table II-4.

Table II-4. *Linear regression parameters (y = a + b*x), Vickers macrohardness HV_0 and the characteristic scale length d_i according to the model of Li and Bradt, Bull and Page and Nix and Gao obtained for the ST37 substrate, for the cross-section and the top surface of the Cr-VI coating applied to the corrected hardness values.*

Models	Parameters	ST37 steel	Cr-VI Cross-section	Cr-VI Top surface
$\mathrm{HV} = a + \frac{b}{\mathrm{d}}$	*a* (GPa)	1.18	8.53	8.03
	b (GPa*μm)	4.76	-0.64	0.73
$\left(\frac{\mathrm{HV}}{\mathrm{HV_0}} = 1 + \frac{\mathrm{d_{LB}}}{\mathrm{d}}\right)$	R^2	0.95	0.37	0.30
	$\mathrm{HV_0}$ (GPa)	**1.18**	**8.53**	**8.03**
	$\mathrm{d_{LB}}$ *(μm)*	*4.03*	*-0.08*	*0.09*
$\mathrm{HV^{0.5}} = a + \frac{b}{\mathrm{d}}$	*a* ($\mathrm{GPa^{0.5}}$)	1.09	2.92	2.83
	b ($\mathrm{GPa^{0.5}}$*μm)	2.11	-0.17	0.12
$\left(\frac{\mathrm{HV}}{\mathrm{HV_0}} = \left(1 + \frac{\mathrm{d_{BP}}}{\mathrm{d}}\right)^2\right)$	R^2	0.95	0.65	0.24
	$\mathrm{HV_0}$ (GPa)	**1.19**	**8.53**	**8.01**
	$\mathrm{d_{BP}}$ *(μm)*	*-0.06*	*0.04*	*1.94*
$\mathrm{HV^2} = a + \frac{b}{\mathrm{d}}$	*a* ($\mathrm{GPa^2}$)	1.37	72.86	64.48
	b ($\mathrm{GPa^2}$*μm)	12.59	-11.96	11.51
$\left(\left(\frac{\mathrm{HV}}{\mathrm{HV_0}}\right)^2 = 1 + \frac{\mathrm{d_{NG}}}{\mathrm{d}}\right)$	R^2	0.96	0.41	0.30
	$\mathrm{HV_0}$ (GPa)	**1.17**	**8.54**	**8.03**
	$\mathrm{d_{NG}}$ *(μm)*	*9.19*	*-0.16*	*0.18*

It is remarkable that the Vickers macrohardness values are not affected by the correction of the indenter tip defect, but this is not the case for the distances. For the coating, both on the cross-section and on the top surface, the values of the distances have been drastically reduced. If some parameters take negative values, this is due to the fact that the correction of the indenter tip defect is 0.4 μm which must be compared to d_{BP} according to the model of Bull and Page, higher than 0.37 and lower than 0.44 shown in *Table II-3* for the cross-section and the top surface, respectively. In fact, we can reasonably consider that the Vickers hardness is constant both on the cross-section and on the top surface of the Cr-VI coating.

However, it is not the case for the ST37 steel substrate where a non-zero value is obtained for d_{BP}. It is generally admitted that the hard materials are not affected by the indentation size effect, which is verified here, but for metallic materials, ISE can be observed and attributed to a work hardening generated during the surface preparation of the sample. Nevertheless, even if we admit a possible ISE for metallic materials, it is very difficult here to consider one ISE model rather than another. They are all able to adequately represent the indentation force versus the indent diagonal for the models of the first group, and the hardness variation versus the reciprocal indent diagonal for the model of the second group.

b) Substrate effect

For the Cr-VI coating, it will be not reasonable to apply the model only on three data points because the results greatly depend on the number of experimental data. That is why only the two NiW coatings will be analyzed with the model of Jönsson and Hogmark.

In a second step, to analyze the hardness variation observed for the two NiW coatings, NiW-2A and NiW-5A, we have recalculated the experimental data by applying Eq. II-5 in order to drastically reduce, even eliminate, the influence of the tip defect. The results of NiW-2A and NiW-5A are shown in Table II-2. We can also reasonably admit that the coating hardness has a constant value. To separate the contribution of the substrate in the hardness measurement, we selected the model of Jönsson and Hogmark [32] which presents the advantage, compared to the others available in literature, to be applicable with only few points which is usually the case in classical microindentation. This model expresses the composite hardness, $\boldsymbol{H_C}$, corresponding to the measured hardness, as a function of the substrate hardness, $\boldsymbol{H_S}$, and the coating hardness, $\boldsymbol{H_F}$, through a coefficient representing the part of the film involved into the composite hardness measurement. This coefficient is related to the indent diagonal, $\boldsymbol{d}$, and the coating thickness, $\boldsymbol{t}$, as well as a coefficient, $\boldsymbol{C}$, which can take two values, 0.5 or 1, depending on the mechanical behavior of the coating, brittle or ductile, respectively. The general expression is given for the Vickers hardness by:

$$HV_C = HV_S + \left(\frac{2C \cdot t}{d} - \left(\frac{C \cdot t}{d}\right)^2\right).(HV_F - HV_S) \quad \text{(II-6)}$$

From Eq. II-6, it is possible to extract the coating hardness as follows:

$$HV_F = HV_S + \frac{(HV_C - HV_S)}{\left(\frac{2C \cdot t}{d} - \left(\frac{C \cdot t}{d}\right)^2\right)} \quad \text{(II-7)}$$

Consequently, there are two possibilities to apply the model of Jönsson and Hogmark [32]. One is the use of Eq. II-7 when the Vickers hardness of the substrate is known and when the value to the constant C is attributed basing on the mechanical behavior of the coating. Nevertheless, some authors like Iost *et al.* [85] suggest keeping this parameter free in order to better fit the experimental data and to discuss about the mechanical behavior of the coating accordingly to the value taken by C. These authors suppose that there exists a hybrid or intermediate mechanical behavior.

These two methodologies will be applied on the experimental data to the two NiW coatings for which all hardness measurements are affected by the substrate when applying the simple rule of 10%. Indeed, starting from this assumption, the substrate should interfere as soon as the indenter displacement is higher than 10 % of the coating thickness which is equal to 10 µm, *i.e.* 1 µm corresponding to an indent diagonal of 7 µm. For NiW coatings, all the indent diagonals are higher than this limit value. Figure II-10 presents the film hardness determined point by point (white and black circles) when the constant C of the model is fixed to 0.5 and 1 depending on the mechanical behavior of the material which is a priori not known, *i.e.* brittle and ductile respectively. When the constant C is considered as a free-parameter as suggested by Iost *et al*. [85], the experimental Vickers hardness (black squares) is then fitted by the model of Jönsson and Hogmark, thus leading to the black solid curve.

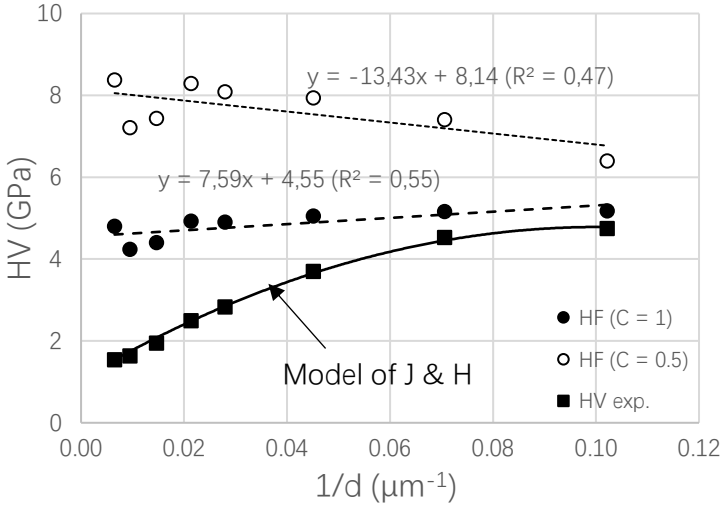

(a) NiW-2A.

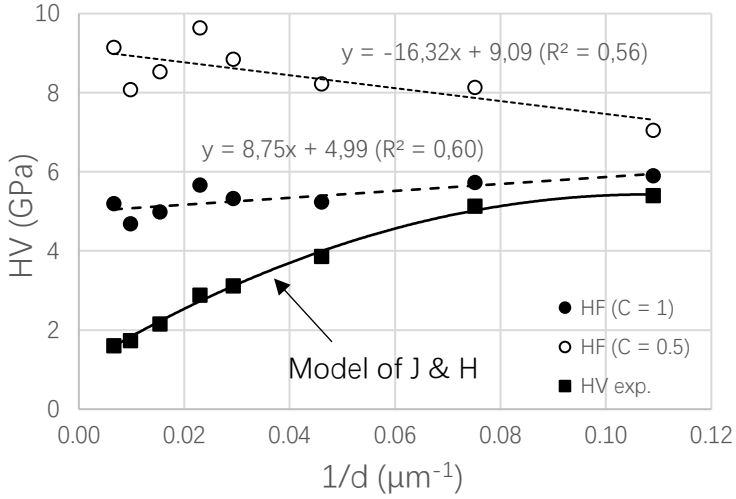

(b) NiW-5A.

Figure II-10. *Application of the model of Jönsson and Hogmark to the Vickers hardness obtained on the NiW coating a) 2A and b) 5A by fixing the constant C equals to 0.5 and 1 and by keeping constant C as a free-parameter (black solid line).*

In Figure II-10, the black squares represent the experimental Vickers hardness measured on the top surface of the NiW coatings taking into account the correction of the indenter tip defect by applying Eq. II-7. As said here before, two material behaviors could be considered as possible to apply the model of Jönsson and Hogmark. The black and white circles result from the application of Eq. II-7 of the model by fixing the constant C equal to 1 or 0.5, respectively. That is to say, by assuming that the mechanical behavior of the coating is ductile or brittle, respectively. This calculation is obtained one

point by point. It is noticeable on Figure II-10 that the value of constant C has a great influence on the Vickers hardness of the coating, a ratio varying between 1.2 and 2 depending on the reciprocal indentation depth is found between the two series of coating hardness. The Vickers hardness thus obtained for the coating resulting from the application of the Jönsson and Hogmark model to one point after another by fixing the value of the constant C can be represented by a linear variation as a function of the reciprocal indent diagonal as shown in Figure II-10 whatever the value of the constant C. Consequently, the film Vickers hardness is fitted by a linear regression according to the model of Bull and Page [23]. The values obtained for the Vickers macrohardness of the coating and of the characteristic scale length d_{BP} are collected in Table II-5.

Table II-5. *Vickers macrohardness HVF_0 and the characteristic scale length d_0 obtained for the NiW coatings according to the model of Bull and Page applied to the film hardness variation obtained by the application of the model of Jönsson and Hogmark.*

Constant C	Parameters	NiW coating 2A	NiW coating 5A
C = 1	**HVF_0 (GPa)**	**4.55**	**4.99**
	d_{BP} *(μm)*	*1.67*	*1.75*
C = 0.5	**HVF_0 (GPa)**	**8.14**	**9.09**
	d_{BP} *(μm)*	*-1.65*	*-1.79*

It is interesting to note that the Vickers macrohardness of the NiW-5A coating obtained with the constant C equal 0.5 is close to 1.8 times more than that obtained when the constant C is equal to 1. The problem here is that no physical meaning can help us to select one constant value rather than the other because no cracks are visible around the indent. On the other hand, we can notice that the characteristic scale lengths seem to be independent on the deposition conditions and have opposite values when considering C equal to 1 and 0.5. It should be added that a negative value has no physical meaning that could indicate that the constant C equal 1 should be more appropriate to calculate the Vickers hardness of the coatings, confirming also that the hardness of the NiW coating has a constant value.

In order to validly discuss on the value that the constant C has to be given, we suggest keeping this parameter free as suggested by Iost *et al*. [85]. In order to do so, we use the solver of Excel to determine the value of the constant C and the Vickers macrohardness of the coating. Following this approach, we suppose that the Vickers hardness of the coating should have a constant value, as indicated here above and as this was obtained for the Cr-VI coating. The black solid curve in Figure II-10 fitting the experimental Vickers hardness represents the application of the Jönsson and Hogmark model when the constant C is a free-parameter. Following this procedure, we obtained the values collected in Table II-6.

Table II-6. *Vickers macrohardness HVF_0 and the constant C obtained for the NiW coatings.*

Parameter	NiW coating 2A	NiW coating 5A
HVF_0 (GPa)	**4.38**	**5.0**
C	*1.07*	*1.0*

A main result from this approach is that the constant C values obtained for both NiW coatings are found very close to 1 thus confirming the assumption made before. Note that for the NiW-5A coating, the Vickers macrohardness indicated in *Table II-5* and *Table II-6* are the same since the constant C is equal to 1. The difference obtained for the NiW-2A coating results from the difference in the constant C, 1.07 in *Table II-6* while it is 1 in *Table II-5*. Finally, we can conclude that the Vickers macrohardness of the NiW coating under the conditions 2A has a hardness number of 4.4 GPa whereas it is slightly higher for the other condition of deposition, *i.e.* 5 GPa.

2.2.2 Instrumented indentation test

Besides the classical test, the instrumented indentation test also applied for the Cr-VI specimen on the cross-section surface. This test can help us to make the comparison between classical and instrumented tests. Instrumented test can give out the result of ***E*** (Young's modulus) as well.

The first step is to consider the contact area of the test, while there is tip defect influence[86][87]:

$$\sqrt{A_c} = \left(\sqrt{\pi} tan\psi\right) \cdot \left[h_c + h_b \left(1 - \exp\left[-2\frac{h_c}{h_b}\right]^{\frac{3}{2}}\right)\right] \quad \text{(II-8)}$$

Where $\sqrt{\pi}tan\psi$ is a constant due to the shape of indenter, for Vickers, it is 24.5; h_c is the contact depth from results in nm which is known by Eq. I-12 in Chapter I; h_b is the effective truncation length of the indenter tip, which can be determined by the microscopic observation and equals 350 nm in this work.

In instrumented indentation test, the machine compliance should be considered. Because the force not only applied on the samples, but also on the parts of the measuring machine. The compliance will lead to higher indentation depth than real and turns out a lower hardness and elastic modulus [88].

In some cases, the frame compliance of the instrument will be corrected by the device automatically using a constant value determined once forever. But compliance is not always a constant and differs from one material to another one. In this work, the CSM device used for instrumented indentation has no automatic correction for compliance. So, in the analysis, compliance must be considered. From the relationship between contact area and the reciprocal of slope S, the compliance of device C_f can be calculated by the relationship between $1/S$ and $1/(A_C^{1/2})$. Both Chicot *et al*. [86] and Ullner *et al.* [89] proposed their own relationship .And another method is a classical one which calculate the compliance from the $1/S$ and the root of maximum load F [22]. These three methods are shown in Figure II-11 and the result of compliance are list in *Table II-7*, where C_{fD}, C_{fU} and C_{fP} are the compliance calculated by the three methods.

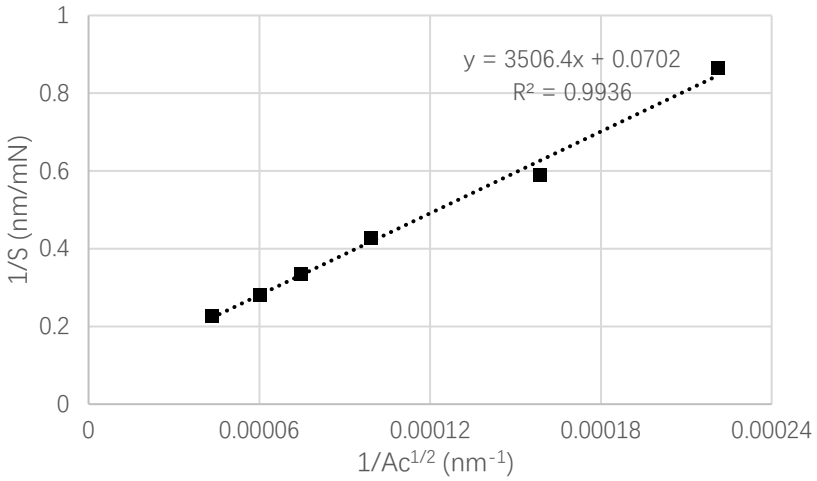

(a) Method suggested by Chicot *et al.*

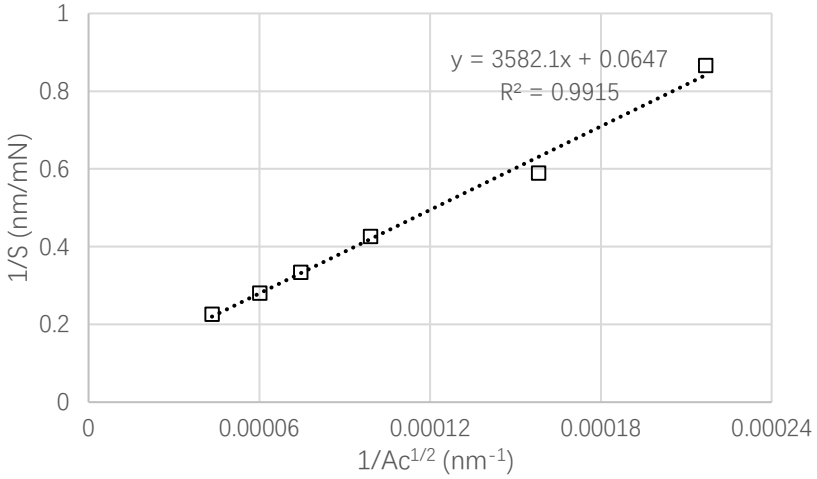

(b) Method suggested by Ullner *et al.*

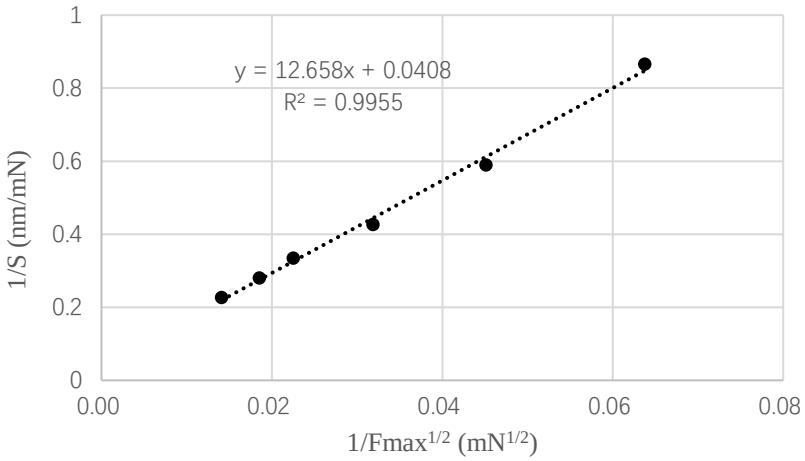

(c) Classical method for compliance.

Figure II-11. *Three methods to calculate the compliance of device: relationship between slope* ***S*** *and contact area suggested by (a) Chicot et al., (b) Ullner et al. and (c) relationship between slope* ***S*** *and maximum load.*

After comparing Chicot *et al.* and Ullner *et al.* models, as shown in Figure II-11 a and b, they give out very close result in analysis (as Table II-7 shows), so here will only presented the results from Chicot *et al.* method.

Table II-7. *The calculated compliance value of two models.*

Model	**Chicot *et al.* C_{fD}**	**Ullner *et al.* C_{fU}**	**Classical C_{fP}**
Compliance value (nm/mN)	0.0702	0.0647	0.0408

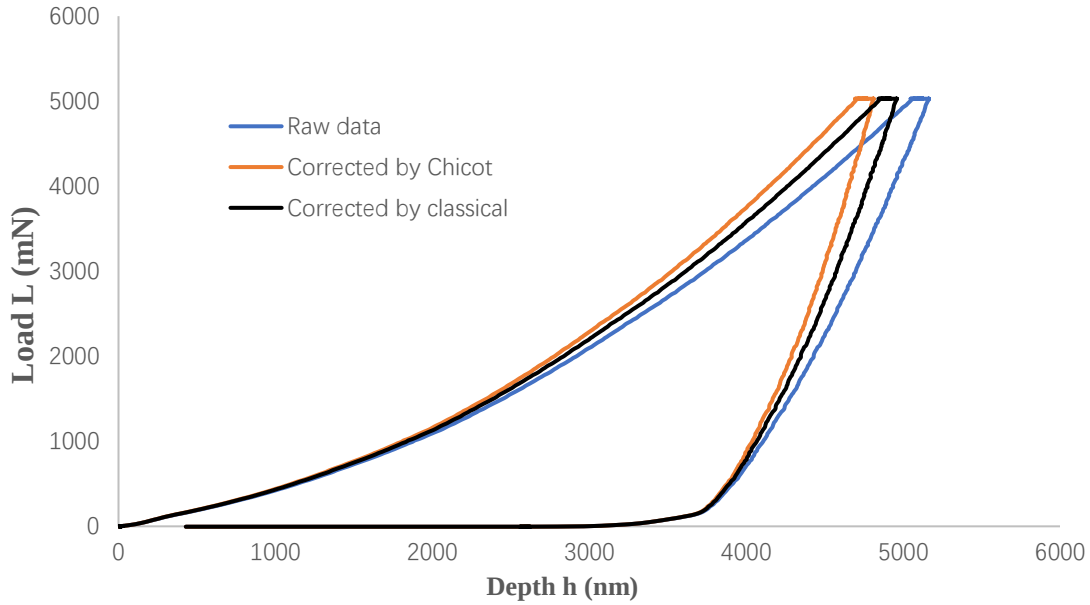

Figure II-12. *The difference among raw experimental curve and corrected curves by two models.*

In Figure II-12, it can be found that there is obviously difference before and after the correction by the compliance.

And once the compliance C_f is determined, the indentation depth h_{cor} and the slope of the load-depth curve S_c can be corrected as well:

$$h_{i.cor} = h_i - C_f \cdot P_i \tag{II-9}$$

$$\frac{1}{S_{cor}} = \frac{1}{S} - C_f \tag{II-10}$$

From the corrected curve and result, the reduced modulus E_r can be calculated [89]:

$$E_r = \frac{\sqrt{\pi} S_{cor}}{2\sqrt{A_P(h_{c.cor})}} \tag{II-11}$$

According to the standard *ISO14577* [10], the instrumented indentation modulus E_{IT} can be calculated as:

$$E_r = \frac{(1-v_s^2)}{E_{IT}} + \frac{(1-v_i^2)}{E_i} \tag{II-12}$$

This equation can be also expressed as:

$$E_{IT} = (1 - v_s^2)(\frac{1}{E_r} - \frac{(1-v_i^2)}{E_i})^{-1} \quad \text{(II-13)}$$

Where v_s is the Poisson's ratio of the material here is 0.21 [90], v_i and E_i is the Poisson's ratio and the elastic modulus of the indenter respectively. In our work, the indenter is made by diamond whose Poisson's ratio is 0.07 and elastic modulus is 1140 GPa.

The contact depth h_c from the experiment can get correct by the compliance as well:

$$h_{c.cor} = h_{max.cor} - 0.75\frac{F_{max}}{S_{cor}} \quad \text{(II-14)}$$

Where $h_{c,cor}$ means the corrected contact depth while $h_{max.cor}$ is the maximum depth during the test which is already corrected.

So the instrumented hardness and Martens hardness could be Eq. II-15 and Eq. II-16 respectively:

$$H_{IT} = \frac{F_{max}}{24.5 \times h_{c.cor}^2} \quad \text{(II-15)}$$

$$H_M = \frac{F_{max}}{26.43 \times h_{max.cor}^2} \quad \text{(II-16)}$$

All the result are given in the Table II-8 with different maximum load. In Figure II-13 and II-14, the hardness and elastic modulus still have a slope after the correction with tip defect. The dash lines are the average value calculated from Table II-8.

Table II-8. *The result of hardness and elastic modulus of Cr-VI from instrumented indentation.*

Maximum Load (mN)	E_r (GPa)	E_{IT} (GPa)	H_{IT} (GPa)	H_M (GPa)
5000	245.39	297.17	9.82	7.14
2900	253.50	309.78	10.84	7.75
1960	249.91	304.17	11.22	7.92
980	246.26	298.51	11.01	7.88
490	270.32	336.68	12.45	8.71

245	246.40	298.73	11.60	7.99
Standard deviation (over **10 tests)**	9	15	0.9	0.5
Average value	**252**	**308**	**11.2**	**7.9**

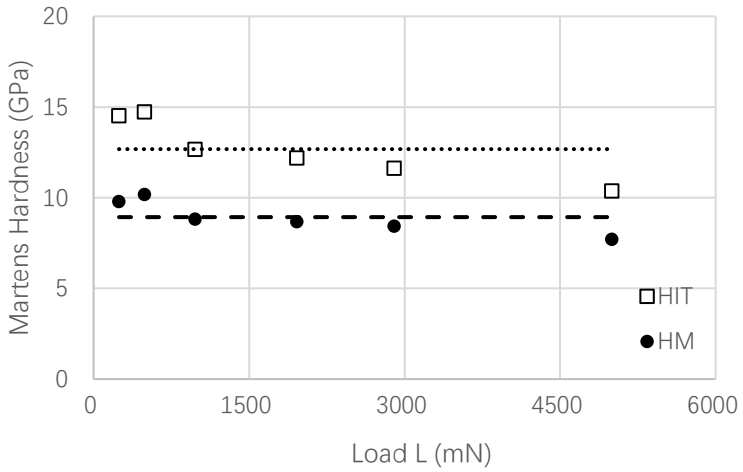

Figure II-13. *Instrumented hardness and Martens hardness of Cr-VI coating. The dash lines are the average value of H_{IT} and H_M.*

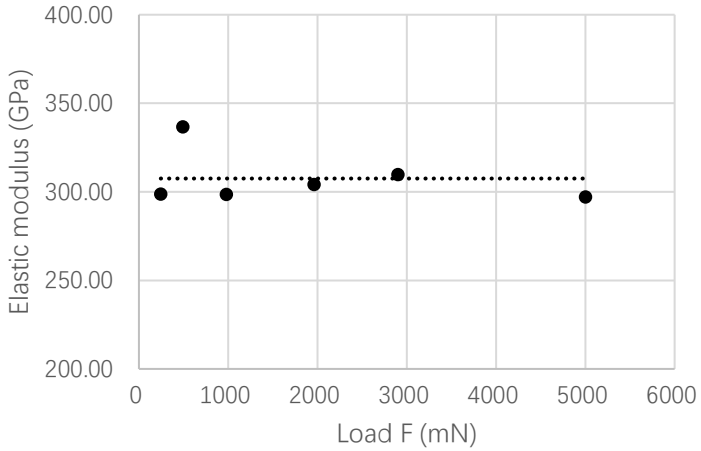

Figure II-14. *Elastic modulus E_{IT} of the Cr-VI coating. The dash line is the average value.*

From the final result, the instrumented hardness $H_{IT} = 11.2 \pm 0.9$ GPa, while the Martens hardness $H_M = 7.9 \pm 0.5$ GPa. The instrumented elastic modulus is also determined, $E_{IT} = 308 \pm$

15 GPa.

It is mentioned in previous section that the Vickers hardness is calculated by Eq. I-5 in chapter I. And the Martens hardness is calculated by Eq. II-16. It is interesting to noting that, with Vickers indenter, the maximum indentation depth $\boldsymbol{h_{max}}$ and the indent diagonal $\boldsymbol{d}$ can be converted by:

$$h_{max} = \frac{d}{7} \tag{II-17}$$

Thus, at maximum load, $\boldsymbol{d}$ could be replaced by $7\boldsymbol{h_{max}}$ and we could get:

$$HV = \frac{1.8544F}{(7h)^2} = \frac{F}{26.43h_{max}^2} = H_M \tag{II-18}$$

Eq. (II-18) shows the Martens hardness is comparable with Vickers hardness, which gave out by the classical indentation test, in mathematic. In previous section, the Vickers hardness of Cr-VI is 8.03 GPa and 8.53 GPa on the top surface and cross section surface respectively.

2.3 Conclusions

Indentation test is a very common and fast way to get the mechanical properties like hardness for our materials. The first choice would have been nano indentation. But unfortunately, due to the roughness of the coated samples, it is very hard to get accurate information from such surfaces. The work goes to the classical and micro scale indentation test.

From the result of the classical and micro indentation test, we find a phenomenon that hardness tends to increase as the indent size decreases at small scales, which is well-known as indentation size effect. In order to get rid of this effect, several models are applied and compared, and finally it turns out that on the top surface of Cr-VI, the hardness is around 8 GPa, while on the cross-section is around 8.5 GPa.

For Cr-VI coating, when indenting on the top surface, we only consider the first three data points to ensure that the indenter displacement will not exceed 10% of the coating thickness [31]. These data points are under very low load and far from the substrate. When indenting on the cross-section, there is no necessary to consider the influence from the substrate under the coating. But for NiW-2A and

NiW-5A coating, it is important to take into account the effect of the substrate.

The model of Jönsson and Hogmark is applied for NiW-2A and NiW-5A to remove the substrate effect. In this work, the constant C in Jönsson and Hogmark model is discussed. The constant C is fixed to 0.5 and 1 depending on the mechanical behavior of the material which is *a priori* not known, *i.e.* brittle and ductile respectively. We take C as a free parameter and try to find the best constant for NiW coatings. It turns out very close to the value 1. Finally, it is found out that the hardness of the NiW-2A coating is 4.4 GPa, while it is 5 GPa for NiW-5A.

For a further study, the instrumented indentation test is also applied for the Cr-VI coating on the cross-section. This can help us to get more information like elastic modulus and make the comparison between classical test and instrumented test. The compliance of the instrument has been fully discussed in previous section. And after comparing several models, the method proposed by Chicot *et al*. [86] is applied for our samples. The tip defect is also considered when correcting the value of hardness. Finally, the instrumented hardness is $H_{IT} = 11.2 \pm 0.9$ GPa, the Martens hardness is $H_M = 7.9 \pm 0.5$ GPa, and the instrumented elastic modulus is $E_{IT} = 308 \pm 15$ GPa.

Chapter III. Structures and cracks formation

In this chapter, the aim is to explore the information about the material's structure and surface morphology. X-ray diffraction can reveal the residual stress in the as-coated or heat-treated material. The specimens for X-ray diffraction test (XRD), tensile test and scratch test use the same ST37 steel substrate as before. For the cracks formation are investigated by indentation, scratch and tensile tests to evaluate the adhesion and toughness. These experiments are the main methods used to characterize the samples in this work.

3.1 XRD characterization

3.1.1 Specimen preparation and device

Room temperature XRD experiments are realized by the MiniFlex 600 (Japan) (Figure III-1(a)), equipped with θ-2θ set-up, using Cu wavelength radiation (λ=1.5406 Å). These experiments were performed on as-coated and heat-treated specimens. The Cr-VI here is used as a reference in the test. Firstly, there are three groups of NiW coatings with varying W content, and then they are heat-treated. After that, there are NiW-2A and NiW-5A, which is also mentioned in chapter II with approximately same W content but different deposition parameters. For different groups of NiW coating, they are listed in Table III-1 and the electroplating conditions are the same as before. More details can be found in Appendix I.

Table III-1. *The information of three groups of NiW in XRD test.*

Groups	Tungsten percentage W/(W+Ni)	Electroplating current
NiW C+	16.3 at%	5A/dm^2
NiW G	2.7 at%	8A/dm^2
NiW C-	9.6 at%	10A/dm^2

The heat treatment tests were applied for the samples in order to observe the stress releasing with different temperatures. And then, these samples can be compared with the original specimens to know the residual stress [41][43]. Further experiments of in-situ XRD were realized by X'pert HTK 1200 (England) (Figure III-1(b)) which means the temperature can be controlled during the X-ray diffraction test, and more details will be given later for the choice of the temperatures. Several advantages of the XRD *in-situ* under temperature can be highlighted: (i) there is no cooling down, thus avoiding any evolution of the material after heat treatment; (ii) the evolution of residual stress and microstructure are continuously monitored with temperature and not only at a few steps; (iii) the same sample is studied at different temperatures, no questions could come from natural discrepancy or heterogeneity of the material.

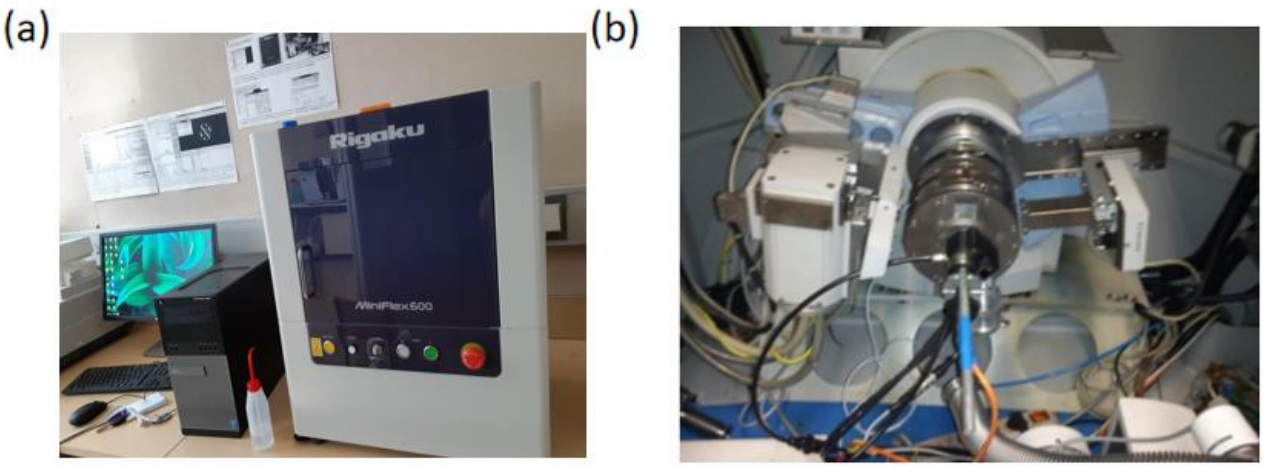

Figure III-1. *(a) The XRD test device MiniFlex 600 (Japan), and (b) The in-situ XRD device X'pert HTK 1200 (England).*

The coatings, including Cr-VI, NiW-2A, NiW-5A are around 10 to 12 µm thick and the specimens are about 2 cm x 3cm.

Before the *in-situ* XRD test, the specimens need to be cut into small pieces around 1cm x 1cm and it is necessary to measure the parallelism of the specimens in order to ensure the specimens are flat enough for the test. It is easy to understand that if the value of parallelism is too important the

measurement of the angle 2θ will be false, and then the discussion on the variations of the peaks. The parallelism tests are carried out for specimen NiW-2A and NiW-5A by the Coordinate Measuring Machines (CMM) UPMC-carat.

Figure III-2 shows how to measure the parallelism, and the radius of the red sphere used to detect is 2mm (Figure III-2a). In Figure III-2 (b) presents an example about the during the test: the measurement of parallelism was defined in a square around 1mmx1mm, each point is a test point for the device, but the lines are just a graphical representation of the surface and not the path of the probe.

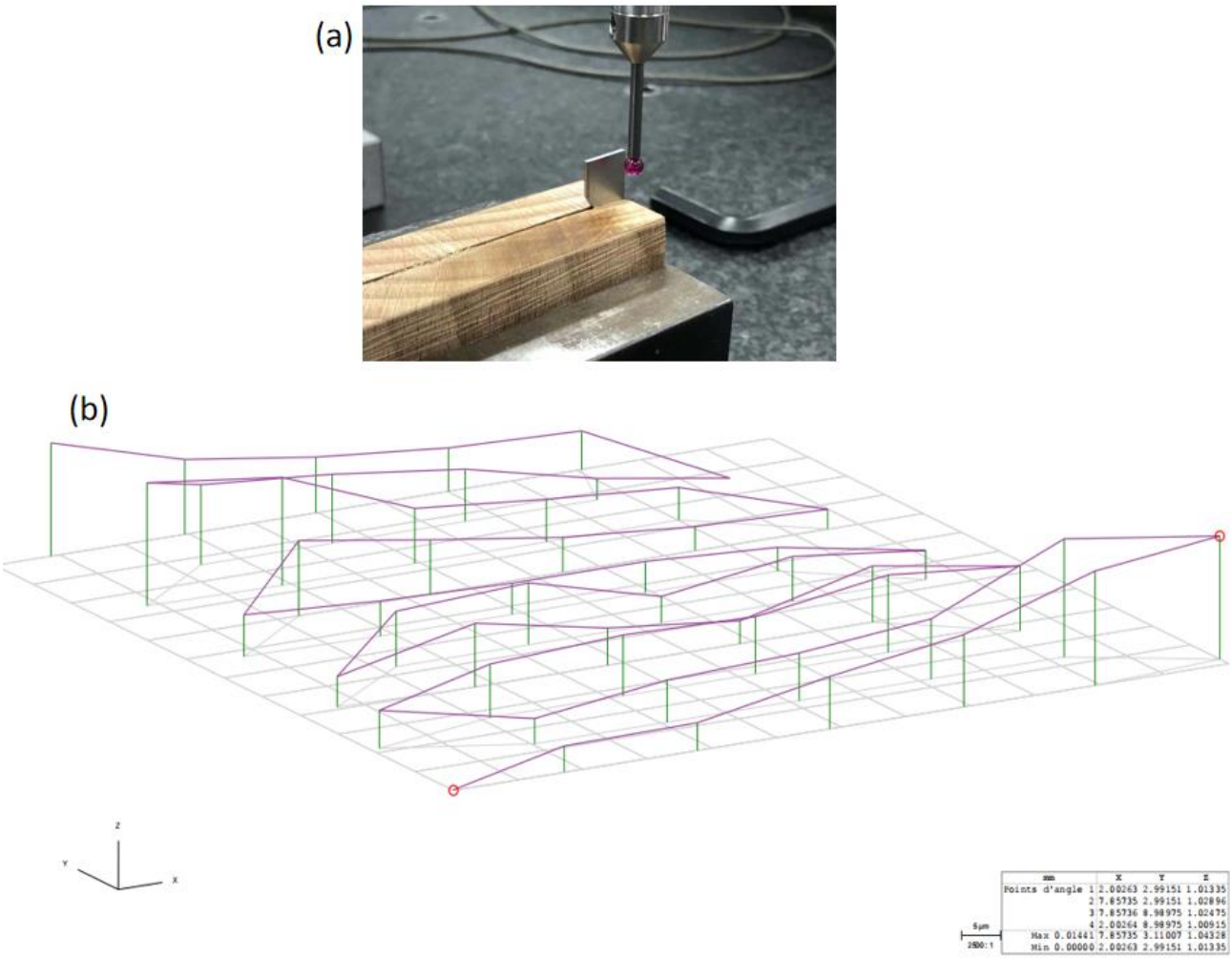

Figure III-2. *(a)The reference shape and surface (front surface is reference) and (b) the measurement of the parallelism.*

The parallelism is defined like the maximum distance, between the points and the reference plane, minus the minimum distance. We selected two definitions for the reference plane. Gauss analysis uses the least squares method, whereas PlanExterne is a tangential plane defined by the outermost points.

Table III-2. *The parallelism of two NiW specimens regarding the two definitions.*

Samples	Gauss	PlanExterne
NiW-2A	21 μm	28 μm
NiW-5A	42 μm	63 μm

For both definitions (shown in Table III-2), the parallelism of the coatings is small enough (smaller than 100 μm) to carry out the in-situ XRD test.

3.1.2 Results and discussion

The first part of the X-ray diffraction test is done by the MiniFlex 600 and the specimens are Cr-VI and NiW coatings.

For Cr-VI coating, the highest temperature was selected as 600 ℃ in order to observe the modification of the inner stress and structure but, to follow their evolutions, two steps are added between room and maximal temperatures. So the final temperatures were set as 200 ℃, 400 ℃ and 600 ℃.

Firstly, the XRD test was applied to the Cr-VI coatings. Figure III-3 shows the result: the maximum height of peak diffraction increases with temperature; this can be linked to the internal stress reduction. Besides, with the temperature from room temperature to 200 ℃, the increase of the height and the decrease of the width is not significant. But when the temperature reaches 400 ℃ and 600 ℃, the peaks' height increases a lot which means more stress are released by the heat treatment. On the other hand, in the standard graph of Cr (Figure III-4), the highest peak ($2\theta = 44.5°$) shall be the one which corresponds to the {110} diffraction family plane. The experimental graphs do not exactly correspond to the standard one, in terms of peak diffraction angles, we predict that there is a very strong preferred

orientation in the samples because as it can be noted on Figure III-3 the main peak, for the several level of temperature, focus at $2\theta = 81.6°$, which is not the same peak as the standard. For the stress releasing, it could be caused by the removing of the dislocations or the recrystallization as mentioned in chapter I. But from the result, the preferred orientation never changes with the increasing of temperature. So even there is recrystallization, the grains always keep the same orientation.

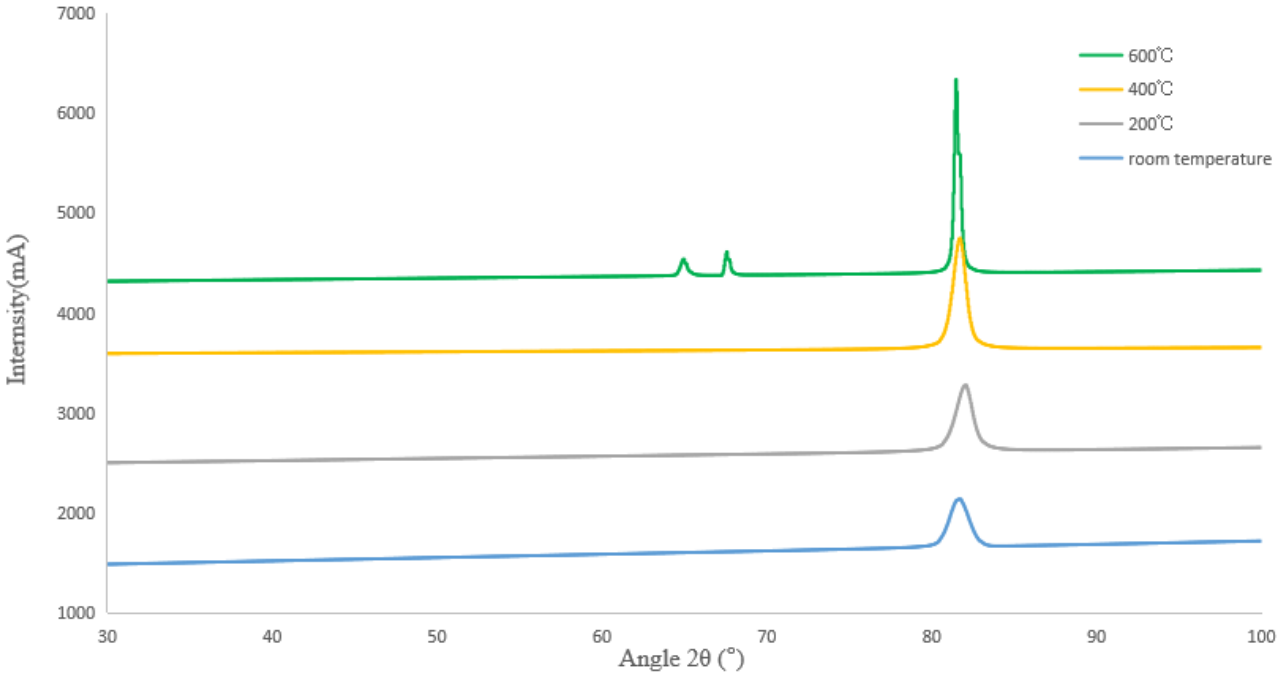

Figure III-3. *The XRD result of Cr-VI after different temperature heat treatment.*

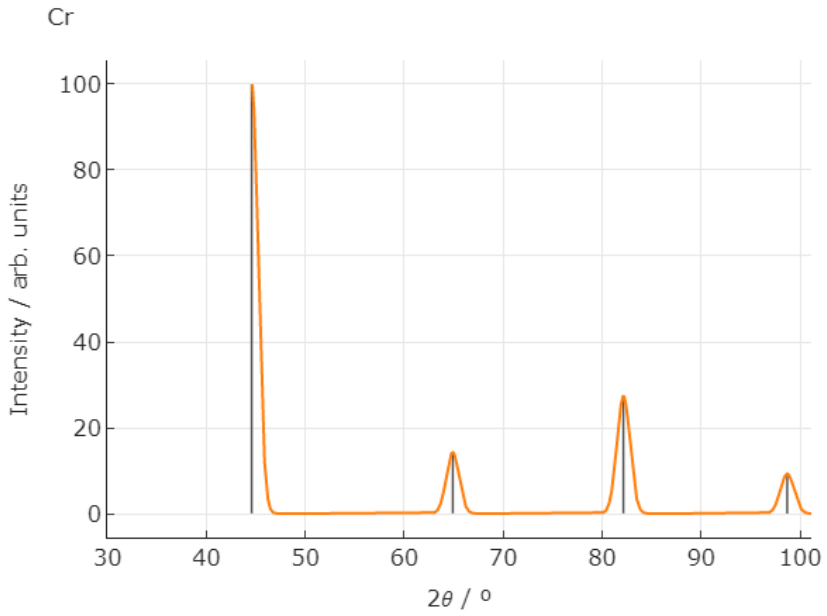

Figure III-4. *The standard peaks of Cr (From the data base: The materials project* [91]*).*

Besides Cr-VI specimens, the three groups of NiW are also investigated by XRD. For NiW coatings, there are three different groups of samples: C+, G and C-.

For the NiW coatings, the choice of the temperatures of heat treatments were based on the exploration of the phase diagram of Ni-W. In this series of experiments, the atom percentage of W varies between 2.7 and 16.3 at%. As we can see on the Figure III-5, the elevation of temperature induces modifications in the microstructure, only in the 16.3 at% specimen.

The 2 others (2.7 at% and 9.6 at%) remain under the form of FCC_A1 phase;

For the specimen with 16.3 at%:

- between room temperature to around 400 K (127 °C) the phases are FCC_A1+NiW(S);

- between 400 K and some 1200 K (between 100°C and 900°C) there is a mixture of FCC_A1+Ni_4W(s);

- above 1200 K (900°C), there is only FCC_A1 phase;

- for temperature higher than 1800 K (1527 °C), the material melts.

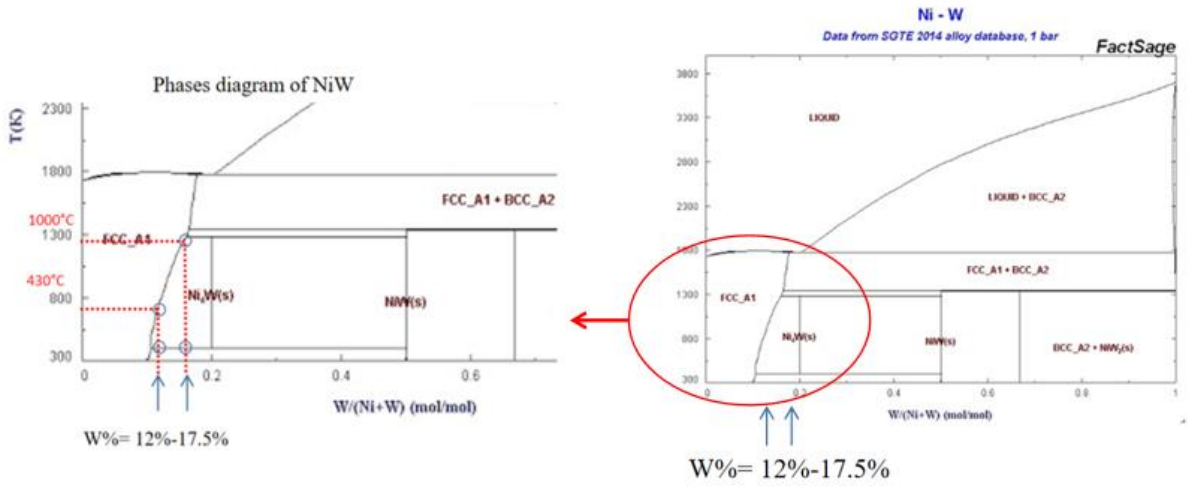

Figure III-5: *The phases diagram of Ni-W system (From the database FactSage* [92]*).*

For group G and C-, the phases are always FCC_A1 when the temperature is under 1000°C. But for NiW samples which have a composition between 12 and 17.5at% in tungsten atom percentage (that means NiW-2A, NiW-5A and group C+), when temperature is increased, phase transformations are occurring for 300°C and between 500 and 900°C. Finally, we choose the three limit temperatures (300, 500 and 900°C) plus an arbitrary intermediate temperature in the last interval (700°C). All the NiW groups have experienced heat treatment test with several different temperatures and last for 1h.

The Figure III-6 shows the results of NiW diffraction. The bottom curves in the three graphs are obtained at room temperature. And the following curves are at 300 ℃, 500 ℃, 700 ℃ and 900 ℃ respectively.

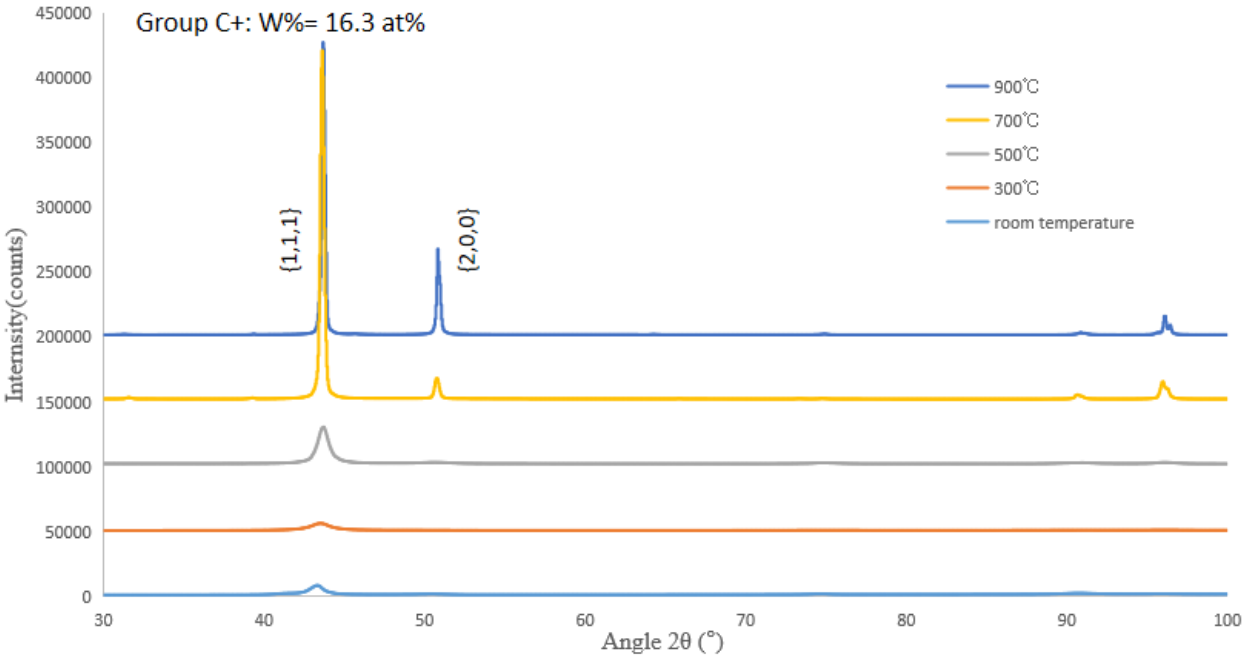
Group C+: W%= 16.3 at%
900°C
700°C
500°C
300°C
room temperature
{1,1,1}
{2,0,0}
Intensity(counts)
Angle 2θ (°)

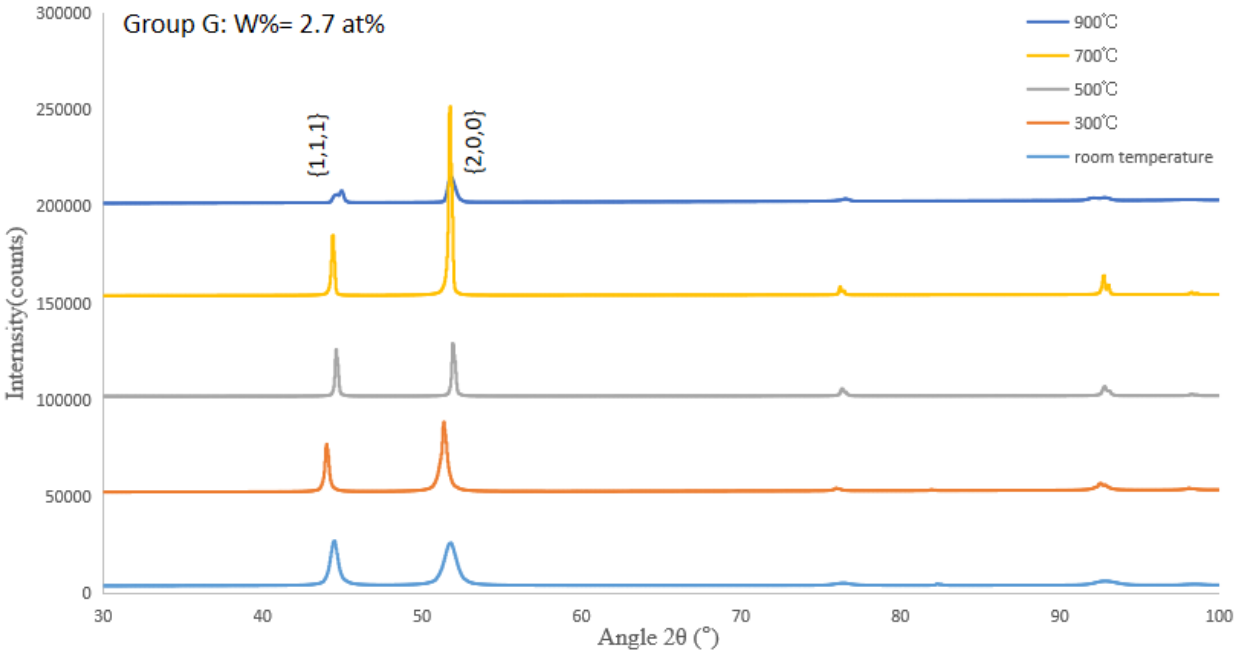
Group G: W%= 2.7 at%
900°C
700°C
500°C
300°C
room temperature
{1,1,1}
{2,0,0}
Intensity(counts)
Angle 2θ (°)

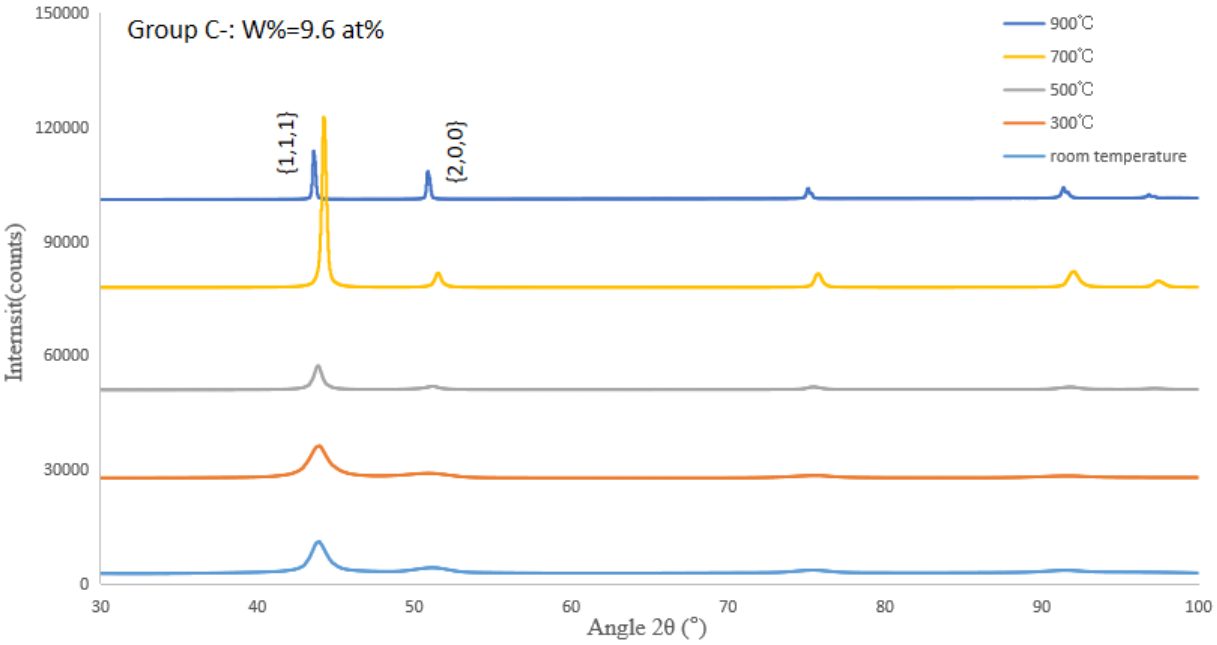

Figure III-6. *Three groups of NiW coating (C+, G and C-) XRD results.*

From the Figure III-6, it can be seen that the heat treatment can help to release the stress inside the coatings as the same situation as Cr-VI coating. All the Figures III-6 show that there are only peaks of FCC-A1 phase. Additionally, at room temperature or in a relatively low temperature of heat treatment, the intensities of peaks are very low, for instance for FCC-A1 at room temperature of group C-. Additionally, the group G has a stronger preferred orientation on the peak {220} than the other two groups. As the same as Cr-VI coating, the heat treatment enables to increase the crystallite size, and here the starting temperature of stress releasing is around 500 ℃ for all groups of NiW coatings.

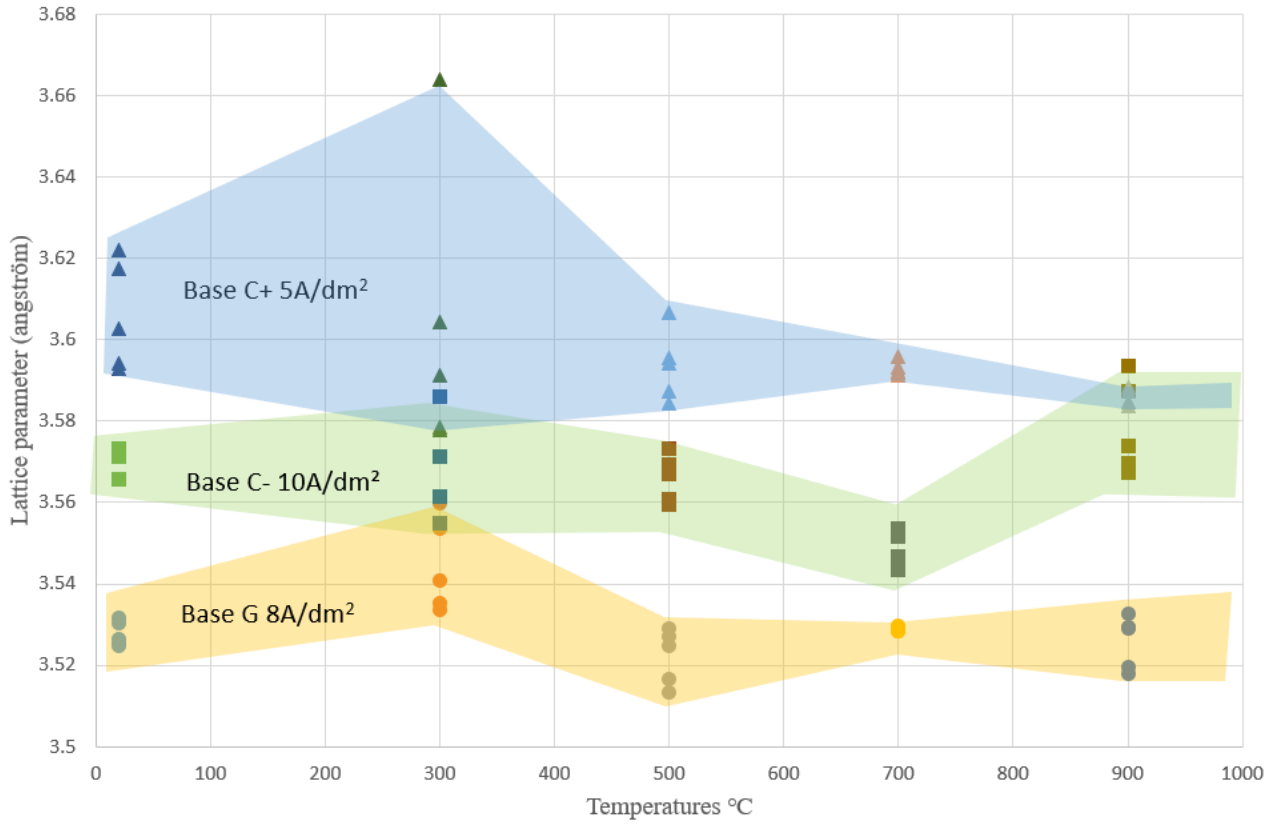

Figure III-7. *Lattice parameters of NiW group C+, C- and G as a function of temperature.*

In Figure III-7, the different symbols present the lattice parameters computed by the experiments results. The shadow area with colors shows the possible value of lattice parameters in different temperatures, and we can conclude that: group C+ and G has the largest and smallest lattice parameters respectively. It is due to the decreasing concentration of tungsten which has much larger size than the nickel atom.

Till now, all the specimens have been heated to the given temperature and then cooled down to room temperature. In this condition, we wonder at which temperature the stress start to decrease and if there is anything happening during the heating, especially from 500 °C to 900 °C. In the *in-situ* XRD, one specimen can be tested for different temperatures of heating and cooling.

During *in-situ* XRD the temperature is fully controlled. The specimens are NiW-2A and NiW-5A. The heating profile on Figure III-8 is proposed: five temperature steps (300, 500, 700 and 900°C as previously selected) with a dwelling time of one hour each and a heating time of one hour between

each step, whatever the temperature increase. The dwelling time are here to see the modification of the structure with time. During the cooling, one step of 1h was realized at 500°C and 300°C with a cooling of one hour between each step.

Figure III-8. *The steps and corresponding temperatures of the in-situ XRD test.*

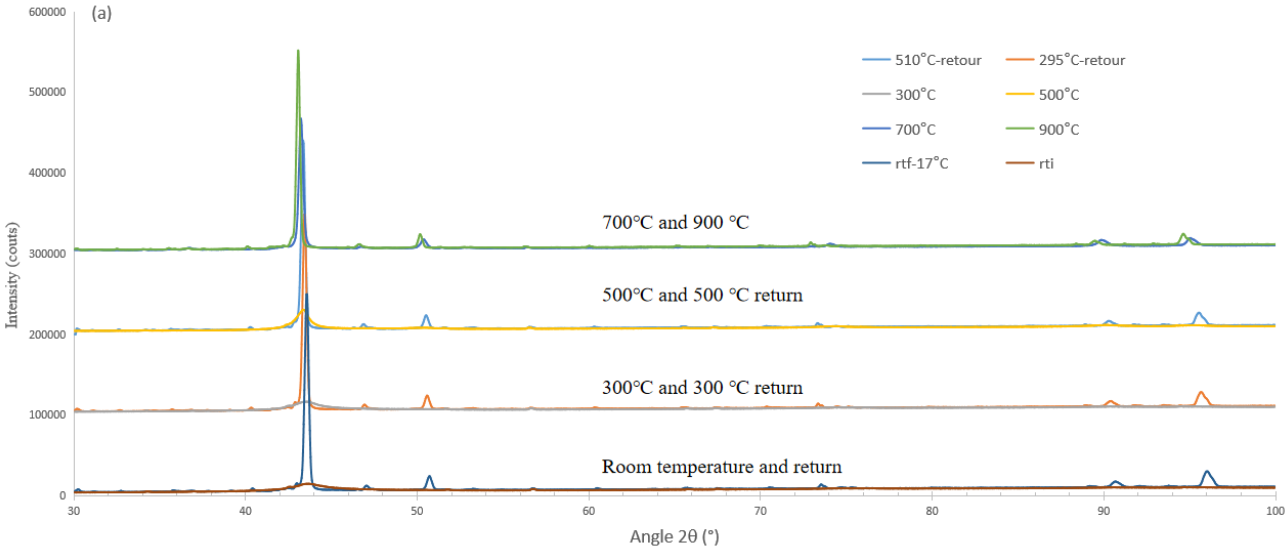

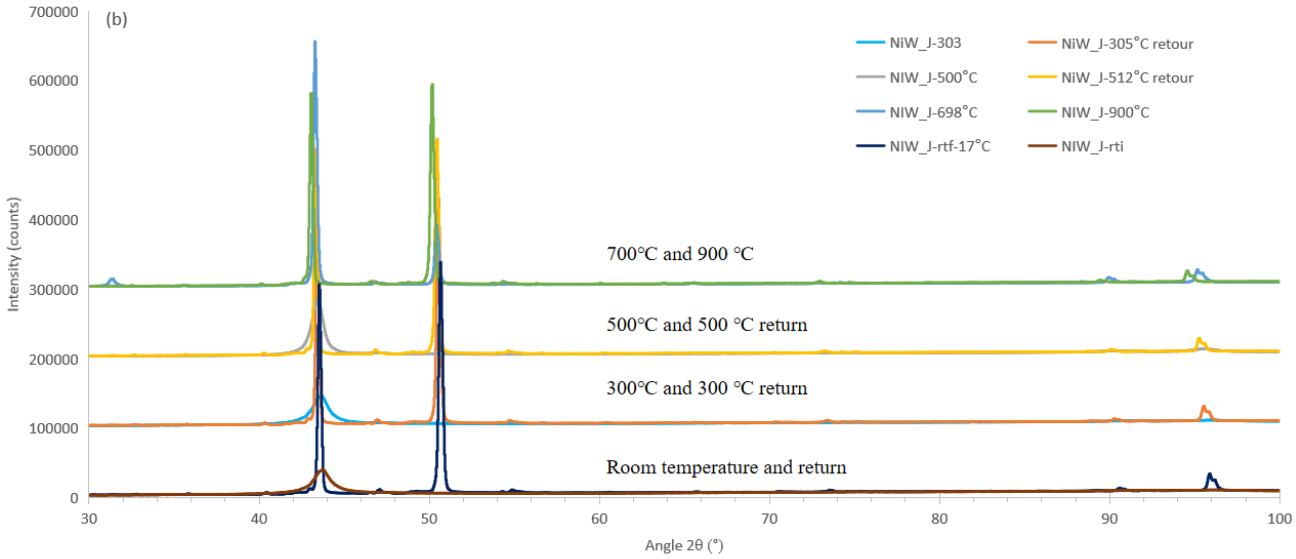

Figure III-9. *The in-situ XRD results of (a)NiW-2A and (b)NiW-5A with different temperature.*

The Figure III-9 gives out the *in-situ* XRD results of NiW-2A and NiW-5A. It can be seen that the preferred orientation is quite different from NiW-2A to NiW-5A. There is no peak {220} for NiW-2A which means it has similar orientation with pure Ni. And there are small peaks that cannot be observed by previous tests. By comparing the standard peaks of Ni4W and Ni6W6C (Figure III-10), and also considering other authors observation [93], these peaks may belong to the Ni6W6C phase, and they can be seen here due to the higher power of the radiation in these tests than the former one. Besides, there seems not peaks corresponding to the Ni4W phase, they are possible to be masked by or merged to the FCC Ni peaks.

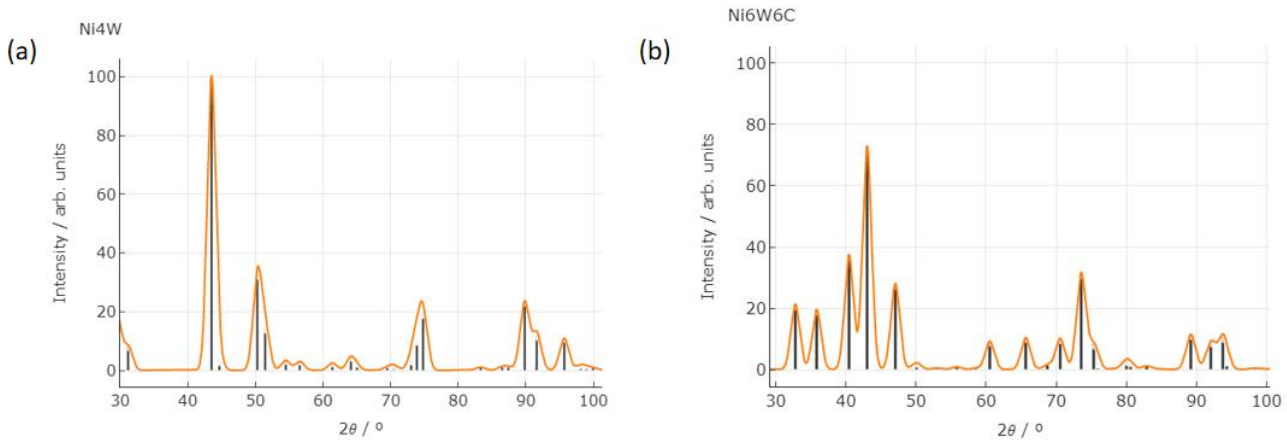

Figure III-10. *The standard peaks of (a) Ni4W and (b) Ni6W6C (From the data base: The materials project* [94]*).*

As mentioned in chapter I, full width at half maximum (FWHM) is a very common and convenient method to analyze peak broadening. This method is based on the Scherrer's equation [51]:

$$D = \frac{k\lambda}{\beta cos\theta} \tag{III-1}$$

Where $\boldsymbol{D}$ is the crystallite size, $\boldsymbol{\lambda}$ is the wavelength of the X-ray source, in this work it is a copper tube and selected wavelength is $\lambda = 1.5406$ Å. $\boldsymbol{\theta}$ is the diffraction angle and the $\boldsymbol{\beta}$ is FWHM which is expressed in radians, these two parameters can be determined by peak diffraction analysis. $\boldsymbol{k}$ is the Scherrer's constant, which depends on the crystal structure and varies from 0.62 to 2.08, and mostly it is used as 0.94 [52][53].

The variation of the crystallite size $\boldsymbol{D}$ can be plotted as the Figure III-11 shows. From Table III-3, the steps and the condition of temperature are mentioned.

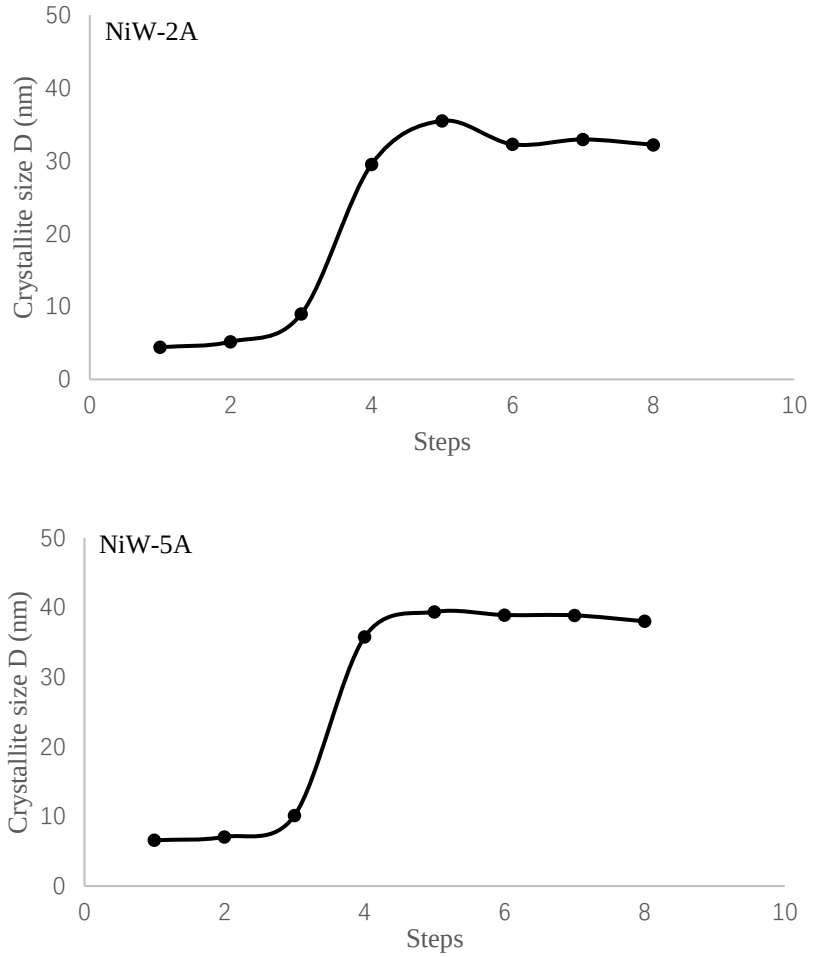

Figure III-11. *The Crystallite size of NiW-2A and NiW-5A with the temperature varies. (Steps are explained in Table III-3.)*

Combining the corresponding temperature and the crystallite size, the re-crystallization starts from around 500 ℃ and it is almost done when it comes to 700 ℃. After that, even after cooling at a lower temperature, the crystallite size remains the same. For NiW-2A, there is only one peak shown on the result, but for NiW-5A, the second peak appears after the temperature 500 ℃. Because these two NiW coatings has different current density during electroplating, the preferred orientation seems to be influenced by the current density of deposition for electroplated coatings. In Figure III-11, the curve only presents the first peak of both NiW material. When the temperature is higher than 700 ℃, the average crystallite size is 32.50 nm for NiW-2A, while for NiW-5A are 38.20 nm and 33.58 nm for the first peak and second peak respectively.

Table III-3. *The steps during in-situ XRD test.*

Steps	Conditions
1	Room temperature
2	300 ℃
3	500 ℃
4	700 ℃
5	900 ℃
6	500 ℃ cooling
7	700 ℃ cooling
8	Room temperature

In this work, we want to confirm the final result of crystallite size with the metallographic observation of the grain size (see Appendix II). But the experiments cannot give a good result due to the galvanic coupling.

3.2 Cracks analysis

3.2.1 Specimen and device

In the cracks analysis tests, four samples, Cr-VI, NiW-2A, NiW-5A and pure Ni coatings, are tested under tensile test (Instron, USA) and scratch test (TriboTechnic, France). The devices are presented in the Figure III-12 (a) and (b).

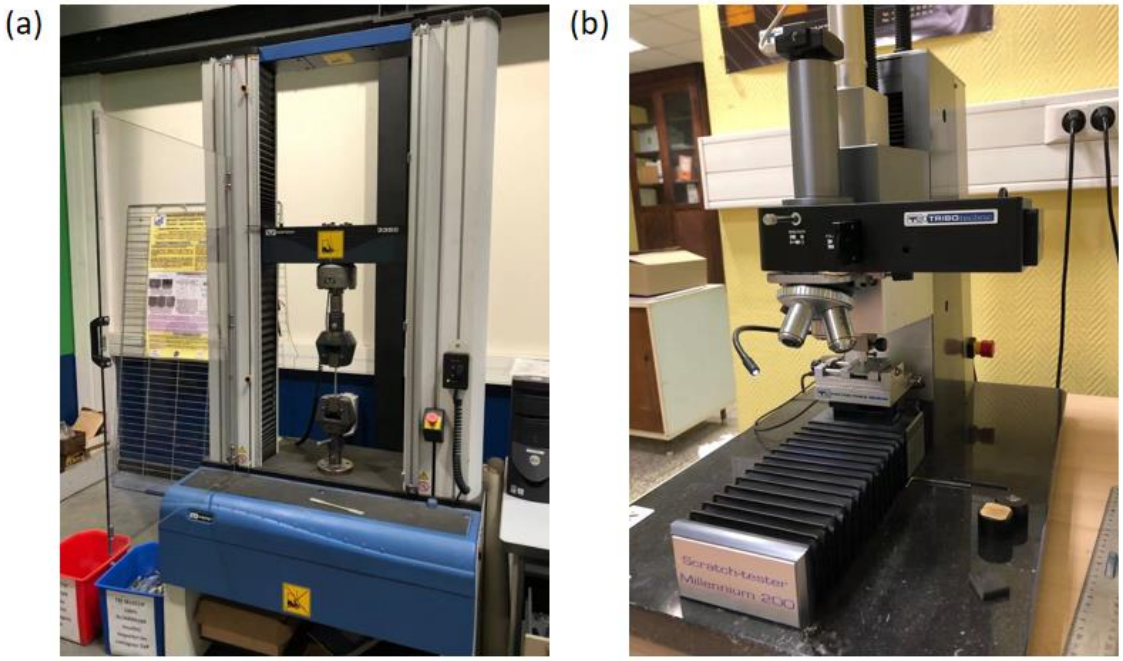

Figure III-12. *(a) Tensile test: Instron and (b) Scratch test: Millennium 200.*

As mentioned in previous sections, the samples for scratch tests need thin coatings in order to get reliable results. So the coatings, including Cr-VI, NiW-2A, NiW-5A and pure Ni, are around 10 to 12 μm thick. For scratch test, the size of specimens is around 2 cm X 3cm. And for tensile test, the specimens' shape and size are as shown in chapter I.

And for indentation crack length test, only the Cr-VI samples are experimented, whose thickness is around 100 μm which is also used in chapter II.

3.2.2 Results and discussion

As mentioned in chapter I, the indentation crack length test is designed to know the toughness and adhesion of the coatings. The main idea is to calculated the average crack length which origin from the imprint. In common, this method is applied when the cracks generated are almost straight lines. In order to make the comparisons among the coatings, the Cr-VI specimens are firstly applied to this method. Figure III-13 shows three indents at different loads: 200N, 300Nand 500N. The surface of the

coating with Cr-VI has a cauliflower structure. Resulting cracks are circular, almost centered on the indentation axis. Unfortunately, that network of cracks cannot be analyzed with aforementioned models, which described straight cracks.

To analyze the evolution of the crack, we propose to divide the indented surface into 8 sections, where the primary axes correspond at the end of the square of the imprint. Each section corresponding to 45° and plot a circle to contain all the residual imprint area after the indentation as red lines as shown in Figure III-13 (b). In this way, the number of cracks in every section could be counted. For the different loads, the cracks numbers are slightly different. But the number of cracks in all sections are similar. This can give us the information that the Cr-VI coating is isotropic. Besides the cracks number, the radius of circumscribed circle for the imprints and the outermost circular cracks are measured (Figure III-13 (c)), with details are listed in Table III-4. From Table III-4, the percentage of outermost cracks/imprint is decreasing with the load from 177% at 200 N to 116% at 500N. The decrease of this percentage can be explained by the fact that there is a higher influence of the substrate for the higher load, and it can be possible that the secondary cracks cannot join together to create a primary crack. More images of other loads can be found in Appendix III.

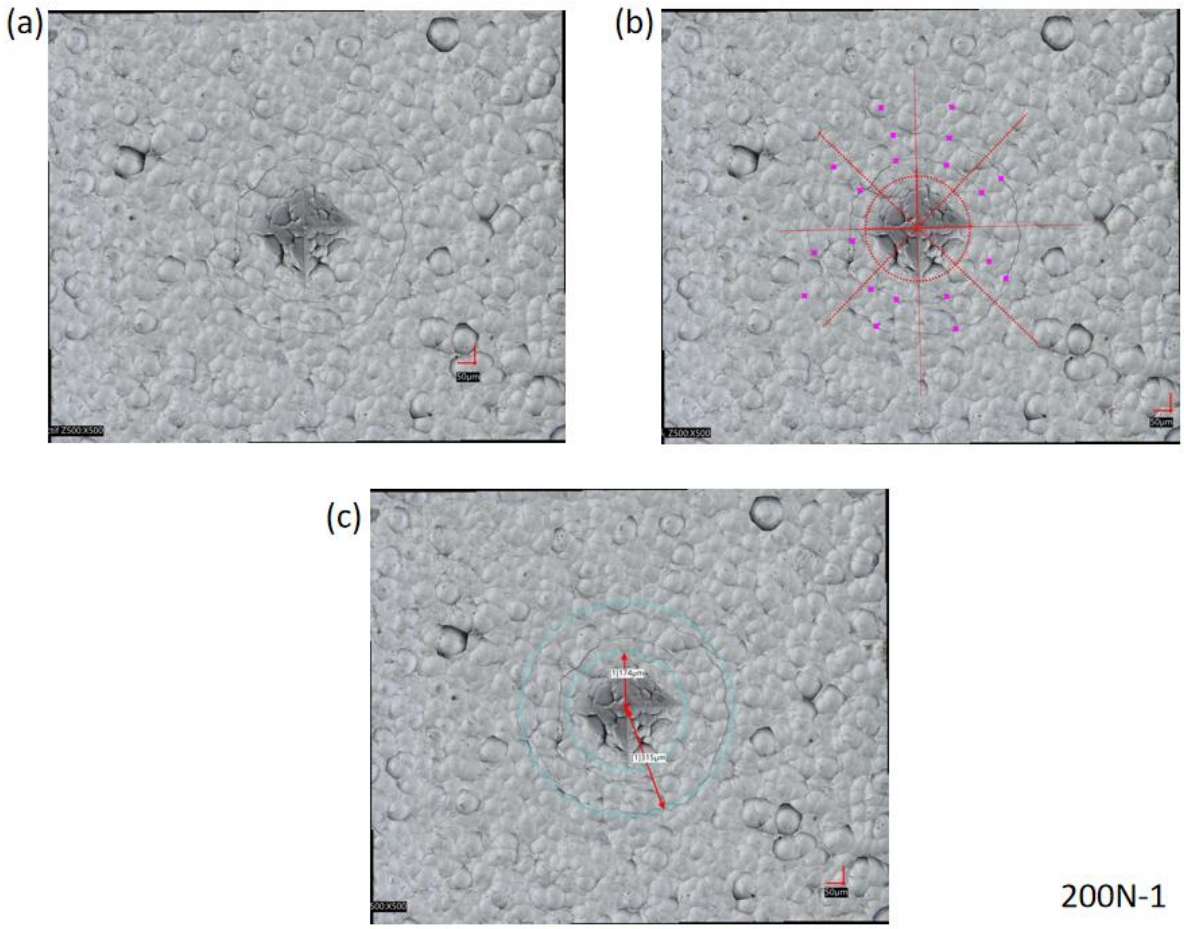

Figure III-13. *Schematics for one of the 200N imprints of (a) the bare cracks, (b) the determination of isotropic and (c) the measurements of the imprint and outermost crack radius.*

Table III-4. *Radius of the imprints and the outermost cracks for every load.*

Loads	**200N**				**300N**				**500N**	
Number of the test	1	2	3	4	1	2	3	4	1	2
Imprints radius µm	174	178	193	183	282	266	237	277	402	391
Average	182				265.5				396.5	
Outermost radius µm	315	328	316	331	402	389	394	386	467	450
Average	322.5				392.75				458.5	
Outermost/imprints	1.81	1.84	1.64	1.81	1.43	1.46	1.66	1.39	1.16	1.15
Average	1.77				1.49				1.16	

Since it is almost impossible to compare the length here in our test, and there is problem of subjective for the counting of cracks, this method is not really suitable for Cr-VI in this work. So we plan some further experiments of scratch test and tensile test to get some information of the surface from cracks.

The scratch tests are performed with a Rockwell C type tip with 200 μm radius and made by diamond. All the samples are scratched with a progressive load. Since all the coatings are around 10 μm thick, the maximum loads are set as 50 N while the initial loads start from 0 N. For every specimen, there will be three scratches in a proper interval to avoid interactions between tests, and every scratch will be 15 mm long. Loading speed is 50 N/min whereas the scratch speed is 15 mm/min, which means every test will take 1 minute. The scratches are shown as Figure III-14.

Figure III-14 shows an example of Cr-VI, NiW-2A, NiW-5A and pure Ni coatings respectively. In Figure III-14, the black curve is the friction force during the scratches, while the orange curve is the acoustic emission. From the result, the critical loads are at the positions around 3 mm away from the beginning of the scratch, since almost every coating shows a suddenly increase of the friction force in the graph. In addition, the acoustic emission curves give the information that there is something different at 9 mm. That is why there are two high magnification pictures which present the locations of 3 mm and 9 mm in Figure III-14. For the 3 mm position, it is almost the beginning of the scratches. There is nothing special observed even with a very high magnification. At the 9 mm, the acoustic emission decrease and then goes to stable. But same as 3 mm position, they are the same with the positions before and after this point. We have to be aware that there is almost no signal of acoustic emission from pure Ni specimen. This is due to the very good ductility of Ni. Though for Ni, the 9 mm position picture is still presented in Figure III-14 (d) to compare with others.

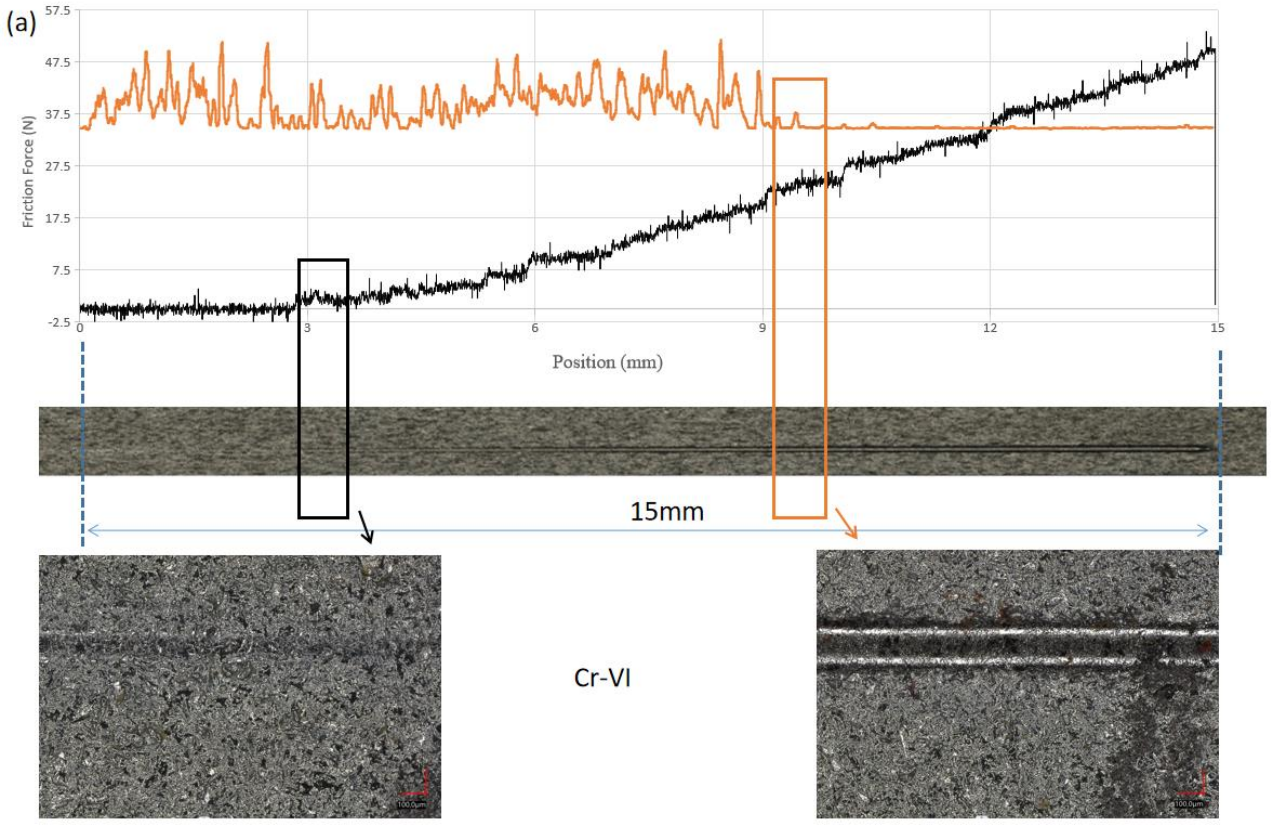
(a)
Friction Force (N)
57.5
47.5
37.5
27.5
17.5
7.5
-2.5
0
3
6
9
12
15
Position (mm)
15mm
Cr-VI

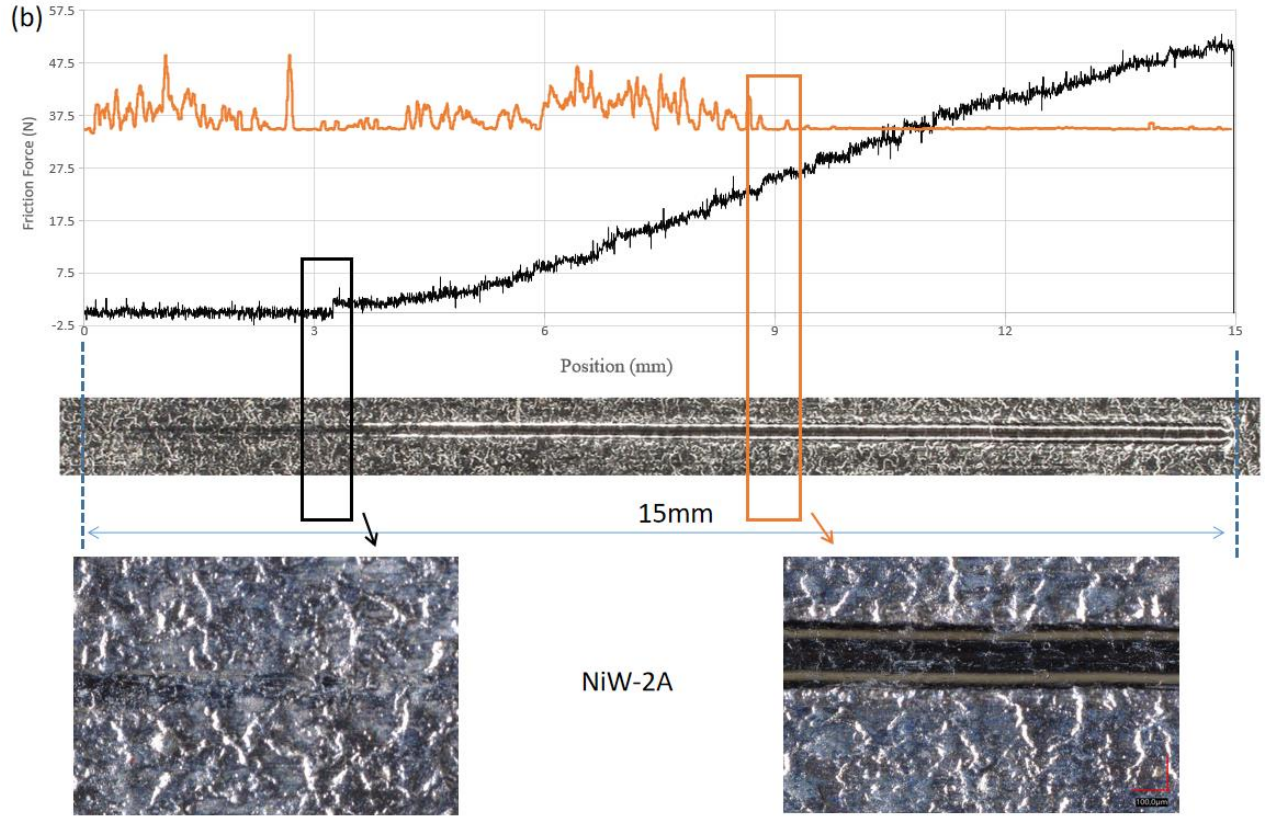
(b)
Friction Force (N)
57.5
47.5
37.5
27.5
17.5
7.5
-2.5
0
3
6
9
12
15
Position (mm)
15mm
NiW-2A

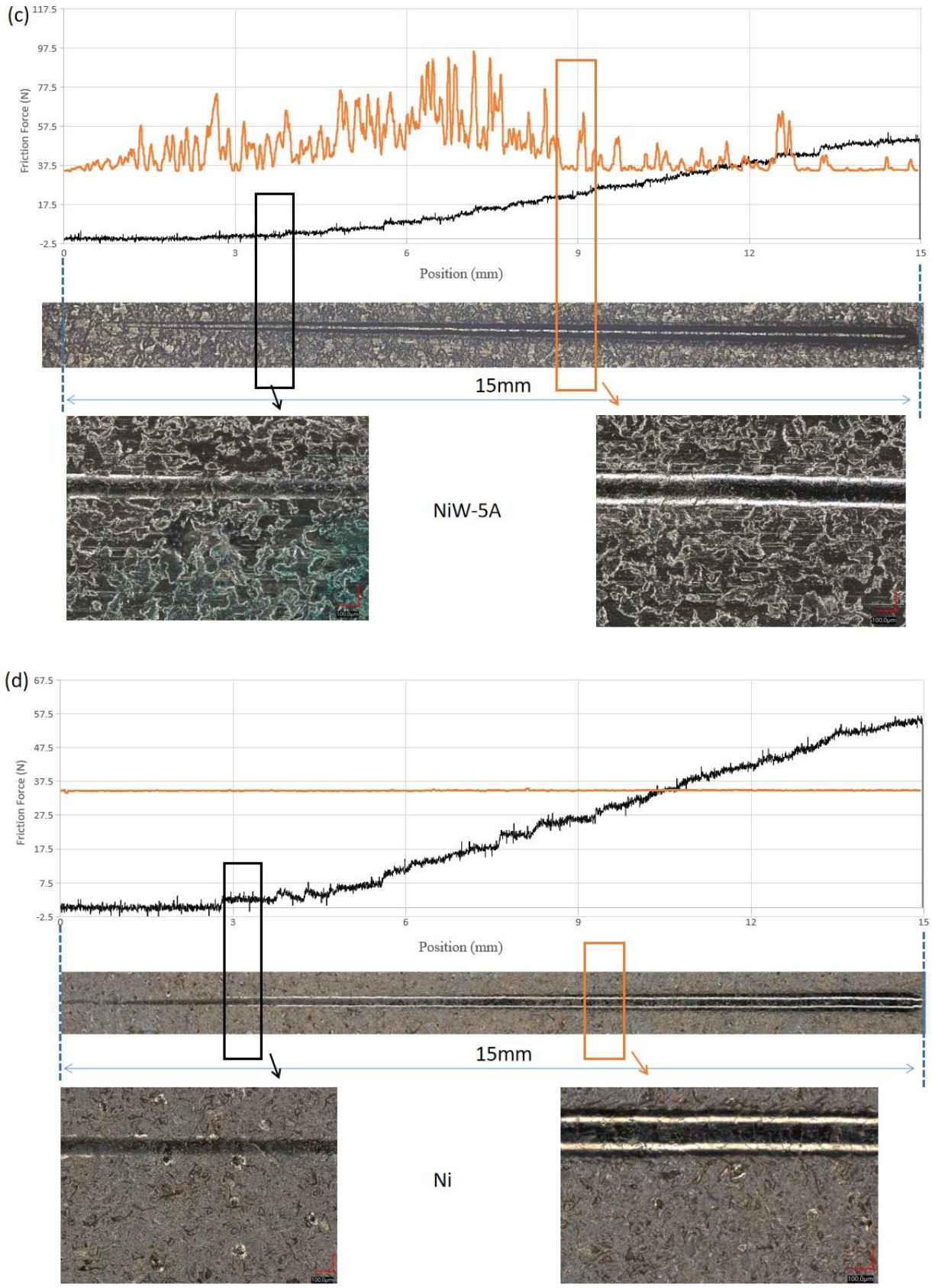

Figure III-14. *Scratches of (a) Cr-VI, (b) NiW-2A, (c) NiW-5A and (d) pure Ni coatings.*

From every test, the critical load is determined with checking the corresponding position on the surface with microscope on the Millennium 200 (Keyence, Japan). Because scratch test is a qualitative test, so compare the critical load is important. Every single test, there will be 2 or 3 critical loads and locations recorded and then the average will be calculated to be the final value.

For these possible critical loads from the scratch test, they are listed in Table III-5. And all the corresponding positions on the specimens' surface are checked. No difference before or after the critical positions on the scratched area can be observed with the microscope. Probably meaning that there are no "critical" changes in the mechanisms of deformation of the coating. For further investigations, we recommend to reduce the thickness of coatings in order to emphasis critical loads and material behavior changes.

Table III-5 *Critical loads of four different coatings.*

	Cr-VI	**NiW-2A**	**NiW-5A**	**Ni**
Critical load 1 (N)	1.29	1.88	1.76	2.84
	3.12	1.44	2.81	2.28
	5.46	2.48	1.86	2.28
Average	**3.29**	**1.93**	**2.14**	**2.47**
Critical load 2 (N)	5.88	2.13	2.27	4.37
	6.95	1.95	3.06	3.56
	5.46	2.33	2.88	3.06
Average	**6.10**	**2.14**	**2.74**	**3.66**
Critical load 3 (N)	5.46	2.39	3.54	2.84
	\	2.46	2.30	2.79
	\	3.25	3.14	3.82
Average	**5.46**	**2.70**	**2.99**	**3.15**

Since the indentation crack length method and scratch test cannot give out satisfied result, we

arrange to carry out the tensile test. In tensile test, as mentioned in chapter I, the trapezoidal shape for coated steel was applied.

The mechanical behavior of the ST37 steel substrate need to be fully characterized first. For this, tensile test samples have been prepared following standard ISO 6892-1 (Figure III-15). 3 samples have been prepared with cutting and no specific surface preparation, as it is used for deposition process. The tests have been performed at speed of 20 mm/min until the specimens are broken.

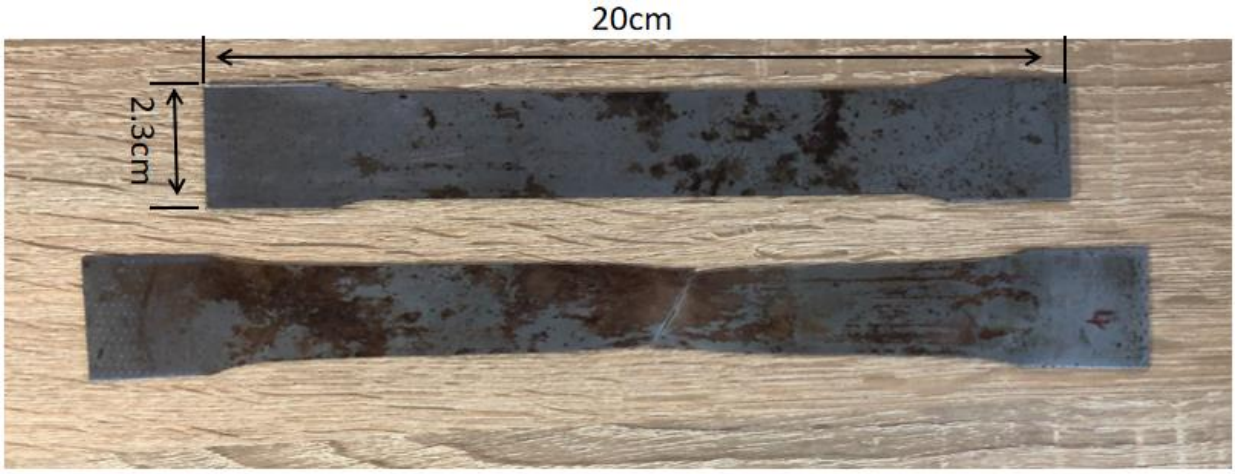

Figure III-15. *Substrate specimens before (top) and after (bottom) the tensile test.*

As mentioned previously, and according to the Hollomon's law, the samples which share the same substrate will have the same relationship between true stress and strain.

During the tensile tests, the initial length of extensometer which used to measure the displacement of our specimens is 5 cm. And all the prepared substrate samples are 2.5 cm width. The thickness of the substrate was measured equal to 0.8 mm for each sample.

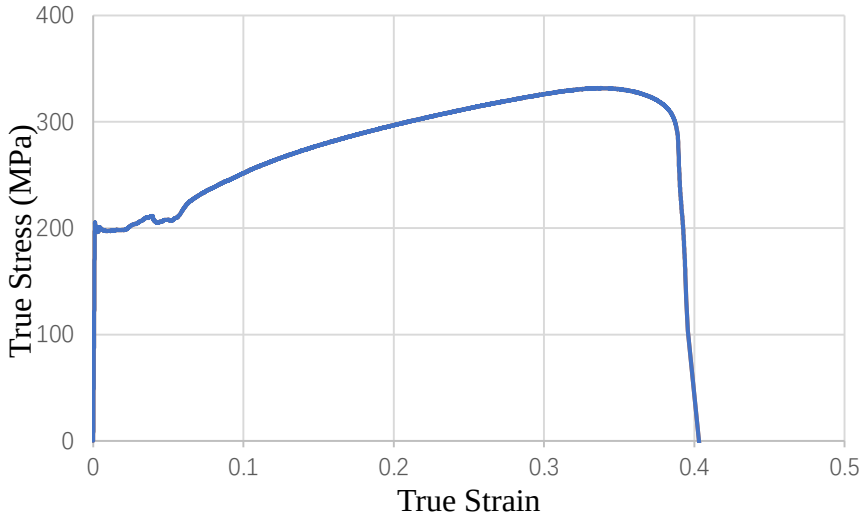

Figure III-16. *Typical tensile test for bare ST37.*

The tensile curve is shown as Figure III-16. From the previous analysis (in chapter I), the elastic modulus can be calculated as E= 184 GPa. Hollomon equation [65] can be applied after the elastic zone and before the necking, where the relation between the true stress $\boldsymbol{\sigma_t}$ and true strain $\boldsymbol{\varepsilon_t}$ is given by Eq. I-47:

$$\sigma_t = K\varepsilon_t^m$$

It can be written as:

$$ln\sigma_t = lnK + mln\varepsilon_t \quad \text{(III-2)}$$

So we can plot the linear relation between $ln\sigma_t$ and $ln\varepsilon_t$ to find out the constant $\boldsymbol{K}$ and exponent $\boldsymbol{m}$ for our substrate. In our work they are $K = 434.4$ MPa and $m = 0.2368$.

After it is clear for the substrate, the tensile tests are carried out at a constant displacement speed of 10mm/min for the coated samples. In this test, if critical stress and position are determined, the strain could be known by Hollomon relationship. So it is possible to know the strain and stress where the first crack generated (critical position) during the test in different coatings, and which coating has the highest toughness behavior is also known. The maximum displacements are set as 4 mm for NiW-2A and NiW-5A coatings, while they are set as 5 mm and 6 mm for Cr-VI and pure Ni coatings. Different

displacements have been selected in order to observe cracks on the surface sample and to avoid the final rupture of the specimen.

When the experiments finish, the specimens is scanned by the optical confocal microscope (Keyence, Japan). With the microscope, we can get where is the position when specimen starts to generate cracks and the corresponding width. Since both the thickness of the coating and the sections are known for all samples, the true stress and the true strain when the cracks appear are known. And also, by comparing the cracking stress, which material has the best adhesion situation will be clear among the four different coatings. The images of result shown as from Figures III-17 to III-20.

For the different coatings, the location and width of the cracks starting point are different, that means the adhesion of the coating is different on the substrate, but at the broadest end there is no crack for all the samples. As it can show in Figure III-17, Cr-VI coating has some very slight cracks before the test, while the cracks grow much larger, and some oriented new cracks are generated during the test. Both NiW coatings has some flakes, which represents the decohesion, at the thinnest position of the sample, they can be clearly seen in the Figure III-18 (b) and III-19 (b). The pure Ni coating (Figure III-20) shows no cracks even though the displacement is already large enough to break the specimen. And except the pure Ni coating, Cr-VI and both NiW coatings show the cracks network as expected: there is highest density of cracks at the thinnest part of the specimens.

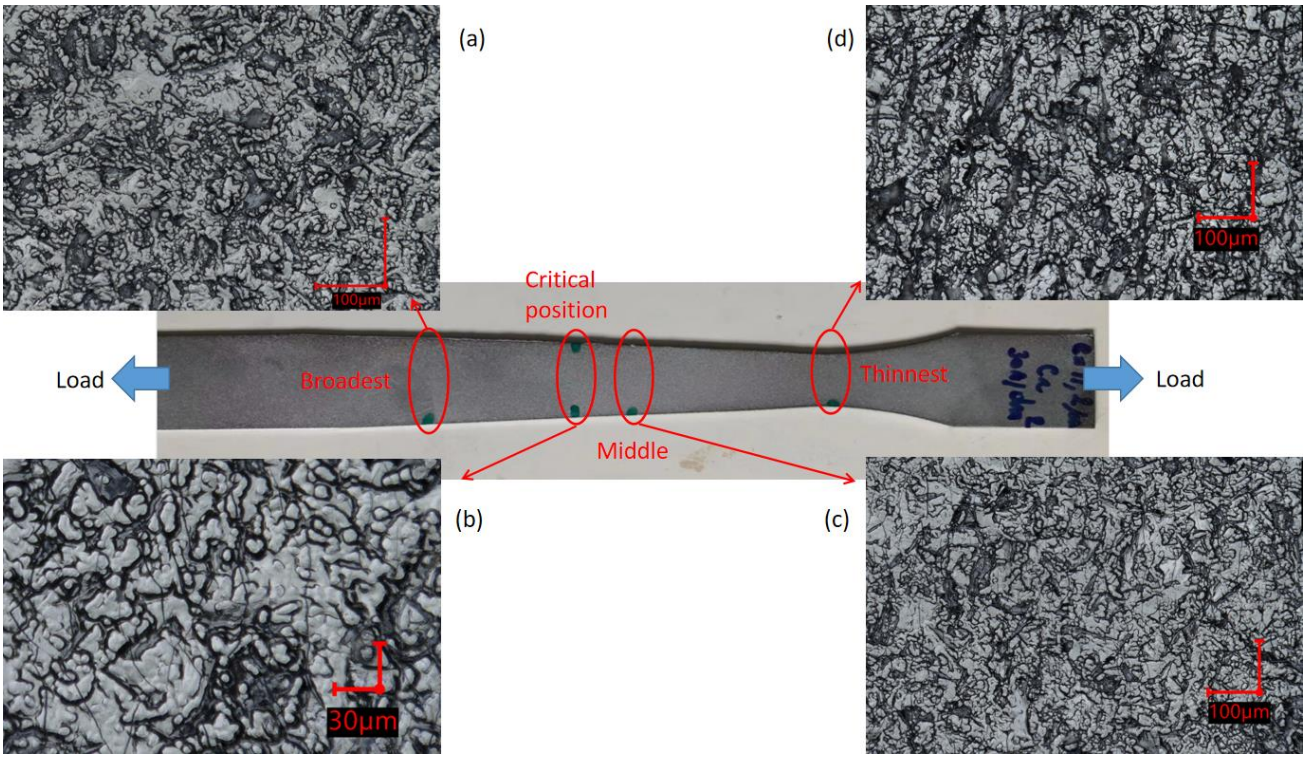

Figure III-17. *Cr-VI coated specimen under microscope in different location: (a) the broadest part; (b) the critical position (c) the middle part and (d) the thinnest part.*

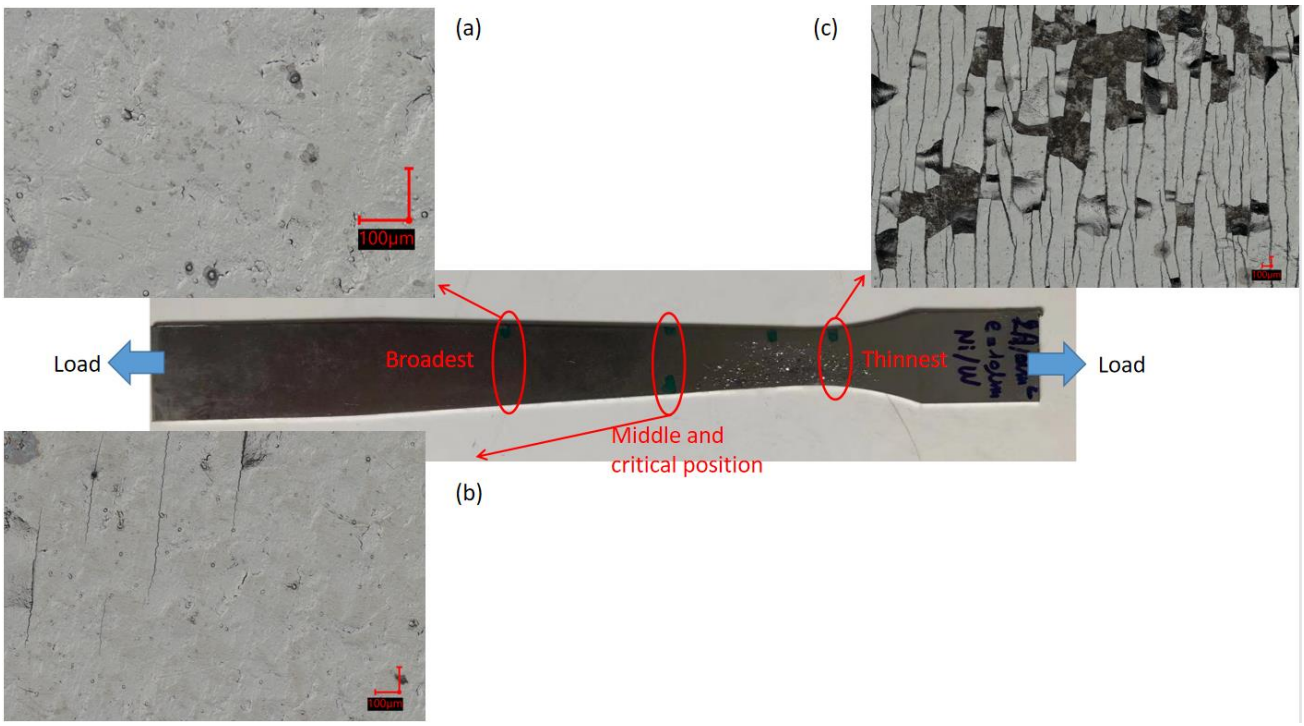

Figure III-18. *NiW-2A coated specimen under microscope in different location: (a) the broadest*

part; (b) the middle and critical position (c) the thinnest part.

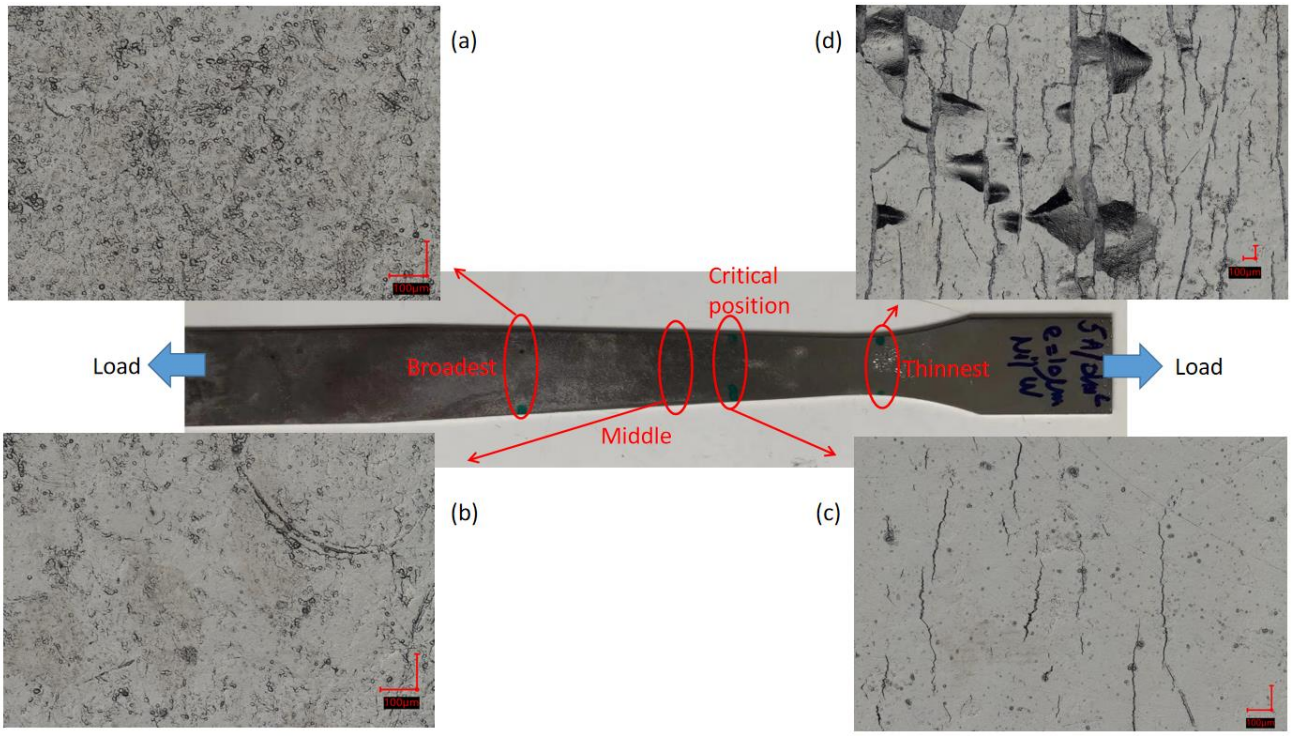

Figure III-19. *NiW-5A coated specimen under microscope in different location: (a) the broadest part; (b) the middle part (c) the critical position and (d) the thinnest part.*

Figure III-20. *Specimen pure Ni coated before and after tensile test.*

From the images of microscope, it is easy to find out that Cr-VI coating's behavior differs from NiW coatings. The most important is to determine the location where cracks appear on surface (critical position) and measure the corresponding width. The section of the location can be calculated by the thickness of the specimens and the corresponding width on the surface. The loads for the experiments

are known. So the stress can be calculate as Table III-6.

Table III-6. *The result of tensile test for four coatings*

Coatings	Thickness Coating+substrate e (mm)	Width at critical position b (mm)	Section S_0 (mm^2)	Load F (N)	Engineering Stress F/S_0 (MPa)
Cr-VI	0.8112	18.04	14.65	3905	266.5
NiW-2A	0.810	16.42	13.30	3947	296.7
NiW-5A	0.810	15.72	12.73	4068	319.5
Ni	0.810	\	\	3863	\

As the Hollomon constant are known for the steel substrate, in the homogenous elasto-plastic zone, the true strains of the substrate during the tensile tests are known if the stress is well defined. So, the Table III-7 gives out the true critical strain and critical stress when the cracks initiate.

Table III-7. *The critical stress and strain for coatings starting to crack.*

Coatings	True critical stress σ_{crit} (MPa)	True critical strain ε_{crit}
Cr-VI	266	0.12
NiW-2A	234	0.19
NiW-5A	252	0.27

In Table III-7, the true critical strain is named ε_{crit} which is at the crack starting position mentioned in chapter I. Figure III-21 and Figure III-22 show us the higher magnification of cracks on the surface at the critical position and the thinnest part for NiW-2A and NiW-5A respectively. By adjusting the scale of the surface, 6 lines with the length of 2000 μm are draw as standard to count the cracks. The lines are always draw to avoid the flakes.

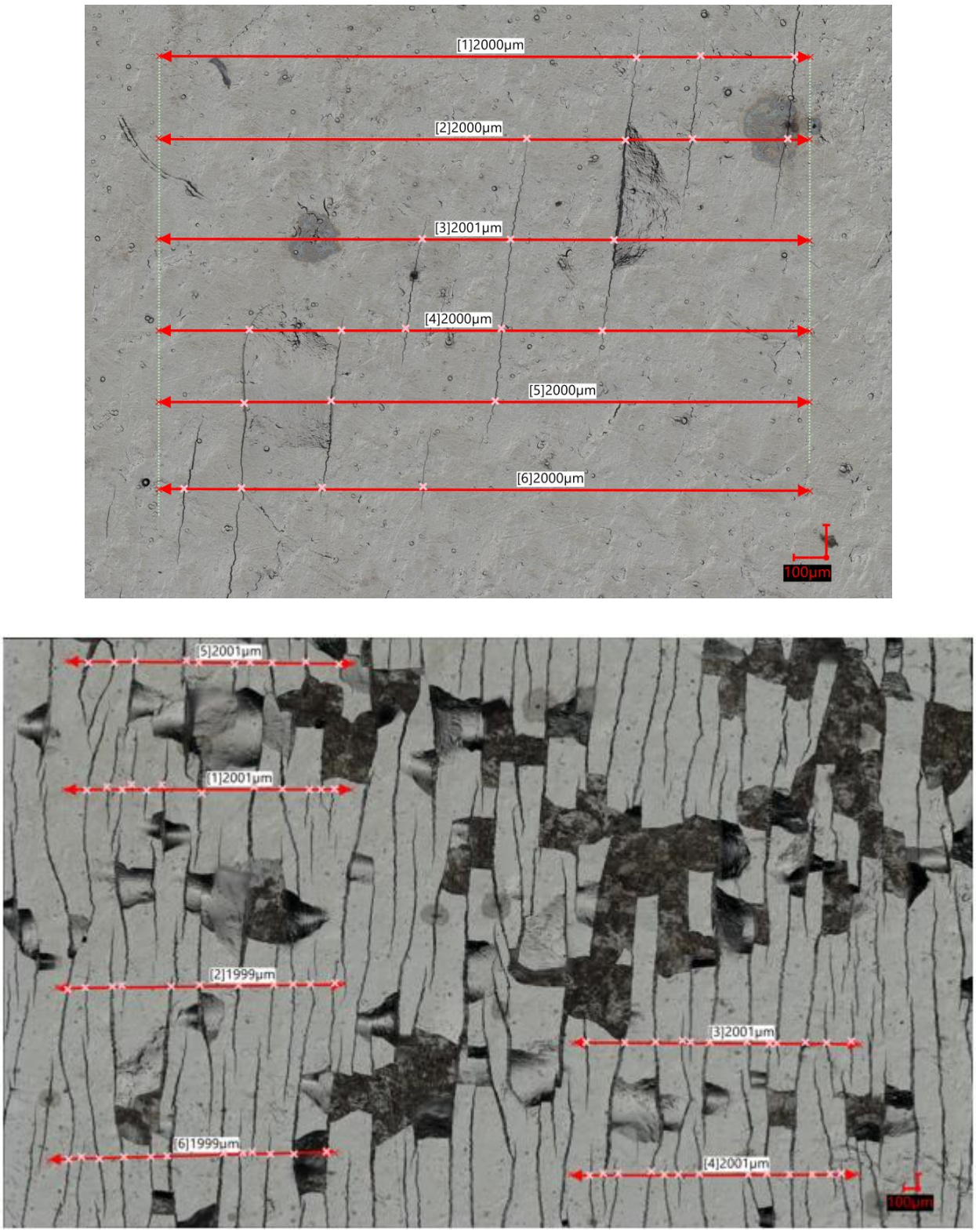

Figure III-21. *Schematic about counting cracks of NiW-2A (a) the critical position and (b) the thinnest part.*

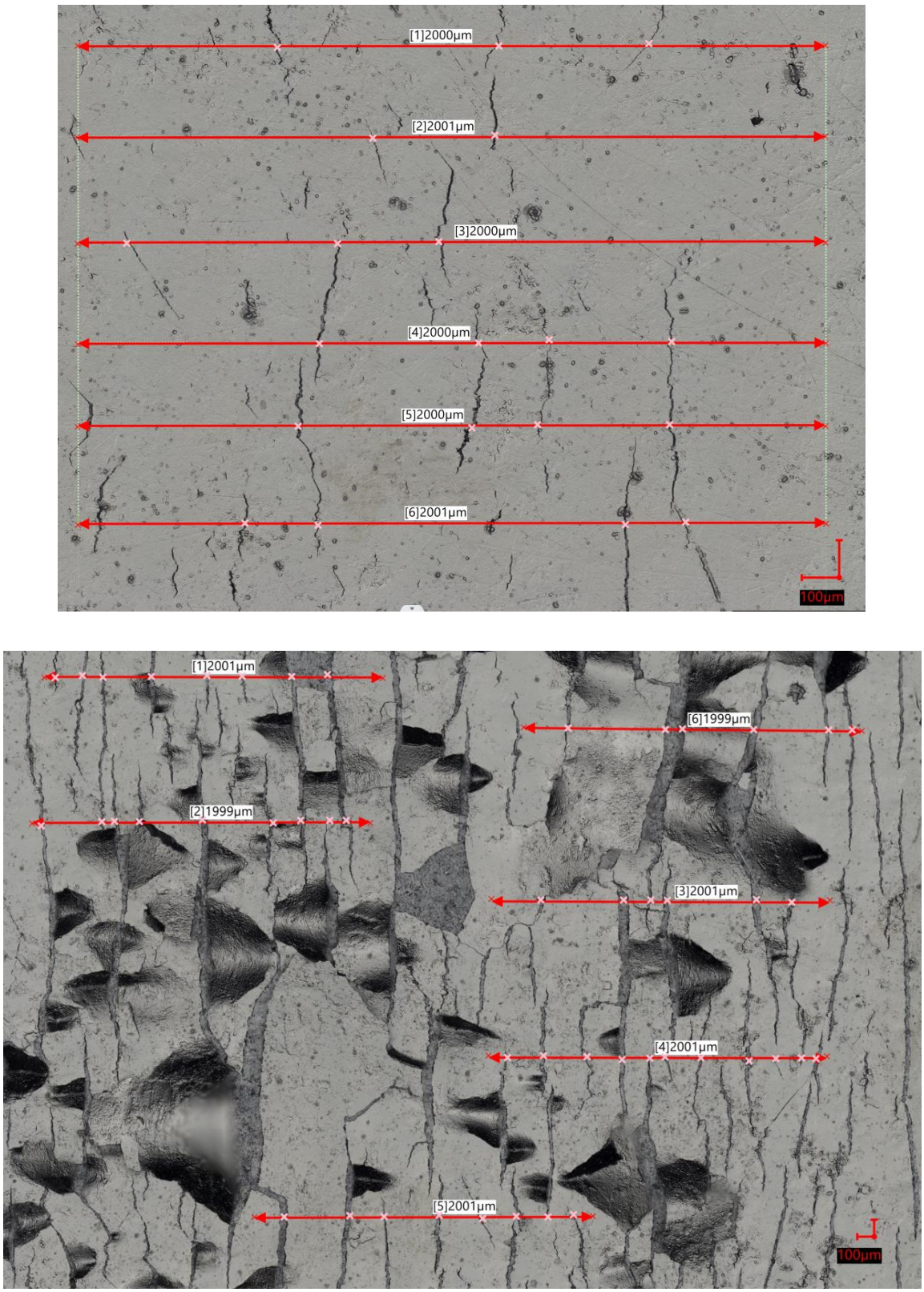

Figure III-22. *Schematic about counting cracks of NiW-5A. (a) the critical position and (b) the thinnest part.*

Table III-8. *The number of cracks for critical position and thinnest position of NiW-2A and NiW-5A coatings.*

Number of the lines	NiW-2A		NiW-5A	
	Critical position	**Thinnest position**	**Critical position**	**Thinnest position**
1	3	10	3	8
2	4	12	2	9
3	3	11	3	6
4	5	12	4	11
5	3	12	5	8
6	4	13	5	6
Average	3.7	11.7	3.7	8.0

In Table III-8, more details about the number of cracks are listed (counted by Figure III-21 and III-22). From this information, the crack density ***CD*** can be calculated [95]:

$$CD = (1 + \varepsilon)\frac{c_n}{ml} \quad \text{(III-3)}$$

Here c_n is the number of cracks, m is the number of the lines and l is the length of the lines.

For NiW-2A, the crack density is ***CD***=0.367 mm^{-1} at the crack starting position (ε_{crit}), while for NiW-5A it is ***CD***=0.349 mm^{-1}.

But the tendency of the crack density is still unknown in this work. The next step is to explore this part and it is also the preparation for calculating the interfacial shear strength (IFSS). After this first set of experiments to test the feasibility of IFSS evaluation, only NiW samples are prone to crack as predicted by the model. For further investigation, only these two samples are in-deep analyzed.

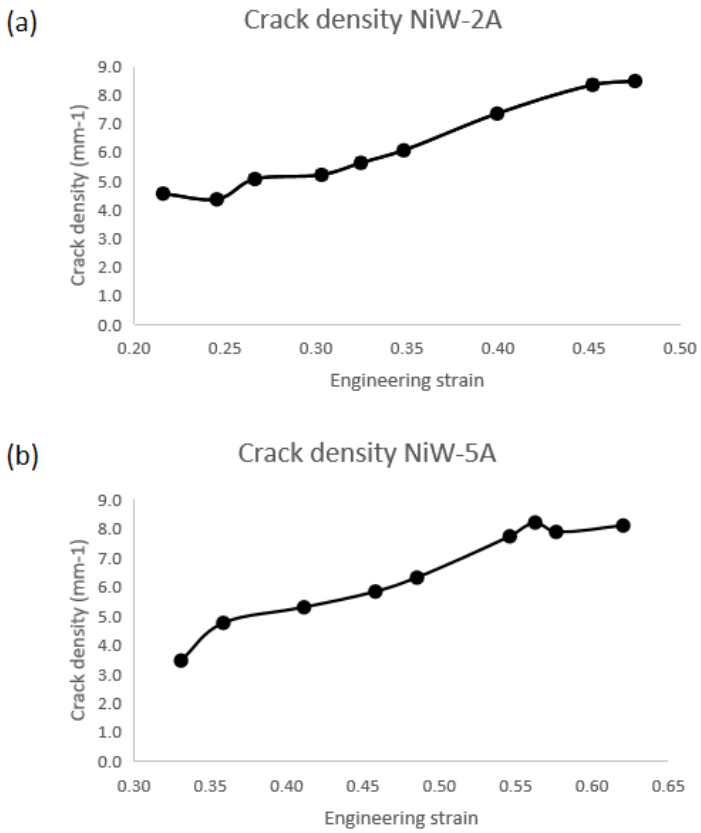

Figure III-23. *The tendency of CD (crack density) with strain.*

Figure III-23 shows the evolution of crack density (CD) with engineering strain (equation III-3). In this graph, for both NiW-2A and NiW-5A, the saturation points are not clearly reached. Further experiments and more information are necessary for calculating interfacial shear strength.

Since the pure Ni shows no cracks until it is broken, we cannot consider the fracture stress and strain of it. We can consider a good cohesion between the substrate and the coating, that means the coating deformation follows the deformation of the substrate before broke. Pure Ni coating has the best adhesion, which is due to its high ductility, but it is too soft to protect the substrate because the Vickers hardness is around 0.63 GPa [96], meanwhile the hardness is around 4.4 GPa and 5.0 GPa for NiW-2A and NiW-5A respectively in this work.

For the other three coatings, Cr-VI coating is very hard but when the strain goes to 12%, this kind of coatings are going to be damaged. In this perspective, Cr-VI seems more fragile than NiW coatings. And the cracks are too irregular to make a further analysis. NiW-2A has close properties with NiW-

5A, since they are made by the same composition and very similar electroplating conditions except the current (details are mentioned in Chapter II). NiW-5A has a better toughness behavior and the stress starting to crack is around 252 GPa while strain is 27% as can be seen in Table III-7.

3.3 Conclusions

In this section, two protocols of XRD test are applied to different coatings. The corresponding coatings and experiments are listed in Appendix I.

For the first protocol of the XRD test, Cr-VI is used as a benchmark and a preferred orientation is observed for this coating. There are 200 ℃, 400 ℃ and 600 ℃ heat treatments applied to Cr-VI in order to know the influence of temperature on our coatings structure and on the inner stress. From this test, it is found that the heat treatment indeed helps to release the stress inside the coating and it may be due to the removing of the dislocations or the recrystallization. But it should be noticed as well that the preferred orientation of Cr-VI does not change, at least under 600 ℃.

After we got an idea about the influence from increasing of temperature, new tests for NiW groups are planned. The three groups of C+, G and C- of NiW contain different percentage of tungsten and the electroplating current density is not the same either. In this way, the influence of the tungsten content with different temperatures can be investigated. According to the phases diagram of NiW, the test temperature are selected as room temperature, 300 ℃, 500 ℃, 700 ℃ and 900 ℃. The result shows us again that the heat treatment help to release the stress. Besides the lattice parameters are calculated during the tests, which indicate that a higher percent of tungsten (group C+) leads to a larger lattice parameter due to the larger size of tungsten atoms than nickel atoms.

Then the *in-situ* XRD are realized for the NiW-2A and NiW-5A, which are compared and discussed in chapter II. In this test, the specimens are scanned with X-rays during the heat-treatment under vacuum. Indentation tests reported in chapter II give out similar hardness for both NiW coatings (2A and 5A), but here, they have different preferred orientations. This test proved the result of the previous *ex-situ* XRD test and give the crystallite size of NiW-2A at 32.50 nm while NiW-5A is at 38.20 nm and 33.58 nm for the two preferred orientations (peaks) after the full relaxation of stress above 700 ℃.

The crystallite size increases after the heat treatment, which also means the stress released after the heat.

After the phases and structures exploration, the crack analysis research by indentation crack length method, scratch test and tensile test are carried out.

The indentation crack length method and scratch test do not give reliable results due to the material properties and thickness of our coatings respectively.

In tensile test, the substrate ST37 is fully characterized and its behavior's law is established. Then, Cr-VI, NiW-2A, NiW-5A and pure Ni coatings deposited on trapezoidal ST37 substrate are tested. The pure Ni coating has a good ductility, which causes no cracks on the surface until the specimen break. So, we cannot analyze it. For other three coatings, we focus on the position of starting of cracks. By the analysis, the Cr-VI can bear the highest stress before cracking but at a low strain. Comparing to NiW-2A, NiW-5A has a higher stress and strain when it starts to crack.

Besides, the crack density of NiW-2A and NiW-5A is calculated as well, while it is impossible for Cr-VI because the expected crack network does not generate on Cr-VI and the model cannot be applied. As general overview, NiW-5A is slightly better than NiW-2A on adhesion and interfacial toughness.

Chapter IV. General conclusion and perspectives

In this work, the main aim is to compare the electroplating coatings of Cr-VI and different NiW in mechanical properties and structures. Theoretical background and former studies are presented in chapter I. The indentation tests are applied for the mechanical properties while XRD tests are for structures revealing. Furthermore, the cracks formation analysis is done for the information of adhesion and toughness behaviors.

In chapter II, for the indentation part, this work focus on the hardness comparison among Cr-VI, NiW-2A and NiW-5A. At the very beginning of the work, the nano-indentation was planned, but due to high roughness on coating surface results are not reliable. A transformation of the surface (by polishing for example) is not suitable due to potential defects introduce in the material (stress release, work hardening…). This is the main reason that this work is carried out the indentation test in micro scale to avoid detrimental influence of roughness. In addition, the substrate will be used in the industry without any transformation of the surface.

Firstly, we tried to characterize the Cr-VI coating from both the top surface and the cross-section surface. In this step, attention is paid on the ISE and three models are compared: Bull and Page, Li and Bradt and Nix and Gao models. For the tested samples, all the models work well and give out clear results. But we have no criteria to select which one is the best in our work. After that, the tip defect is taken into account as well. The tip defect can be determined by two methods, but in order to compare with parameters involved in the ISE models, we select the notion of indenter tip defect $\boldsymbol{h_b}$. After the tip defect applied into correction, the ISE value of three models will be very close to zero. But for Bull & Page and Nix & Gao models give out negative value which has no physical meaning. This is due to the over correction of ISE and tip defect. Finally, it turns out the similar result: on the top surface of Cr-VI, the hardness is around 8.0 GPa while on cross section it is 8.5 GPa.

Before the study on the NiW coating, we have to be clear that on the Cr-VI top surface, only three data points are selected which corresponding to a very low indenter displacement (less than 10% of

the thickness). This makes that the substrate has very small or no influence when we test our samples. But for NiW coatings, the indenter displacement is much larger and the thickness is less than Cr-VI. So, the substrate influence during the test must be considered. Owing to the situation of the experiments and known information of the materials, Jönsson and Hogmark model is applied to correct it. The constant C, which represent the brittle or ductile properties of samples, in the model is fully discussed as well. When constant C equals or is very close to 1, the results are more reliable than the value 0.5. Finally, it is found out that the hardness of the NiW-2A coating is 4.4 GPa, while it is 5.0 GPa for NiW-5A.

Following the classical test, the instrumented indentation tests are also applied on the Cr-VI cross-section surface. By this test, the Young's modulus and hardness are researched. The compliance influence and some models are discussed in chapter II. Besides, the tip defect is also considered when analysis the hardness and modulus. This test gives the information: the instrumented hardness $H_{IT} = 11.2 \pm 0.9$ GPa, the Martens hardness $H_M = 7.9 \pm 0.5$ GPa, and instrumented elastic modulus is $E_{IT} = 308 \pm 15$ GPa.

In a further study, if a smother surface of the coatings can be prepared, the nano indentation test is strongly recommended to apply on the samples. And the NiW could be electroplated by more different current density in order to observe the influence of this condition on the hardness. Additionally, the tungsten content of the coating could be another interesting variable for experiments.

In the structure and cracks formation chapter, the work mainly focuses on the XRD test and the tensile test.

Before the test, the metallic etching and grain size observation are made. Though because of the galvanic coupling, only the substrates are etched deeper and deeper, and there is no change for the coatings. So, the XRD will be the main method for us to get information of the structures.

Firstly, the Cr-VI coatings with different temperatures of heat treatment are tested. These test for Cr-VI conclude that the heat treatment can influence the inner stress of coatings but does not change the preferred orientations.

Then three groups of NiW coating are subjected to heat treatments according to the phases diagram and analyzed by X-rays diffraction. It is interesting to figure out the range of the lattice parameters of every group of the NiW and we make it clear that this is influence by the content of the tungsten atoms. It makes sense that when there are more large atoms (tungsten), the lattice parameter increases. Then the *in-situ* XRD are realized for the NiW-2A and NiW-5A. From this test, the crystallite size of both NiW after fully heated, which means fully release of the inner stress, is calculated: for NiW-2A is 32.50 nm and for NiW-5A the corresponding peak is 38.20 nm.

In the crack formation part, the main attention is paid to analyze different type of cracks. Indentation crack length method is interesting and convenient way to analyze the toughness and elastic modulus. But the precondition of this method is that the samples can generate regular cracks (line cracks) to be measured. In our situation, there are only circular cracks which do not fit the theory mentioned in chapter I. For the scratch test, it can provide information by comparing the critical load during scratching. From both the load curve and the image of the scratch on the surface, it is very difficult to determine where is the critical loads and critical positions. This problem is due to the coatings' thickness. And for the Rockwell adhesion test, the same problem obstructs us to get a good result.

We introduce a characterization by tensile test. The steel substrate ST37 is firstly characterized and its behavior's law is established. When this information is known, we need the critical stress to make it easier to compare the different coatings. A trapezoid shape of the samples is applied, in which with only one test, several states of stress/strain can be revealed.

Among all the coatings, pure Ni has no cracks until it is broken, which is because of the good ductility. Cr-VI coating seems the hardest one in our work, but it will start cracking at a low strain. For the two NiW coatings, the NiW-5A has slightly higher critical strain than NiW-2A. In general, NiW-5A has the best adhesion and the surface toughness behaviors.

In a further study, a proper (thinner) thickness of coatings for the scratch test should be applied. And for the NiW-2A and NiW-5A coatings, since there are regular cracks, the crack density at the saturation can be found and the interfacial shear stress can be calculated as well. More quantitative comparison

can be made between them.

Besides, the corrosion properties comparison between NiW and Cr-VI is also an interesting perspective. The corrosion resistance of NiW coatings was related to three main factors: 1) tungsten content, 2) volume of grain boundaries which may act as potential sites for corrosion reactions, and 3) the crystallographic texture of coatings [97]. So from the result of XRD in this work and a better experiment of metallic etching method, there shall be more new and interesting conclusions. Our colleagues who work on this part get the information that NiW-5A has better corrosion resistance than other Cr-VI replacement.

To put in a nutshell, until now, there is few chances to find one single replacement for Cr-VI to meet all the needs in the various field of applications. If the users are looking for a good wear resistance (high hardness), NiW coatings may not be a perfect replacement whereas NiB coating could be a possible choice. NiB coating developed in this project by other partners has very similar hardness with Cr-VI and after heat treatment, this value could be even higher. But when we pursue a high corrosion resistance with modest wear resistance, NiW will work very well.

Appendix I. Samples in this work

Table A-1. *The samples used in this work for different experiments. The mainly differences are presented in the 'Features' column.*

Coating	Features		Classical indentation	Instrumented indentation	XRD	In-situ XRD	Tensile test	Scratch test
Cr-VI	Electroplated by 40 A/dm^2		X	X	X		X	X
NiW-2A	Electroplated	2A/dm^2 W/(W+Ni)=12-17%at	X		X	X	X	X
NiW-5A		5A/dm^2 W/(W+Ni)=12-17%at	X		X	X	X	X
NiW C-		10A/dm^2 W/(W+Ni)=9.6%at Heat treatment*			X			
NiW C+		5A/dm^2 W/(W+Ni)=16.3%at Heat treatment*			X			
NiW G		8A/dm^2 W/(W+Ni)=2.7%at Heat treatment*			X			
Pure Ni							X	X

**The heat treatments are applied under the temperatures of 300°C, 500°C, 700°C, 900°C.*

Appendix II. Metallic etching and grain size observation

The inner structure of a metal is made up of individual crystalline areas known as ‘grains’. The structure, size and orientation of these grains result from the material composition (alloy) and the way the material is made (*e.g.* forging, casting or additive manufacturing). The grains are formed from the molten material when it solidifies, interact with one another and with other ingredients, like phases and contaminations. Typically, the grain structure is adapted to the technical application.

Grain size and orientation and other structural characteristics are directly linked to the mechanical and technological properties of these materials. Structural characteristics also depend on subsequent external influences. These influences include:

a) Chemical influences (e.g. corrosion);

b) Chemical and/or physical influences (e.g. heat treatment processes);

c) Mechanical influences (e.g. following the forming processes, such as forging, rolling, bending, etc.).

In this work, the NiW and Cr-VI coatings are supposed to be observed by this method. All the specimens are cut and cold mounted in epoxy resin. Then the prepared specimens and resin are ground on grade 220 SiC using water as a lubricant. They are then polished on different cloths with diamond paste of size 6 μm, 3 μm and 1 μm. Fine polishing is then performed with alumina suspension of size 0.25 μm. The well-prepared specimens are shown as Figure A-1.

Figure A-1. *An example of the well-prepared metallic etching specimens.*

Without etching, it was possible to observe the cross-sectional thickness of the various coatings, and to document the presence of cracks.

Etching was performed in order to reveal the grain structure of the coatings. Nital (4% nitric acid in ethanol) was used, with increasing amounts of nitric acid (up to 20%) and hydrofluoric acid additions (up to 5%), at a controlled temperature of 50°C.

The experiment time is selected as 1 min, 3 min, 5 min and 10 min, in order to observe the etching process. But unfortunately, the coatings didn't react with etchants. Only the substrate was more and more deeply etched. This was attributed to galvanic coupling. In the next step of this test, if we want to observe the etching of the coating, the separating of the substrate and coating is necessary.

Appendix III. Images of the indentation cracks' radius

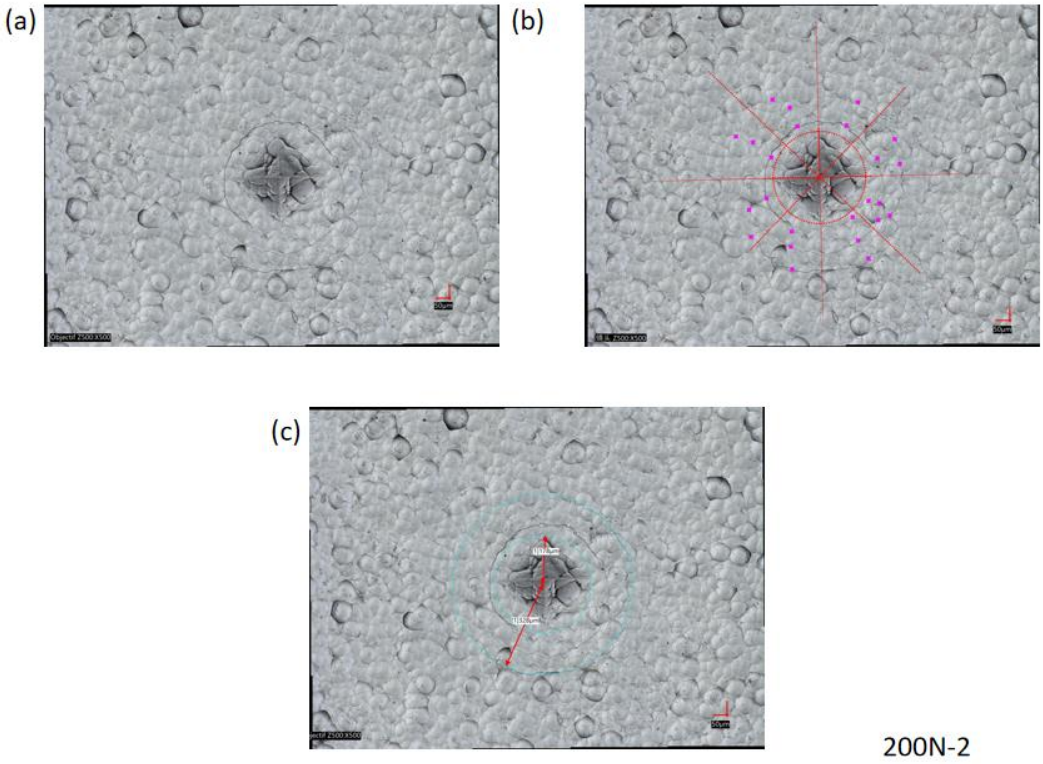

Figure A-2. *Schematics for the 2nd 200N imprints of (a) the bare cracks, (b) the determination of isotropic and (c) the measurements of the imprint and outermost crack radius.*

This part is as a complement for the scratch test in the manuscript in order to show more details. This part is as a complement for the scratch test in the manuscript. From Figure A-2 to A-5 are the pictures for 200N, 300N and 500N respectively. All the figures include a bare crack without any analysis (a); a schematic to show how to count cracks around the imprints (b) and a schematic to show how to measure the radius.

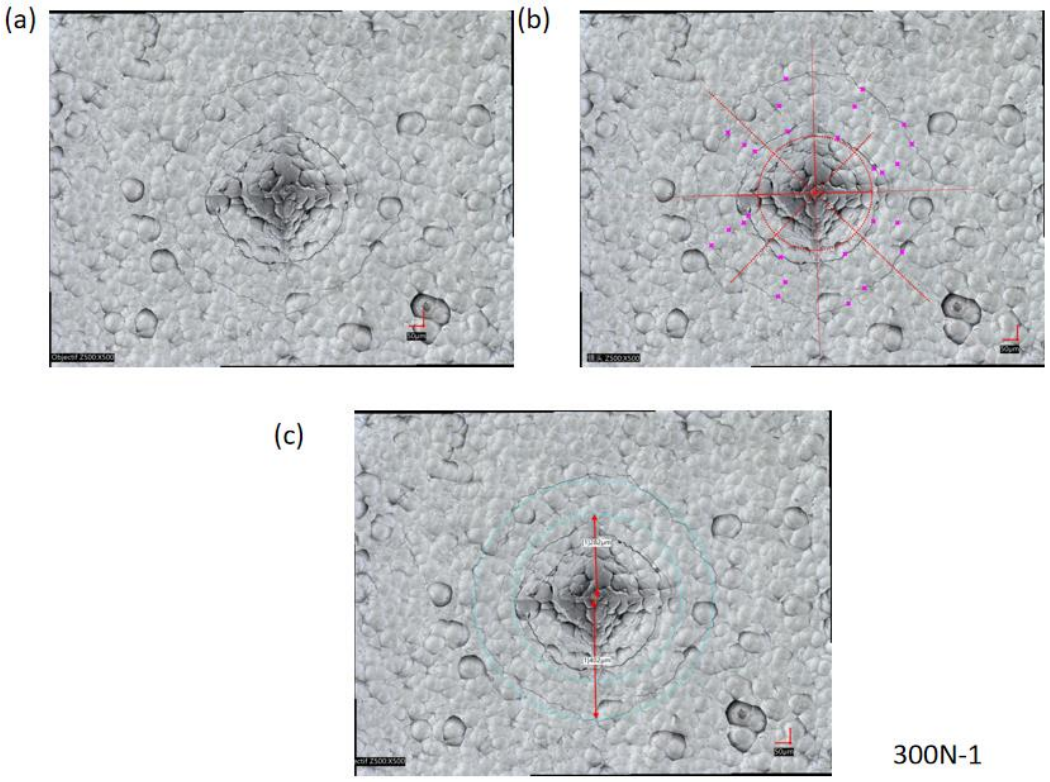

Figure A-3. *Schematics for the 1st 300N imprints of (a) the bare cracks, (b) the determination of isotropic and (c) the measurements of the imprint and outermost crack radius.*

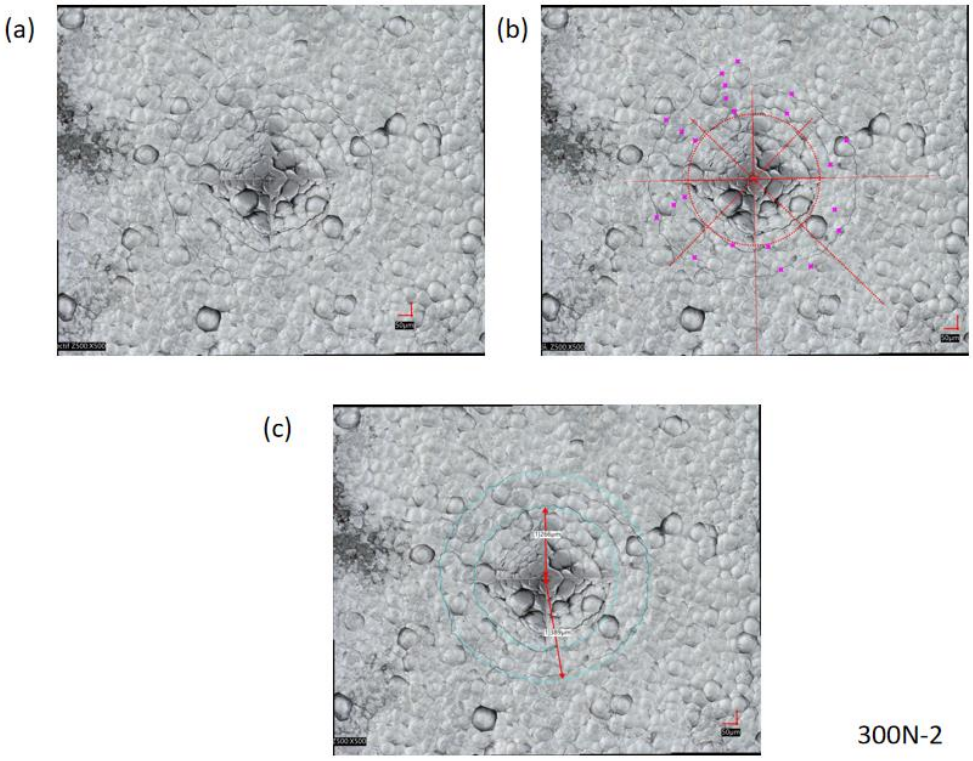

Figure A-4. *Schematics for the 2nd 300N imprints of (a) the bare cracks, (b) the determination of isotropic and (c) the measurements of the imprint and outermost crack radius.*

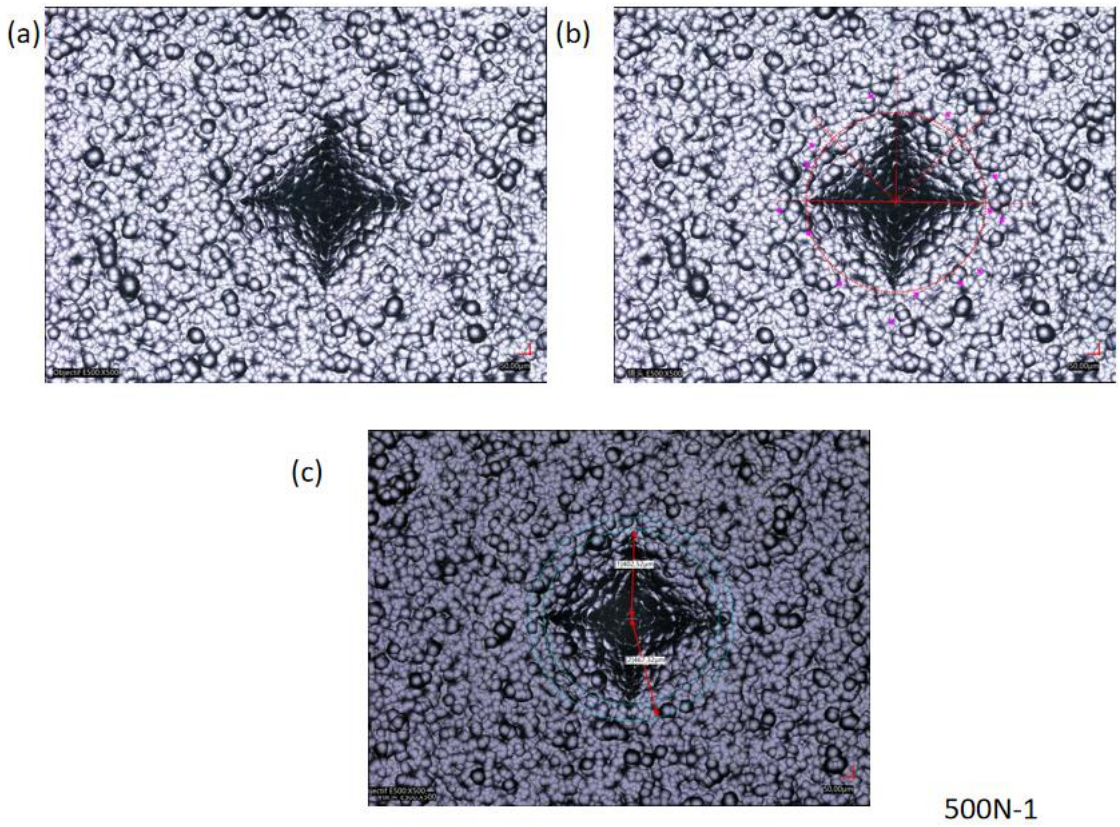

Figure A-5. *Schematics for the 1st 500N imprints of (a) the bare cracks, (b) the determination of isotropic and (c) the measurements of the imprint and outermost crack radius.*

References

[1] A. V. Chernogor, F. F. Klimashin, A. O. Volkhonskii, I. V. Blinkov, and P. H. Mayrhofer, "The impact of Ni and Mo on growth-morphology and mechanical properties of arc evaporated Ti-Cr-N hard coatings," *Surf. Coatings Technol.*, vol. 377, no. August, p. 124917, 2019, doi: 10.1016/j.surfcoat.2019.124917.

[2] F. J. He, M. Wang, and X. Lu, "Properties of electrodeposited amorphous Fe-Ni-W alloy deposits," *Trans. Nonferrous Met. Soc. China (English Ed.*, vol. 16, no. 6, pp. 1289–1294, 2006, doi: 10.1016/S1003-6326(07)60008-9.

[3] M. Cieślak-Golonka, "Toxic and mutagenic effects of chromium(VI). A review," *Polyhedron*, vol. 15, no. 21, pp. 3667–3689, 1996, doi: 10.1016/0277-5387(96)00141-6.

[4] J. P. Wise, J. L. Young, J. Cai, and L. Cai, "Current understanding of hexavalent chromium [Cr(VI)] neurotoxicity and new perspectives," *Environ. Int.*, vol. 158, p. 106877, 2022, doi: 10.1016/j.envint.2021.106877.

[5] A. Liang, Y. Li, H. Liang, L. Ni, and J. Zhang, "A favorable chromium coating electrodeposited from Cr(III) electrolyte reveals anti-wear performance similar to conventional hard chromium," *Mater. Lett.*, vol. 189, pp. 221–224, 2017, doi: 10.1016/j.matlet.2016.12.022.

[6] F. Rosalbino, G. Scavino, G. Mortarino, E. Angelini, and G. Lunazzi, "EIS study on the corrosion performance of a Cr(III)-based conversion coating on zinc galvanized steel for the automotive industry," *J. Solid State Electrochem.*, vol. 15, no. 4, pp. 703–709, 2011, doi: 10.1007/s10008-010-1140-7.

[7] S. Mahdavi, S. R. Allahkaram, and A. Heidarzadeh, "Characteristics and properties of Cr coatings electrodeposited from Cr(III) baths," *Mater. Res. Express*, vol. 6, no. 2, 2019, doi: 10.1088/2053-1591/aaeb4f.

[8] N. P. Wasekar and G. Sundararajan, "Sliding wear behavior of electrodeposited Ni-W

alloy and hard chrome coatings," *Wear*, vol. 342–343, pp. 340–348, 2015, doi: 10.1016/j.wear.2015.10.003.

[9] A. R. Jones, J. Hamann, A. C. Lund, and C. A. Schuh, "Nanocrystalline Ni-W alloy coating for engineering applications," *Natl. Assoc. Surf. Finish. Annu. Tech. Conf. 2009, SUR/FIN 2009*, no. May, pp. 285–301, 2009.

[10] *ISO 14577: Metallic Materials - Instrumented Indentation Test for Hardness and Materials Parameters.* International Organization for Standardization, Geneva, 2002.

[11] E. Broitman, "Indentation Hardness Measurements at Macro-, Micro-, and Nanoscale: A Critical Overview," *Tribol. Lett.*, vol. 65, no. 1, pp. 1–18, 2017, doi: 10.1007/s11249-016-0805-5.

[12] S. M. Walley, "Historical origins of indentation hardness testing," *Mater. Sci. Technol. (United Kingdom)*, vol. 28, no. 9–10, pp. 1028–1044, 2012, doi: 10.1179/1743284711Y.0000000127.

[13] R. L. Smith and G. E. Sandland, "An Accurate Method of Determining the Hardness of Metals," *Proc. Inst. Mech. Eng.*, no. May, pp. 623–641, 1922.

[14] "National Physics Laboratory UK Report for the Year 1932, pp. 180–181. National Physics Laboratory, Teddington (1993).pdf." .

[15] A. E. Giannakopoulos, P. L. Larsson, and R. Vestergaard, "Analysis of Vickers indentation," *Int. J. Solids Struct.*, vol. 31, no. 19, pp. 2679–2708, 1994, doi: 10.1016/0020-7683(94)90225-9.

[16] N. A. Sakharova, J. V. Fernandes, J. M. Antunes, and M. C. Oliveira, "Comparison between Berkovich, Vickers and conical indentation tests: A three-dimensional numerical simulation study," *Int. J. Solids Struct.*, vol. 46, no. 5, pp. 1095–1104, 2009, doi: 10.1016/j.ijsolstr.2008.10.032.

[17] F. Knoop, C. G. Peters, and W. B. Emerson, “A sensitive pyramidal-diamond tool for indentation measurements,” *J. Res. Natl. Bur. Stand. (1934).*, vol. 23, no. 1, p. 39, 1939, doi: 10.6028/jres.023.022.

[18] S. Rockwell, H., Rockwell, “Hardness tester,” USA Patent 1294171, 1914.

[19] *ISO 6508-1: Metallic Materials—Rockwell Hardness Test—Part 1: Test Method.* International Organization for Standardization, Geneva, 2016.

[20] *ASTM E18-16: Standard Test Methods for Rockwell Hardness of Metallic Materials.* ASTM International, West Conshohocken, 2016.

[21] *ISO 2039-2: Plastics—Determination of Hardness—Part 2: Rockwell Hardness.* International Organization for Standardization, Geneva, 1987.

[22] W. C. Oliver and G. M. Pharr, “An Improved Technique for Determining Hardness and Elastic Modulus Using Load and Displacement Sensing Indentation Experiments.,” *Mater. Res. Soc.*, no. 1, pp. 1564–1583, 1992.

[23] S. J. Bull, T. F. Page, and E. H. Yoffe, “An explanation of the indentation size effect in ceramics,” *Philos. Mag. Lett.*, vol. 59, no. 6, pp. 281–288, 1989, doi: 10.1080/09500838908206356.

[24] M. Troyon and L. Huang, “Comparison of different analysis methods in nanoindentation and influence on the correction factor for contact area,” *Surf. Coatings Technol.*, vol. 201, no. 3–4, pp. 1613–1619, 2006, doi: 10.1016/j.surfcoat.2006.02.033.

[25] M. Yetna N'jock, D. Chicot, J. M. Ndjaka, J. Lesage, X. Decoopman, F. Roudet and A. Mejias, “A criterion to identify sinking-in and piling-up in indentation of materials,” *Int. J. Mech. Sci.*, vol. 90, pp. 145–150, 2015, doi: 10.1016/j.ijmecsci.2014.11.008.

[26] J. L. Loubet, M. Bauer, A. Tonck, S. Bec, and B. Gauthier-Manuel, “Nanoindentation with a Surface Force Apparatus,” *Mech. Prop. Deform. Behav. Mater. Having Ultra-Fine*

Microstruct., pp. 429–447, 1993, doi: 10.1007/978-94-011-1765-4_28.

[27] D. Grabco, O. Shikimaka, and E. Harea, "Translation-rotation plasticity as basic mechanism of plastic deformation in macro-, micro- and nanoindentation processes," *J. Phys. D. Appl. Phys.*, vol. 41, no. 7, 2008, doi: 10.1088/0022-3727/41/7/074016.

[28] Y. Benarioua, F. Roudet, and D. Chicot, "Influence of the indenter tip defect in classical indentation: Application to the hardness determination of DLC thin films," *Mater. Sci. Eng. A*, vol. 662, pp. 268–274, 2016, doi: 10.1016/j.msea.2016.03.067.

[29] H. Li and R. C. Bradt, "The microhardness indentation load/size effect in rutile and cassiterite single crystals," *J. Mater. Sci.*, vol. 28, no. 4, pp. 917–926, 1993, doi: 10.1007/BF00400874.

[30] Y. Huang, F. Zhang, K. C. Hwang, W. D. Nix, G. M. Pharr, and G. Feng, "A model of size effects in nano-indentation," *J. Mech. Phys. Solids*, vol. 54, no. 8, pp. 1668–1686, 2006, doi: 10.1016/j.jmps.2006.02.002.

[31] J. H. Westbrook; H. Conrad, *The Science of Hardness Testing and its Research Applications*. American Society for Metals, 1973.

[32] S. H. B.Jönsson, "Hardness measurements of thin films," *Thin Solid Film.*, vol. 114, pp. 257–269, 1984.

[33] D. Chicot and J. Lesage, "Absolute hardness of films and coatings," *Thin Solid Films*, vol. 254, no. 1–2, pp. 123–130, 1995, doi: 10.1016/0040-6090(94)06239-H.

[34] E. S. Puchi-Cabrera, "A new model for the computation of the composite hardness of coated systems," *Surf. Coatings Technol.*, vol. 160, no. 2–3, pp. 177–186, 2002, doi: 10.1016/S0257-8972(02)00394-8.

[35] A. M. Korsunsky, M. R. McGurk, S. J. Bull, and T. F. Page, "On the hardness of coated systems," *Surf. Coatings Technol.*, vol. 99, no. 1–2, pp. 171–183, 1998, doi: 10.1016/S0257-

8972(97)00522-7.

[36] P. J. Burnett and D. S. Rickerby, “The mechanical properties of wear-resistant coatings. I: Modelling of hardness behaviour,” *Thin Solid Films*, vol. 148, no. 1, pp. 41–50, 1987, doi: 10.1016/0040-6090(87)90119-2.

[37] B. R. Lawn, A. G. Evans, and D. B. Marshall, “Elastic/Plastic Indentation Damage in Ceramics: The Median/Radial Crack System,” *J. Am. Ceram. Soc.*, vol. 63, no. 9–10, pp. 574–581, Sep. 1980, doi: 10.1111/j.1151-2916.1980.tb10768.x.

[38] J. R. Tuck, A. M. Korsunsky, R. I. Davidson, S. J. Bull, and D. M. Elliott, “Modelling of the hardness of electroplated nickel coatings on copper substrates,” *Surf. Coatings Technol.*, vol. 127, no. 1, pp. 1–8, 2000, doi: 10.1016/S0257-8972(00)00537-5.

[39] Q. S. Paduano, D. W. Weyburne, and A. J. Drehman, “An X-ray diffraction technique for analyzing structural defects including microstrain in nitride materials,” *J. Cryst. Growth*, vol. 318, no. 1, pp. 418–422, 2011, doi: 10.1016/j.jcrysgro.2010.10.019.

[40] P. B. Hirsch and J. N. Kellar, “A study of cold-worked aluminium by an X-ray microbeam technique. I. Measurement of particle volume and misorientations,” *Acta Crystallogr.*, vol. 5, no. 2, pp. 162–167, 1952, doi: 10.1107/s0365110x52000496.

[41] S. G. Qu, H. S. Lou, X. Q. Li, T. R. Kuang, and J. Y. Lou, “Effect of heat-treatment on stress relief and dimensional stability behavior of SiCp/Al composite with high SiC content,” *Mater. Des.*, vol. 86, pp. 508–515, 2015, doi: 10.1016/j.matdes.2015.07.044.

[42] R. Lin, T. Zhao, M. Shang, J. Wang, W. Tang, V. E. Guterman and J. Ma, “Effect of heat treatment on the activity and stability of PtCo/C catalyst and application of in-situ X-ray absorption near edge structure for proton exchange membrane fuel cell,” *J. Power Sources*, vol. 293, pp. 274–282, 2015, doi: 10.1016/j.jpowsour.2015.05.067.

[43] Z. Gao, C. Wang, N. Gao, S. Guo, Y. Chen, Z. Chai, Y. Wang and H. Ma, “Electrodeposited Ni-W coatings as the effective reaction barrier at Ga-21.5In-10Sn/Cu

interfaces," *Surfaces and Interfaces*, vol. 30, no. December 2021, p. 101838, 2022, doi: 10.1016/j.surfin.2022.101838.

[44] M. A. Moram and M. E. Vickers, "X-ray diffraction of III-nitrides," *Reports Prog. Phys.*, vol. 72, no. 3, 2009, doi: 10.1088/0034-4885/72/3/036502.

[45] J. Epp, *X-Ray Diffraction (XRD) Techniques for Materials Characterization*. Elsevier Ltd, 2016.

[46] B.Pinheiro, "Étude par Diffraction des Rayons X des Modifications Microstructurales em Cours de Fatigue," Lille University, 2011.

[47] B. E. Warren and B. L. Averbach, "The separation of cold-work distortion and particle size broadening in x-ray patterns," *J. Appl. Phys.*, vol. 23, no. 4, p. 497, 1952, doi: 10.1063/1.1702234.

[48] B. E. Warren and B. L. Averbach, "The separation of stacking fault broadening in cold-worked metals," *J. Appl. Phys.*, vol. 23, no. 9, p. 1059, 1952, doi: 10.1063/1.1702352.

[49] A. C. Murrieta and F. F. Contreras-Torres, "Microstructure of polycrystalline solids: A brief review from methods in X-ray line profile analysis," *Mater. Today Proc.*, vol. 48, pp. 96–100, 2020, doi: 10.1016/j.matpr.2020.10.978.

[50] B.E. Warren, *X-ray diffraction*. New York: Dover Publications, 1990.

[51] L. V. Azaroff, *Elements of X-ray Crystallography*. New York: Mc Graw-Hill, 1968.

[52] A. Khan, R. Hussain, A. M. Toufiq, A. Shah, B.A. Khan, Z. Niaz and S. ur Rahman, "Fabrication of cryptomelane FexMn1-xO2 with enhanced antibacterial activity and specific heat capacity," *Mater. Charact.*, vol. 169, no. September, p. 110661, 2020, doi: 10.1016/j.matchar.2020.110661.

[53] P. Šimonová, W. Pabst, and J. Cibulková, "Crystallite size of pure tin oxide ceramics and its growth during sintering determined from XRD line broadening – A methodological case

study and a practitioners' guide," *Ceram. Int.*, vol. 47, no. 24, pp. 35333–35347, 2021, doi: 10.1016/j.ceramint.2021.09.076.

[54] G. K. Williamson and W. H. Hall, "X-ray line broadening from filed aluminium and wolfram," *Acta Metall.*, vol. 1, no. 1, pp. 22–31, 1953, doi: 10.1016/0001-6160(53)90006-6.

[55] K. Kurashkin, V. Mishakin, and A. Rudenko, "Ultrasonic Evaluation of Residual Stresses in Welded Joints of Hydroelectric Unit Rotor Frame," *Mater. Today Proc.*, vol. 11, pp. 163–168, 2019, doi: 10.1016/j.matpr.2018.12.125.

[56] M. Duquennoy, M. Ouaftouh, M. L. Qian, F. Jenot, and M. Ourak, "Ultrasonic characterization of residual stresses in steel rods using a laser line source and piezoelectric transducers," *NDT E Int.*, vol. 34, no. 5, pp. 355–362, 2001, doi: 10.1016/S0963-8695(00)00075-X.

[57] M. Doxbeck, M. A. Hussain, J. Frankel, and A. Abbate, "Use of laser generated creeping longitudinal waves to determine residual stresses," *Proc. IEEE Ultrason. Symp.*, vol. 1, pp. 725–728, 2000, doi: 10.1109/ultsym.2000.922649.

[58] A. Moreau and C. S. Man, "Laser-ultrasonic measurements of residual stresses in a 7075-T651 aluminum sample surface-treated with low plasticity burnishing," *AIP Conf. Proc.*, vol. 820 II, no. 2006, pp. 1434–1441, 2006, doi: 10.1063/1.2184692.

[59] M. Duquennoy, D. Devos, M. Ouaftouh, D. Lochegnies, and E. Roméro, "Ultrasonic evaluation of residual stresses in flat glass tempering: Comparing experimental investigation and numerical modeling," *J. Acoust. Soc. Am.*, vol. 119, no. 6, pp. 3773–3781, 2006, doi: 10.1121/1.2197806.

[60] Y. Zhan, C. Liu, J. Zhang, G. Mo, and C. Liu, "Measurement of residual stress in laser additive manufacturing TC4 titanium alloy with the laser ultrasonic technique," *Mater. Sci. Eng. A*, vol. 762, no. July, p. 138093, 2019, doi: 10.1016/j.msea.2019.138093.

[61] M. Hayes and R. S. Rivlin, "Surface waves in deformed elastic materials," *Arch. Ration.*

Mech. Anal., vol. 8, no. 1, pp. 358–380, 1961, doi: 10.1007/BF00277451.

[62] A. Hannon and P. Tiernan, "A review of planar biaxial tensile test systems for sheet metal," *J. Mater. Process. Technol.*, vol. 198, no. 1–3, pp. 1–13, 2008, doi: 10.1016/j.jmatprotec.2007.10.015.

[63] T. Ganne, J. Crépin, S. Serror, and A. Zaoui, "Cracking behaviour of PVD tungsten coatings deposited on steel substrates," *Acta Mater.*, vol. 50, no. 16, pp. 4149–4163, 2002, doi: 10.1016/S1359-6454(02)00256-2.

[64] C. H. Hsueh, "Analyses of Multiple Film Cracking in Film/Substrate Systems," *J. Am. Ceram. Soc.*, vol. 84, no. 3–12, pp. 2955–2961, 2001, doi: 10.1111/j.1151-2916.2001.tb01120.x.

[65] Z. Zhang, Q. Sun, C. Li, and W. Zhao, "Theoretical calculation of the strain-hardening exponent and the strength coefficient of metallic materials," *J. Mater. Eng. Perform.*, vol. 15, no. 1, pp. 19–22, 2006, doi: 10.1361/10599490524057.

[66] A. J. Atanacio, B. A. Latella, C. J. Barbé, and M. V. Swain, "Mechanical properties and adhesion characteristics of hybrid sol-gel thin films," *Surf. Coatings Technol.*, vol. 192, no. 2–3, pp. 354–364, 2005, doi: 10.1016/j.surfcoat.2004.06.004.

[67] P-J Millet and A. Iost, "Méthodologie de caractérisation des propriétés mécaniques de revêtements sol-gel hybrides," 2014.

[68] Y. Leterrier, "Durability of nanosized oxygen-barrier coatings on polymers," *Prog. Mater. Sci.*, vol. 48, no. 1, pp. 1–55, 2003, doi: 10.1016/S0079-6425(02)00002-6.

[69] J. Valli, "A review of adhesion test methods for thin hard coatings," *J. Vac. Sci. Technol. A Vacuum, Surfaces, Film.*, vol. 4, no. 6, pp. 3007–3014, 1986, doi: 10.1116/1.573616.

[70] A. J. Perry, "The adhesion of chemically vapour-deposited hard coatings to steel-the scratch test," *Thin Solid Films*, vol. 78, no. 1, pp. 77–94, 1981, doi: 10.1016/0040-6090(81)90419-3.

[71] S. J. Bull and E. G. Berasetegui, “An overview of the potential of quantitative coating adhesion measurement by scratch testing,” *Tribol. Int.*, vol. 39, no. 2, pp. 99–114, 2006, doi: 10.1016/j.triboint.2005.04.013.

[72] P. A. Steinmann, Y. Tardy, and H. E. Hintermann, “Adhesion testing by the scratch test method: The influence of intrinsic and extrinsic parameters on the critical load,” *Thin Solid Films*, vol. 154, no. 1–2, pp. 333–349, 1987, doi: 10.1016/0040-6090(87)90377-4.

[73] M. D. Thouless, “An analysis of spalling in the microscratch test,” *Eng. Fract. Mech.*, vol. 61, no. 1, pp. 75–81, 1998, doi: 10.1016/S0013-7944(98)00049-6.

[74] R. Moharrami and M. Sanayei, “Developing a method in measuring residual stress on steel alloys by instrumented indentation technique,” *Meas. J. Int. Meas. Confed.*, vol. 158, p. 107718, 2020, doi: 10.1016/j.measurement.2020.107718.

[75] H. Liu and D. shu Qian, “Evaluation of residual stress and corrosion behaviour of electroless plated Ni−P/Ni−Mo−P coatings,” *Transactions of Nonferrous Metals Society of China (English Edition)*, vol. 28, no. 12. pp. 2499–2510, 2018, doi: 10.1016/S1003-6326(18)64896-4.

[76] S. Suresh and A. E. Giannakopoulos, “A new method for estimating residual stresses by instrumented sharp indentation,” *Acta Mater.*, vol. 46, no. 16, pp. 5755–5767, 1998, doi: 10.1016/S1359-6454(98)00226-2.

[77] Z. Qu, K. Wei, Q. He, R. He, Y. Pei, S. Wang and D. Fang, “High temperature fracture toughness and residual stress in thermal barrier coatings evaluated by an in-situ indentation method,” *Ceram. Int.*, vol. 44, no. 7, pp. 7926–7929, 2018, doi: 10.1016/j.ceramint.2018.01.230.

[78] W. G. Mao, J. Wan, C.Y. Dai, J. Ding, Y. Zhang, Y.C. Zhou and C. Lu, “Evaluation of microhardness, fracture toughness and residual stress in a thermal barrier coating system: A modified Vickers indentation technique,” *Surf. Coatings Technol.*, vol. 206, no. 21, pp. 4455–4461, 2012, doi: 10.1016/j.surfcoat.2012.02.060.

[79] B. R. Lawn and E. R. Fuller, “Measurement of thin-layer surface stresses by indentation fracture,” *J. Mater. Sci.*, vol. 19, no. 12, pp. 4061–4067, 1984, doi: 10.1007/BF00980772.

[80] N. Vidakis, A. Antoniadis, and N. Bilalis, “The VDI 3198 indentation test evaluation of a reliable qualitative control for layered compounds,” *J. Mater. Process. Technol.*, vol. 143–144, no. 1, pp. 481–485, 2003, doi: 10.1016/S0924-0136(03)00300-5.

[81] M. Jafarzadegan, A. Abdollah-zadeh, A. H. Feng, T. Saeid, J. Shen, and H. Assadi, “Microstructure and Mechanical Properties of a Dissimilar Friction Stir Weld between Austenitic Stainless Steel and Low Carbon Steel,” *J. Mater. Sci. Technol.*, vol. 29, no. 4, pp. 367–372, 2013, doi: 10.1016/j.jmst.2013.02.008.

[82] Agilent Technologies, “Indentation Rules of Thumb - Applications and Limits,” pp. 1–8, 2010, [Online]. Available: https://www.semanticscholar.org/paper/Indentation-Rules-of-Thumb-—-Applications-and-Note/1f89c80f83b9cbac10fd8715ac381824abafd467.

[83] D. Chicot, “Hardness length-scale factor to model nano- and micro-indentation size effects,” *Mater. Sci. Eng. A*, vol. 499, no. 1–2, pp. 454–461, 2009, doi: 10.1016/j.msea.2008.09.040.

[84] T. Sawa and K. Tanaka, “Simplified method for analyzing nanoindentation data and evaluating performance of nanoindentation instruments,” *J. Mater. Res.*, vol. 16, no. 11, pp. 3084–3096, 2001.

[85] A. Iost, G. Guillemot, Y. Rudermann, and M. Bigerelle, “A comparison of models for predicting the true hardness of thin films,” *Thin Solid Films*, vol. 524, pp. 229–237, 2012, doi: 10.1016/j.tsf.2012.10.017.

[86] D. Chicot, M. Yetna N'Jock, E.S. Puchi-Cabrera, A. Iost, M. H. Staia, G. Louis, G. Bouscarrat and R. Aumaitre, “A contact area function for Berkovich nanoindentation: Application to hardness determination of a TiHfCN thin film,” *Thin Solid Films*, vol. 558, pp. 259–266, 2014, doi: 10.1016/j.tsf.2014.02.044.

[87] D. Chicot, P. de Baets, M.H. Staia, E.S. Puchi-cabrera, G. Louis, Y. Perez Delgado and J. Vleugels, "Influence of tip defect and indenter shape on the mechanical properties determination by indentation of a TiB2-60%B4C ceramic composite," *Int. J. Refract. Met. Hard Mater.*, vol. 38, pp. 102–110, 2013, doi: 10.1016/j.ijrmhm.2013.01.006.

[88] A. L. M. Costa, D. J. Shuman, R. R. Machado, and M. S. Andrade, "Determination of the compliance of an instrumented indentation testing machine," *IMEKO TC5 Conf. Hardness Meas. Theory Appl. Lab. Ind. HARDMEKO 2004*, no. January, pp. 30–35, 2004.

[89] C. Ullner, E. Reimann, H. Kohlhoff, and A. Subaric-Leitis, "Effect and measurement of the machine compliance in the macro range of instrumented indentation test," *Meas. J. Int. Meas. Confed.*, vol. 43, no. 2, pp. 216–222, 2010, doi: 10.1016/j.measurement.2009.09.009.

[90] Wiki, "Chromium." https://en.wikipedia.org/wiki/Chromium (accessed Oct. 10, 2021).

[91] The material project, "Materials Explorer:Cr." https://materialsproject.org/materials/mp-90?chemsys=Cr (accessed Aug. 28, 2022).

[92] FactSage, "Collection of Phase Diagrams: Ni-W." https://www.crct.polymtl.ca/fact/phase_diagram.php?file=Ni-W.jpg&dir=SGTE2014 (accessed May 11, 2020).

[93] R. Cury, J. M. Joubert, S. Tusseau-Nenez, E. Leroy, and A. Allavena-Valette, "On the existence and the crystal structure of Ni4W, NiW and NiW2 compounds," *Intermetallics*, vol. 17, no. 3, pp. 174–178, 2009, doi: 10.1016/j.intermet.2008.11.001.

[94] The material project, "Materials Explorer: Ni-W." https://materialsproject.org/materials?chemsys=Ni-W (accessed Aug. 28, 2022).

[95] Y. Leterrier, "Fragmentation Test Method for Adhesion Analysis of Coatings," 2009.

[96] Wiki, "Nickel." https://en.wikipedia.org/wiki/Nickel (accessed Mar. 01, 2021).

[97] M. H. Allahyarzadeh, M. Aliofkhazraei, A. R. Rezvanian, V. Torabinejad, and A. R.

Sabour Rouhaghdam, “Ni-W electrodeposited coatings: Characterization, properties and applications,” *Surf. Coatings Technol.*, vol. 307, pp. 978–1010, 2016, doi: 10.1016/j.surfcoat.2016.09.052.

Abstract

Hard chrome coatings (Cr-VI) are obtained from Cr^{6+} solutions that are CMR (Carcinogenic, Mutagenic and Reprotoxic). Their use is strongly limited by UE regulations and will be completely forbidden in the next coming years. Current alternatives do not have such high versatility as hard chrome coatings. This study aims to compare some alternatives based on electroplated NiW (nickel tungsten) coating, regarding their mechanical properties. Firstly, coatings are investigated by means of indentation at a microscale, including classical and instrumented tests, performed on top surface and cross-section. A full processing protocol is proposed to take into account tip defect, indentation size effect and contribution of the substrate. The hardness of Cr-VI is found to be 8.0 and 8.5 GPa on top surface and cross-section respectively. It is almost two times higher than these of NiW coatings obtained with two different current density, namely 4.4 and 5.0 GPa. Microstructure of both Cr-VI and NiW coatings are explored by *ex-situ* and *in-situ* under temperature X-ray diffraction tests. In addition to the growth of crystallites with temperature, XRD reveals a decrease of the residual stress inside the coatings. Adhesion and toughness of coatings are investigated by several experimental approaches (indentation, tensile test, scratch test). NiW coatings electroplated with the highest current density have a better adhesion and toughness behaviors than NiW with lower current density and Cr-VI.

Key words: thin film, Indentation, X-ray diffraction, cracks analysis

Résumé

Les revêtements de chrome dur (Cr-VI) sont obtenus à partir de solutions contenant du Cr^{6+}, elles sont CMR (Cancérogène, Mutagène et Reprotoxique). Leur utilisation est fortement limitée par la réglementation européenne et sera totalement interdite dans les années à venir. Les alternatives actuelles ne sont pas aussi polyvalentes que les revêtements en chrome dur. Cette étude compare, du point de vue de leurs propriétés mécaniques, certaines alternatives basées sur des revêtements NiW (au nickel-tungstène) obtenus par voie électrolytique. Tout d'abord, les revêtements sont étudiés par indentation à échelle microscopique, incluant des tests classiques et instrumentés, effectués sur la surface originelle et la section transversale. Un protocole d'analyse est proposé pour prendre en compte le défaut de pointe, l'effet de taille en indentation et la contribution du substrat. La dureté du Cr-VI est respectivement de 8,0 et 8,5 GPa sur la surface originelle et la section transversale. Elle est presque deux fois supérieure à celles des revêtements NiW obtenus avec deux densités de courant différentes, à savoir 4,4 et 5,0 GPa. La microstructure des revêtements Cr-VI et NiW est explorée par des tests de DRX (diffraction de rayons X) *ex-situ* puis *in-situ* sous température. En plus de la croissance des taille de grains avec la température, la DRX révèle une réduction des contraintes résiduelles dans les revêtements. L'adhérence et la ténacité des revêtements sont étudiées par plusieurs approches expérimentales (indentation, essai de traction, rayure). Les revêtements NiW électrodéposés avec la densité de courant la plus élevée ont de meilleurs comportements d'adhérence et de ténacité que les NiW avec une densité de courant plus faible et que le Cr-VI.

Mots clés: Film mince, Indentation, Diffraction des rayons X, Analyse des fissures